

POLITECNICO DI TORINO

Department of Engineering

Master Degree in Mechanical Engineering

Master Degree Thesis

Effect of microinclusions on the fatigue life of rolling bodies



Tutor:
Ing. Raffaella Sesana
Prof. Eugenio Brusa

Candidate:
Francesco Morosi

Academic Year 2017/2018

Abstract

The goal of this study is to understand how the microinclusions affect the fatigue life of rolling bodies. In order to do this, a numerical method was considered, and its results were correlated with experimental ones, investigating whether a microinclusion threshold parameter could be defined, to be related to the life bearing requirements.

Many phenomena are involved in damage of rolling elements of bearings. Rolling contact fatigue is the main cause of failure, along with contact pressure related fatigue and dimensional instabilities effect. Most of those are well known, and are described by wide experimental, analytical and numerical literature. Damage phenomena are related to material properties and manufacturing processes.

Nowadays, steels are well-suited in bearings manufacturing, and they represent the most established materials for these applications. Each of these is not free of non metallic inclusions because of the manufacturing process. These inhomogeneities have an important role on the fatigue performances, since the damage evolution of the rolling elements of bearings is affected by the microinclusions present in the material. This study is focused on the AISI 52100 (100Cr6), that is the main steel in bearings production.

Non metallic inclusions like sulfides, carbides and oxides act like stress concentrators, and this can originate cracks which lead to failure. Inclusions have different composition, dimension, configuration and distribution so their effect on the fatigue life changes depending on these parameters. For this reasons, different types of non metallic inclusions were analyzed, in order to have an overview of the phenomena.

The stresses around the non metallic inclusions are evaluated thanks to a MATLAB code [16] based on the Eshelby solution for this type of problem [4]. Then, this stresses are counted in order to evaluate a microinclusion threshold parameter. A correlation between stress computed by the model and experimental failures (performed thanks to fatigue test rigs and a rotating bending machine) has been shown, with a good matching of the data.

Contents

1	Introduction	5
2	Rolling Contact Fatigue	9
2.1	Factors that influence RCF Life	10
2.2	Cleanliness	11
2.2.1	Dimension	12
2.2.2	Shape	12
2.2.3	Depth	12
2.2.4	Chemical composition	12
2.2.5	Configuration	12
2.3	Hertz Theory	14
2.3.1	Local geometry	14
2.3.2	Stress	18
3	Balls manufacturing process	21
4	Materials and Methods	23
4.1	Experimental set up	24
4.1.1	Rotating bending fatigue tests	24
4.1.2	Test Rigs for bearing balls	27
4.1.3	After failure analyses - Spheres	31
4.1.4	After failure analyses - Specimens	32
4.2	Stresses calculation	33
4.2.1	Hertzian stress - Spheres	33
4.2.2	Stress - Specimens	36
4.2.3	Stress variation	38
5	Model	39
5.1	Eshelby model	39
5.1.1	Equivalent inclusion method	40

5.2	Numerical solver	42
6	Numerical Simulations	44
6.1	Dimension	45
6.2	Shape	47
6.3	Depth	49
6.4	Chemical composition	50
6.4.1	Inclusion Composition	50
6.4.2	Matrix composition	51
6.5	Configuration	51
6.6	Conclusions	52
7	Failures on balls	53
7.1	Case 1	54
7.2	Case 2	57
7.3	Case 3	60
7.4	Case 4	63
7.5	Case 5	66
7.6	Case 6	69
7.7	Case 7	72
8	Failures on specimens	75
8.1	Case 1	76
8.2	Case 2	79
8.3	Case 3	81
8.4	Case 4	83
8.5	Case 5	86
8.6	Case 6	88
8.7	Case 7	90
9	Life - Stress Relation	92
9.1	Stress threshold	94
9.1.1	Spheres	94
10	Conclusions	95
11	Future works	96

A	Balls - others inclusions	103
A.1	Case 1	103
	A.1.1 Second inclusion	103
	A.1.2 Third inclusion	104
A.2	Case 2	105
	A.2.1 Second inclusion	105
	A.2.2 Third inclusion	106
A.3	Case 5	107
	A.3.1 Second inclusion	107
A.4	Case 6	108
	A.4.1 Second inclusion	108
	A.4.2 Third inclusion	108
A.5	Case 7	109
	A.5.1 Second inclusion	109
	A.5.2 Third inclusion	110

Chapter 1

Introduction

Tsubaki Nakashima Co., Ltd. manufactures and sells steel balls and precision products worldwide. In particular, the group is a global leader of rolling contact elements as premium quality precision balls, rollers, cages, and sheet metal parts.

Pinerolo plant, where this study was carried out, is specialized in ball manufacturing for bearings production.

The bearing is a part of the machine that allows one part to rotate or move in contact with another part with as little friction as possible. Additional functions include the transmission of loads and enabling the accurate location of components. A bearing may have to sustain severe static as well as cyclic loads while serving reliably in difficult environments [2].

A wide variety of bearing designs exists to allow the demands of the application to be correctly met for maximum efficiency, reliability, durability and performance.

Bearings are composed of different elements: cylinders or balls as rolling elements and external and internal rings, which form the raceways. Also the lubrication between the parts is very important.

Fatigue life performances of the rolling elements have a key role to prevent premature failures of the bearings during working operations. For this reason, it is important to understand how the microinclusions affect the life of the balls and consequently of the bearing.

It is now been clearly established that fatigue resistance correlates strongly with steel cleanliness. Non metallic inclusions play an essential role in the length of the rolling contact fatigue (RCF) life. However, inclusions are inevitably present in steels, they cannot be eliminated in the steelmaking process [11]. On the other hand, the improvement of the technologies allows to reduce

the total quantity of these non metallic inclusions, improving the fatigue life.

In general, rolling contact fatigue is driven by two phenomena: surface originated pitting and subsurface originated spalling. These two are different, at the point that they can be considered separately. The first one can be prevented with better lubricants or a better surface finish [12], while there are not many ways to stop subsurface originated fatigue. Subsurface cracks mostly occur at stress concentration sites such as material defects, voids and non-metallic inclusions. Such inclusions act like stress risers, leading to cracks and final failure [14]. The inclusions are very critical since they are in a position where the shear stress due to the Hertzian contact is maximum.

Many studies, both experimental and numerical ones, have been carried out to understand the most important factors that affect RCF life. Nowadays it is known that they are: inclusion composition, size, shape and location [11].

The relationship between the RCF life and the maximum inclusion size has been studied by Nagao et al.[15] and Seki [18], but the results are different of one order of magnitude even if the size of the inclusion is the same. For this reason, Hasmimoto et al. [11] made experimental tests to analyze the role of the composition using different deoxidation post-processes. The size and composition are evaluated thanks to an optical microscopy and an X-ray energy dispersive spectroscopy (XREDS). The tests showed that the RCF life in case of similar sized inclusions, is affected primarily by the chemical composition. In particular, they showed that RCF life is improved reducing the oxygen content as the size of the oxides. Moreover, they examined the length of the crack around the inclusions throughout the test, finding out that the crack length controlling RCF life is influenced by the interface condition between the inclusion and the matrix. Since matrix-MnS and matrix-TiN interfaces showed no cavities, they suggested that the oxide inclusions play the most detrimental role in the material's RCF. Also S. M. Moghaddam et al.[14] and J. Guan et al.[9] studied the effect of the inclusion composition, considering the inclusion elastic modulus. The maximum von Mises stress increases with the increase of the elastic modulus of the inclusion and it appears at the interface between inclusion and surrounding material.

The effect of size, stiffness and depth has been shown in [14] and in [9]. The authors of [14] and [9] developed a model that takes advantage of the Voronoi tessellation to construct the FEM domain. In this way, the model is able to capture the butterfly wing formation, crack initiation and crack propagation. Moreover, the model was used to study the different RCF life varying size,

stiffness and depth.

Regarding the size, a comparison between a 16 μm and a 8 μm inclusions with the same stiffness value and depth, has been made [14]. Similar test were performed in [9], with a set of inclusions which is set to vary from 5 μm to 20 μm . No strong influence on stress concentration was found, but it is known that larger inclusions subject larger volumes of the material to stress concentration. Furthermore, larger inclusions have a higher chance of being located at the critical depth.

For what concerns the inclusion location, the stress profile changes at the inclusion depth, while the rest of the profile remains pristine. Inclusions located at 0.5 times the contact half width (b) are critical [14], since there is the maximum von Mises stress calculated from the Hertz theory. For a certain value of depth, the stress rise remains below the original stress at $0.5b$, so the inclusion will not be the controlling phenomenon of the RCF life. J.Guan et al. [9] showed that the highest stress concentration is located at about $0.75b$ but both [14] and [9] lead to the same conclusion.

Taking into account the shape of the inclusion, Stienon et al.[1] showed that stress fields obtained with simplified shape are in good agreement with those obtained with real shape, therefore is reasonable to use simplified shapes to simulate the stress concentration around the inclusion.

J. Courbon et al.[8] examined the interaction between multiple inclusions (pairs, clusters and stringers) using the Moschovidis and Mura extension [17, 21] of the Eshelby method [4]. They found out that the orientation of the axes according to which the inclusions are arranged, plays a fundamental role on the stress field.

Once that the effect of microinclusions on the material matrix is clarified, it would be very useful to have a model that is capable to predict the bearing fatigue life considering the steel cleanliness. Lamagnere et al. [12] presented a model that calculates the fatigue limit H_1 of the bearing steel, it is the maximum Hertzian pressure that would not introduce any plastic deformation. This threshold is derived from the comparison between the local shear stress around the inclusion and the microyield stress of the matrix.

The idea of a stress threshold below which a material would not be damaged was first introduced by Weibull [20], and then developed in bearing fatigue life models by several authors [6, 7], but without considering the steel cleanliness. The local shear stress around the inclusion is calculated with the Eshelby method [4], while the microyield stress of the matrix is evaluated by means of

experimental compression tests.

The current work investigates the effect of microinclusions on fatigue life of a steel alloy (100Cr6) for bearing rolling elements. Fatigue damage and failure mechanisms are studied by experimental testing on test bench and analytical models are considered, to relate life of rolling elements to the microinclusion parameters. A dedicated 3D solver implementing Eshelby model [4] was developed to estimate the stress distribution surrounding the microinclusion. The simulated load corresponds to experimental load applied to a set of ball bearing undergoing fatigue testing. The calculated stresses will be used as input for a microinclusion threshold estimation model to estimate the life of the ball bearing. It has to be observed that microinclusion chemical composition, shape, dimension, depth and configuration are introduced in the numerical model after experimental failure observation. This procedure aims at validating numerical model and life estimation model on bearing balls.

Chapter 2

Rolling Contact Fatigue

The fatigue life of bearings is determined primarily by two factors: the detachment of material (spalling) following the initiation of cracks below the contact surface and spalling due to surface irregularities and due to distress caused by surface roughness [2]. In this study the focus is on the first of these failure mechanism, since inclusions are located at a certain depth respect to the surface and the crack starts from the inclusion itself. Nowadays, the bearing steels are clean, in the sense that the number of inclusion is not as big as was in the past, but inclusions persist.

In this project, the analyses on microinclusions were made on failed balls coming from Test Rigs. A ball is considered failed when is no longer capable to perform rotations or excessive vibrations and noise occur. The spalling phenomenon is the cause of failure of the balls with inclusions, in concomitance with overload but it can happen also without a particular inclusion, so due to pure overload. Spalling begins with microcracks initiating on the subsurface of the rolling body, followed by coalescence of multiple microcracks which then reach the surface.

Failure can also occur in a more dramatic way by crack formation along the entire section of a bearing rolling element, but this can be prevented by stopping the test benches when vibrations exceed the limits. Typically, when the vibrations evaluated by the test rig start to increase, the formation of spalls and pits among the balls and the raceways is begun.

2.1 Factors that influence RCF Life

There are many factors that can affect the RCF life of a component, like:

- contact pressure
- material properties
- lubricant properties
- surface roughness
- relative slip during the rotation between the elements
- microstructure
- cleanliness condition

Since the aim of the study is to analyze the effect of microinclusions on the bearing life, the focus is on the cleanliness condition.

2.2 Cleanliness

Non-metallic inclusions affect negatively the fatigue life of a rolling body, like a ball in a bearing. They are detrimental also in case of components that are stressed with alternating stresses in general, so subjected to fatigue, like the specimens used in the rotating bending machine analyzed in this study. Inclusions are inevitably present in steels, because they cannot be eliminated in the steelmaking process. When using modern steelmaking processes to decrease the amount of oxide inclusions, the other impurities such as sulfides or nitrides may grow larger [11].

The inclusions may also be brittle, and the resulting cracks concentrate stress and then may nucleate from these discontinuities into the subsurface of the rolling element. A non-metallic inclusion, even if it is uncracked, produces a mechanical heterogeneity which locally changes the stress distribution. In such circumstances, the depth in which the maximum shear stress and then the maximum damage is expected could not coincide with that calculated from the Hertzian theory of normal contact of homogeneous steel [2]. Further clarifications on the severity of different types of inclusions will be showed in the next chapters.

There are several parameters that are useful to characterize the inclusions:

- Dimension
- Shape
- Depth
- Chemical composition
 - Oxides
 - Nitrides
 - Carbides
 - Silicates
 - others
- Configuration

2.2.1 Dimension

Considering several cases of microinclusions, the size of them can change significantly depending on the inclusion type. Inclusion size affects the stress distribution around the inhomogeneity; in particular the stressed volume increases with the increase of the inclusion size. The maximum value of the stress (like the maximum von Mises stress) due to the presence of the inclusion, does not depend strongly on the inclusion size [9], as the Eshelby numerical model will confirm.

2.2.2 Shape

Inclusions can have different shape depending on their chemical composition. Typically Al_2O_3 inclusions have a spheroidal or ellipsoidal shape, while for example Nitrides and Carbides are sharper. The effect of the shape of an ellipsoidal inclusion will be seen in the next chapters.

2.2.3 Depth

Inclusions can appear at a random depth in the component volume. Due to the stress distribution under the surface of the object, it is possible to say that if the defect is positioned too far from the surface, the stress concentration effect can be neglected. On the other hand, if the inclusion is located at a critical depth (that depends on geometrical parameters of the contact), it is detrimental for the fatigue life [9].

2.2.4 Chemical composition

The chemical composition is an important factor, because it is related with the Young modulus. Most of non-metallic inclusions have an elastic modulus higher than the matrix one. Increasing the difference between the two moduli, the maximum von Mises stress or Tresca stress will increase [9].

Another parameter that is influenced by the chemical composition is the Poisson ratio. As seen for the Young modulus, if the difference between the two Poisson ratios increases, the stress will have a major increase.

2.2.5 Configuration

The configurations in which the inclusions are present affect the endurance limit of the bearing steel. Examples of these configurations are pairs, clusters

and stringers.

When two or more inclusions are next to each other, with a distance that is under a certain limit, the approximation of an uniform applied strain field in the inclusion area is no longer valid [8], so the Eshelby model should be revised. Further clarifications on this aspect will be seen in the next chapters.

2.3 Hertz Theory

The problem of elastic contact between two elastic bodies was first solved by Heinrich Rudolf Hertz. His purpose was to determine mathematically how bodies in 'point contact' when undeformed will behave when loaded one against the other. He obtained his results within the classical theory of elasticity.

Contact conditions:

1. Geometry:

- two bodies in contact
- in a non-singular point of their surfaces (regular at least to the second derivative); then (first derivatives) the common tangent plane exist

2. Material:

- elastic, isotropic
- no friction

3. Hypothesis:

- small contact surface (length and width small compared to curvature radii of bodies in contact)

2.3.1 Local geometry

The properties of body 1 are, developed up to the 2^{nd} order derivative at point $(0,0)$:

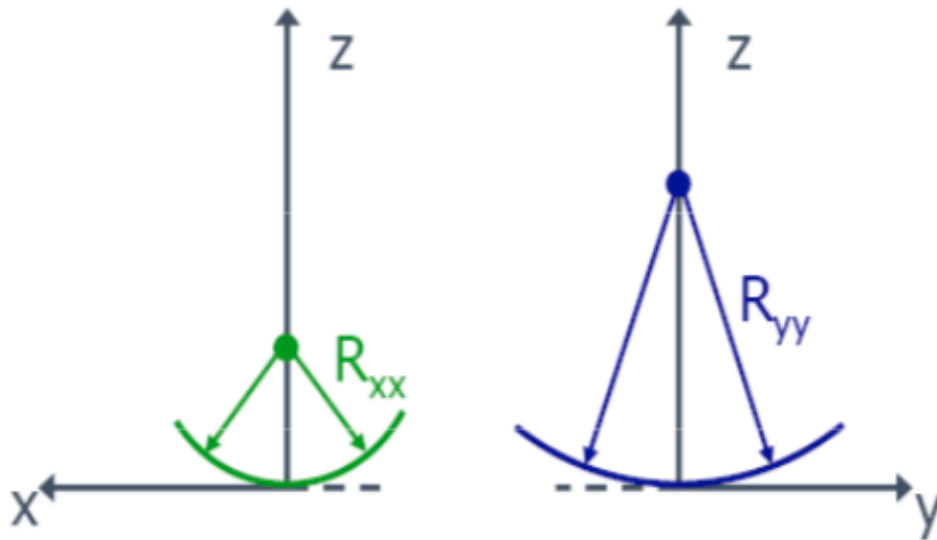
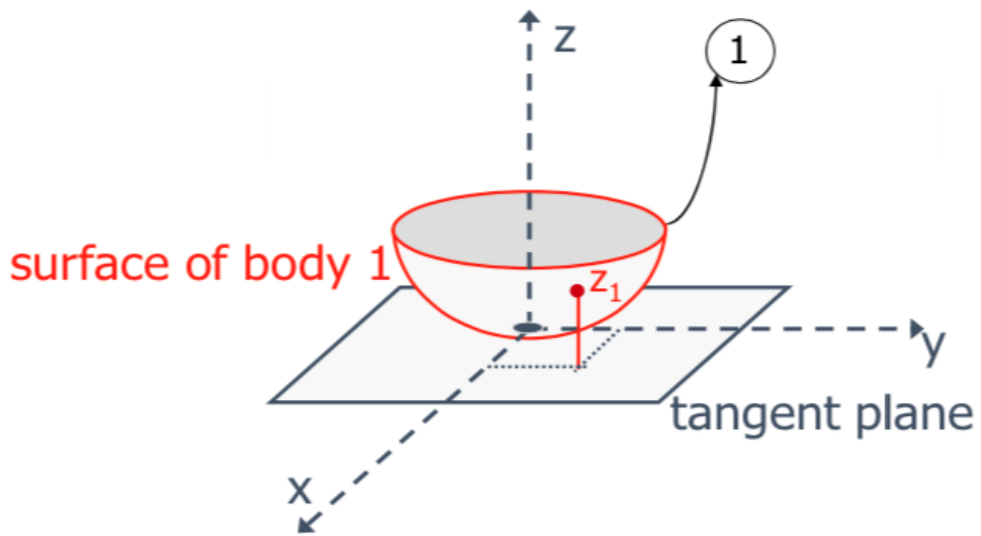
$$z_1 \simeq 0 + 0 \cdot x + 0 \cdot y + \frac{1}{2} \left[\frac{\partial^2 z_1}{\partial x^2} x^2 + 2 \frac{\partial^2 z_1}{\partial x \partial y} xy + \frac{\partial^2 z_1}{\partial y^2} y^2 \right] + \dots \quad (2.1)$$

Where:

- $z_1 = z_1(x, y)$
- $z_1(0, 0) = 0$
- $\frac{\partial z_1}{\partial x}(0, 0) = 0$

- $\frac{\partial z_1}{\partial y}(0,0) = 0$
- $\alpha_{xx} = \frac{1}{2} \cdot \frac{\partial^2 z_1}{\partial x^2} = \frac{1}{2} \cdot \frac{1}{R_{xx,1}}$
- $\alpha_{yy} = \frac{1}{2} \cdot \frac{\partial^2 z_1}{\partial y^2} = \frac{1}{2} \cdot \frac{1}{R_{yy,1}}$

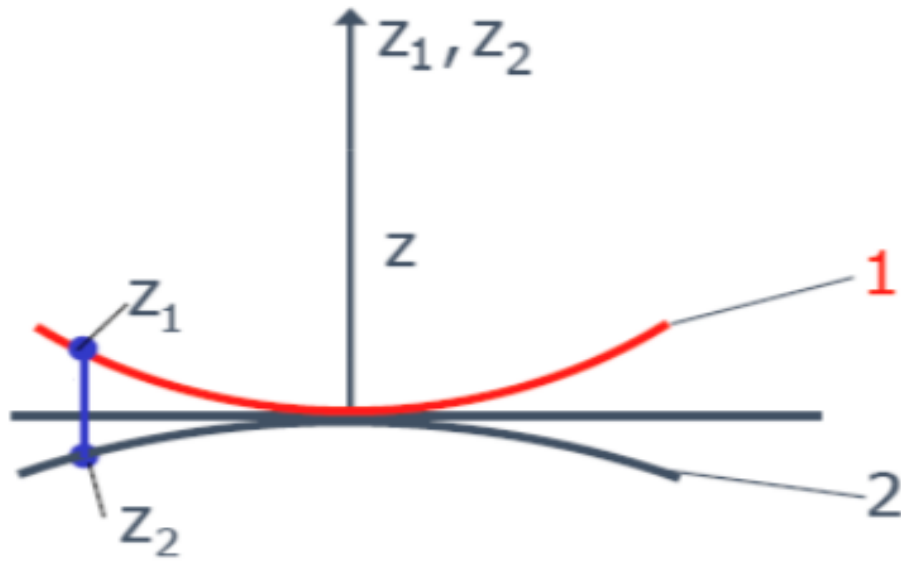
R_{xx} and R_{yy} are the curvature radii of the section with plane xz and of the section with plane yz , respectively.



For body 2, the properties can be defined similarly, and the curvature radii are:

- $\beta_{xx} = \frac{1}{2} \cdot \frac{\partial^2 z_2}{\partial x^2} = \frac{1}{2} \cdot \frac{1}{R_{xx,2}}$
- $\beta_{yy} = \frac{1}{2} \cdot \frac{\partial^2 z_2}{\partial y^2} = \frac{1}{2} \cdot \frac{1}{R_{yy,2}}$

If body 2 is concave, the coefficients β would be negative.



At all points (x, y) $z_1 - z_2 \geq 0$ since interpenetration does not occur. Moreover, experimental observations suggest that when two bodies are pressed one against to each other they will touch over a surface having an elliptical contour (Fig. 2.1).

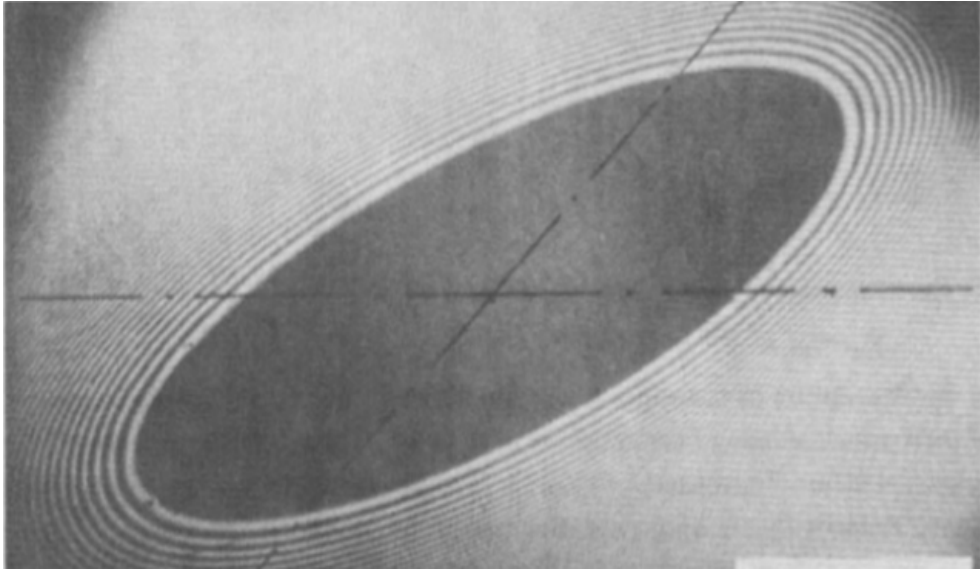


Figure 2.1: Interference fringes of two transparent bodies in contact, loaded

Moreover, rigid body motion combines with elastic deformation when the two bodies are approaching, so that the deformed shape of the bodies are related to the elastic properties of the material (Eq. 2.2). On each area element:

$$dA = dx' dy'$$

inside the contact surface at a point (x', y') , an infinitesimal force dF is applied:

$$dF = p(x', y') dx' dy'$$

which produces at any other point of coordinates (x, y) a contribution to displacements:

$$du = \frac{1-\nu^2}{\pi E} \frac{1}{r_b} \cdot p(x', y') dx' dy'$$

$$u(x, y) = \frac{1-\nu^2}{\pi E} \int \int \frac{p(x', y')}{r'} dx' dy'$$

$$\text{where: } r_b = \sqrt{(x - x')^2 + (y - y')^2}$$

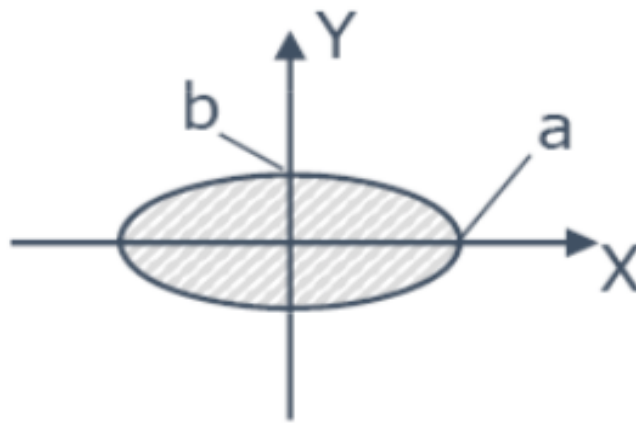
$$\frac{u_1(x, y)}{u_2(x, y)} = \frac{\frac{1-\nu_1^2}{E_1}}{\frac{1-\nu_2^2}{E_2}} \quad (2.2)$$

Hertz found that, with a contact force F :

$$F = \int \int p(x, y) \cdot dx \cdot dy$$

$$p = \frac{3}{2} \frac{F}{\pi ab} \cdot \sqrt{1 - \frac{x^2}{a^2} - \frac{y^2}{b^2}}$$

with: a, b semi axes of the elliptic contact surface. The values of the semi axes depend on the solution of an integral equation, which is normally given in numerical form.



2.3.2 Stress

Experimental evidence shows that failure starts at points below the surface. For this reason, it is interesting to know the 3D stress status along the z -axis, which is the one that is parallel to the applied force. In this way, it is possible to calculate the principal stresses and then the maximum tangential stress, the von Mises stress and so on.

The stresses below the surface, for the sphere-sphere contact and for the cylinder-cylinder contact, are represented below (Fig. 2.2, Fig. 2.3) and that is similar to what happens in the sphere-ring contact inside a bearing.

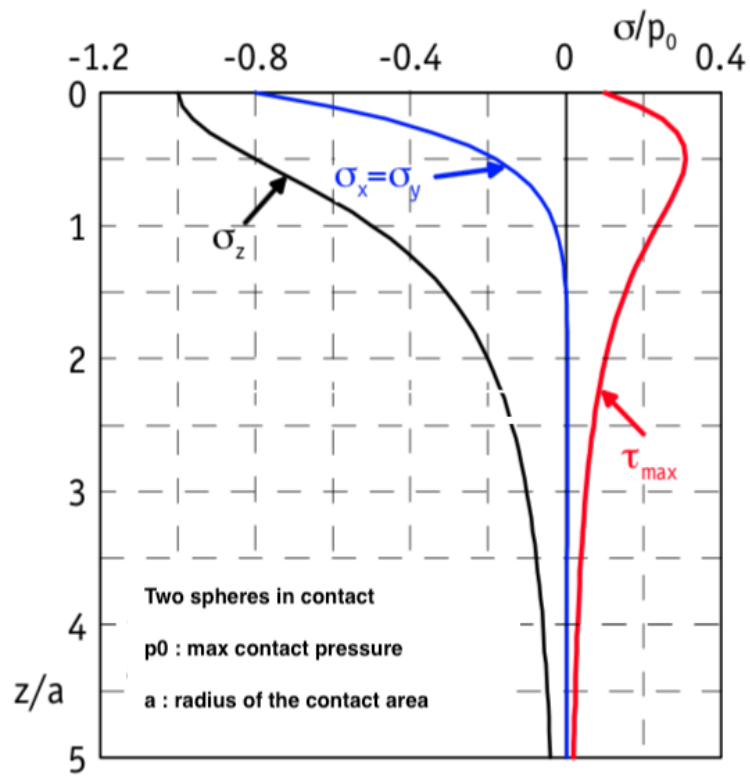


Figure 2.2: Subsurface stresses: sphere-sphere contact

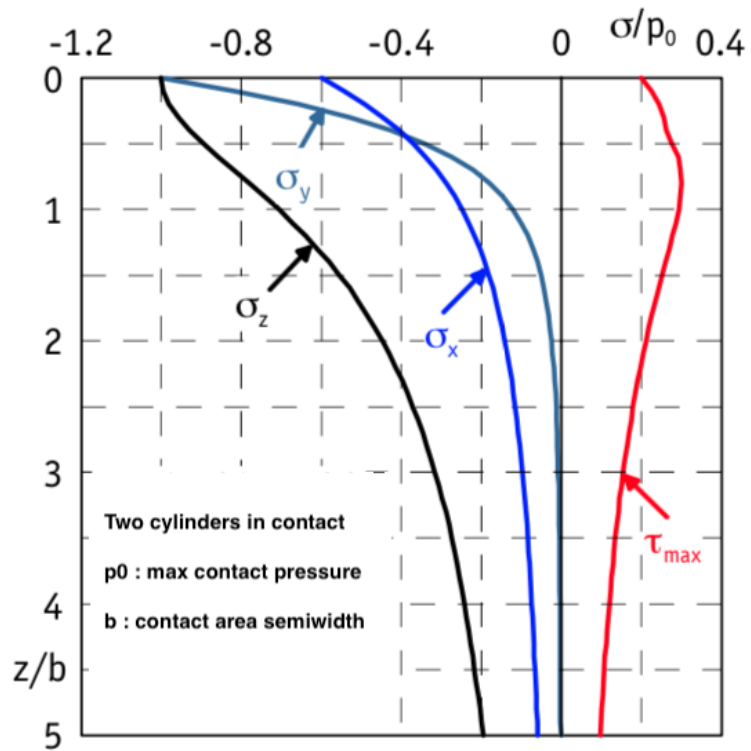


Figure 2.3: Subsurface stresses: cylinder-cylinder contact

Many researches have been conducted to study which shear stress (maximum tangential stress, von Mises stress, Tresca stress) is the one that has to be considered in the context of fatigue of contacting bodies [10, 19]. Their roles can in principle be determined by comparing the respective stress distributions against the location of maximum damage in experiments. However, whichever shear stress is considered, the maximum occurs below the contact surface and this has significant consequences to the development of damage. Notice that the shear stress is proportional to the contact pressure p_0 but the proportionality constant will depend on the geometry of the contact [2].

Chapter 3

Balls manufacturing process

Heading

The balls production starts from a wire which is fed from a coil into a machine that cuts it in short pieces. After that, the pieces are formed into a rough sphere by pressing in a hemispherical matrix. In this process, the wire is not heated before being headed. For this reason, the process is called cold heading.

Soft grinding

After heading, the balls show a ring around the middle due to the moulding, the soft grinding phase allows to remove this exceeding material. The ball bearings pass through two cast iron disks that presents rough grooves in which the ball was filed. The balls are left oversized because of the following process of surface finishing which brings the balls to their finished size.

Heat Treatment

Normally, the Heat Treatment phase consists in Quenching followed from Tempering. The balls pass through a heat-treating furnace at about 840 degrees Celsius (Austenitization temperature) and then they are dropped into an oil or water bath to cool them almost instantly. This process makes the balls harder than before the treatment, but also give a brittle steel, whereby the balls are also tempered.

Peening

After heat treatment, the balls are subjected to peening, which is a cold working process used to produce a subsurface residual stress that can be beneficial if it is compressive and localized immediately below the surface [2].

Surface Finish

Right after peening, the balls, which are oversized, begin the last process; the balls pass into grinding wheels that grind the balls down so that they are round within cents of micron. After this, the balls are lapped to their final surface finish.

Chapter 4

Materials and Methods

The project presented here is composed by an analytical part, supported by a numerical code, and an experimental part, that includes rotating bending fatigue tests performed on specimens and ball bearings tests executed on RCF benches.

Starting from the cases analyzed experimentally, some parameters have been changed in the numerical model, in order to understand the effect of the various parameters.

The RCF benches are useful to study the failures due to microinclusions of the spheres, that are mounted inside the bearing. Nevertheless inclusions are already present in the steel, from the steel making process; for this reason also rotating bending fatigue tests on steel samples were performed. In these type of tests, the goal is to analyze the fatigue behavior of the pure steel, thanks to standard specimens.

When the specimen or a ball fails, an analysis of the fracture was made, evaluating the inclusion presence and characterization.

The last aim of this project was to define a threshold parameter to estimate the fatigue life of the balls that accounts the inclusion presence.

4.1 Experimental set up

The experimental tests provided real data about the inclusions; thanks to this data the stress distribution around the inclusion was calculated. Moreover, these informations were helpful to have a general knowledge of the real properties of the inclusions present in the steel, and so to have a solid database for the numerical simulations.

4.1.1 Rotating bending fatigue tests

The rotating bending fatigue test has the objective to test the raw material (Fig. 4.3). The steel wire was cut in 150 *mm* samples and then straightened to nullify the curvature of the coil (Fig. 4.1) . Then, the sample was quenched (for 12 minutes at 850°C) in salt water or oil to obtain the same properties of the steel balls.



Figure 4.1: Raw steel coil cut and final specimen

From the sample, the standard specimens were obtained, following the drawing below (Fig. 4.2), as requested by the ISO 1143 specification.

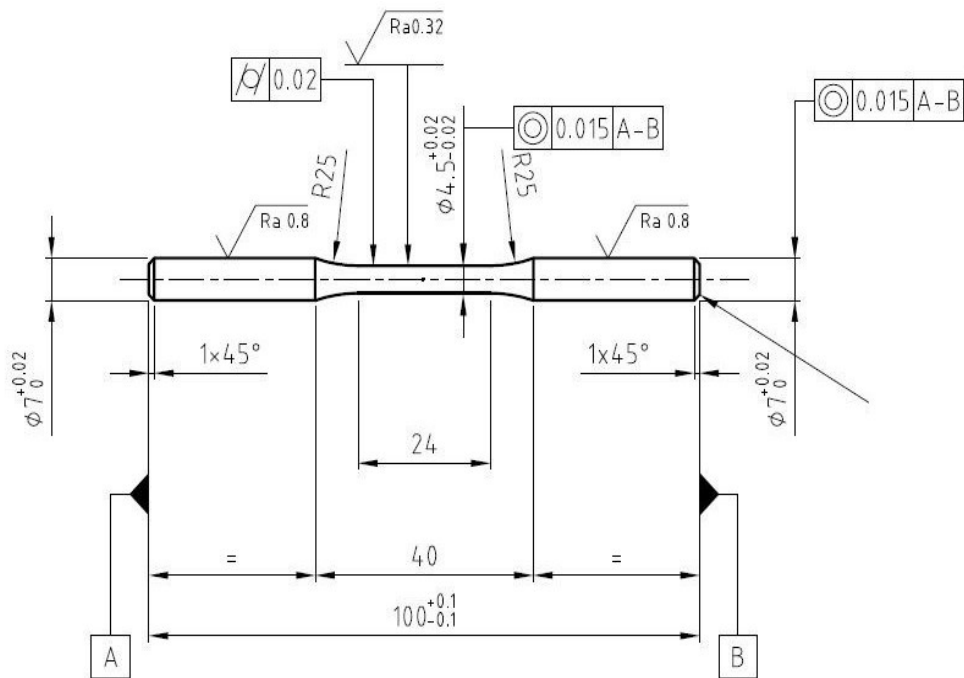


Figure 4.2: Specimen geometry

Furthermore, additional checks were made:

- **Roughness**

Thanks to a roughness meter, every part of the specimens was inspected (tangs, junctions and central cross section) to know if the standard limits were respected. If not, an accurate polishing was made and the roughness re-checked.

- **Visual Inspection**

This operation is mandatory to avoid any scratch or surface defect that could affect the test.

- **Mounting procedure**

The specimen was clamped thanks to a torque wrench and the tangs were covered with a thin layer of anti-fretting paste that prohibits the rubbing of the specimen inside the machine. After that, the rotational speed was kept at a low level to verify the correct mounting and the screws of the moving head were tightened so as to obtain two fixed supports.

This procedure had the purpose *to avoid any brake of the specimens that is not caused by a non metallic inclusion.*

Staircase analysis

The rotating bending machine rotates and bends the specimen. The inclusion content of the steel was tested through several specimens of different *staircase analyses*: this method allows to estimate the fatigue limit of the steel. It consists of testing the first specimen at a stress condition that is supposed to be about the fatigue limit of the material: if it reaches the life target without failing, the next specimen is tested at a higher stress condition; otherwise, in case of failure, the stress level of the next specimen is reduced. The $\Delta\sigma$ is fixed before starting the test campaign.

The load applied at the minimum cross section is controlled by a PC software, as the rotational speed. The test characteristics were:

- Stress frequency: 58.3 Hz (3500 rpm)
- Test machine loading system: 4 points
- Life target: $5 \cdot 10^6$ cycles
- $\Delta\sigma = 25$ MPa



Figure 4.3: Rotating bending machine

4.1.2 Test Rigs for bearing balls

The fatigue test of the balls was designed in order to single out the failure cause only on the tested balls without damaging the other parts of the bearing, like the inner ring, outer ring and cage. In order to ensure the reliability of different tests and so to have the same test conditions, a process protocol that is established since many years, was adopted. The same test conditions are mandatory to compare the fatigue life of different balls, respect to the inclusion presence and properties. Because of the high contact pressure between the balls and the raceways, it could be possible to have a damaging of inner and outer rings that consequently generates balls damaging which invalidate the test.

Rigs structure and properties

Each test bench (Fig. 4.4) is made up of a shaft in which are assembled two types of 1st generation HUB bearings::

- Angular contact ball bearing ($\phi 11, 112 mm$)
- Angular contact ball bearing ($\phi 10, 500 mm$)

The shaft is connected to an electric motor that transmit the rotation. A hydraulic piston driven by a pneumatic one, provides the axial load to the bearings. The loaded side of the shaft is the one with $\phi 11, 112 mm$ balls, and the study is focused on those balls, not on the $\phi 10, 500 mm$ ones. The latter ones have only a support function.

The test bench is able to detect:

- vibrations through an accelerometer
- temperature through to a thermocouple
- load level through to a load cell

Both the accelerometer and the thermocouple are placed on tested bearings (balls with $\phi 11, 112 mm$). These two sensors are very important for the management of the tests, indeed every variation of the nominal condition may have important consequences. For this reason, the three parameters display real time on the computer monitor connected with test rigs and for each minute of the test, temperature and vibrations are recorded.

- A high level of load may produce high pressure on balls that leads to premature failure
- A high temperature can arise due to excessive or limited lubricant, or a marked roundness of the balls and so excessive contact pressure
- A high level of vibrations may suggest a marked roundness of the balls or a failure of one of the bearing components.

The tested bearing mounts only one row of 7 balls (instead of 14 balls) to increase the contact pressure between the rings and the tested balls. Only one row is necessary since there's unidirectional load. The grease is the Shell Gadus S3 V220.

Regarding the no-tested bearing, only one cage is assembled (as explained for the tested case) with a complete set of 15 balls. The grease in this case is the Shell Gadus S2 V100.

The cleanliness during the assembly is mandatory, since any contamination of the lubricant can lead to a reduction in the bearing fatigue life.



Figure 4.4: Test rigs for balls bearing tests

Test procedure

The test conditions are summarized below:

- Ball diameter: $\phi 11,112\text{ mm}$
- Ball material: 100Cr6
- Ball number in each test bearing: 7
- Ball number in each no-test bearing: 15
- Applied Load: 34400 N
- Grease for tested balls: Shell Gadus S3 V220
- Grease for tested balls: Shell Gadus S2 V100
- Load limit: 37500 N
- Vibration limit: $15\frac{\text{mm}}{\text{s}^2}$
- Temperature limit: 145° C
- Releasing load interval: 25s every 300s
- Data acquisition period: 60s

The test can start when the two bearings are mounted on the shaft and the bench is correctly assembled. During the firsts 10 minutes, the load is only the 30% of the nominal one to obtain a homogeneous distribution of the lubricant and the optimal centering of the shaft. After this short time, the load is raised until the nominal one. Every 5 minutes the load is released for 25 seconds to allow the spinning of the balls.

Each 20 hours the rigs are stopped so as to change the rings, the lubricant, the cages, and the balls of the no-tested bearing. In this way, the element of the bearing that will fail earlier will be the ball in most cases.

It is possible to have premature stops due to:

1. High temperature

If the temperature overcomes 145° C , the machine stops. This temperature was chosen because 150° C is the tempering temperature of the steel, over this limit there is the possibility of microstructural changes (hardness reduction) of the rolling elements and then a reduction of fatigue life.

2. Vibrations

When the vibrations level is higher than $15\frac{mm}{s^2}$, the machine stops. That level was chosen according to the testing developed experience: if a lower level is set, the machine would stop for external vibrations and if a higher level is set, a ball could be broken but the machine would not stop, ruining the test.

3. Load

In order to prevent the overload, the test is stopped if the load limit is exceeded.

At every stop of the bench, it must be disassembled and cleaned. The components must be inspected completely, and different situations can arise:

- Stops **before** 20 hours:
The test bearing has to be inverted or changed if both sides have been already used, while the rings of the support bearing can be maintained if they are in good status. The $\phi 10,500\text{ mm}$ balls have to be changed.
- **Programmed** stops at 20 hours:
Both the test bearing and the support bearing must be inverted or changed, as the $\phi 10,500\text{ mm}$ balls.

After this operation, everything is lubricated and assembled. This accurate maintenance ensures that the balls break first. Moreover, at each stop, the roundness and weight of the balls is measured to know the damage evolution. The test is considered finished in two cases:

- Failure of the tested balls
- Excessive vibrations or temperature due to a marked roundness of the balls.

4.1.3 After failure analyses - Spheres

When one ball had failed, the after failure analyses started. Here the procedure is presented:

1. A stereomicroscope inspection was made on each failed ball, to evaluate if the failure started from an inclusion. In this case, few photos at different magnification were taken.
2. The SEM (Fig. 4.6) analysis allowed to know the chemical composition and the dimension of the inclusion.
3. The inclusion depth was evaluated thanks to a gauge meter (Fig. 4.5).



Figure 4.5: Gauge meter

4.1.4 After failure analyses - Specimens

Similarly to the failure analyses of the spheres:

1. An optical inspection was made on the fracture of the specimen, few photos at different magnification were taken and the distance from the surface and the dimension of the inclusion were detected.
2. The SEM (Fig. 4.6) analysis allowed to know the chemical composition and dimension of the inclusion.



Figure 4.6: Scanning Electron Microscope

4.2 Stresses calculation

Since the inclusion depth was known, it was possible to calculate the stress at the corresponding position, both for spheres and specimens. The Tresca and von Mises equivalent stresses were evaluated:

- the first one states that the yielding of the material is reached when the maximum tangential stress reaches a threshold value $\tau_{max} = k$. In this case the stress limit is:

$$\tau_{max} = \left\{ \frac{|\sigma_I - \sigma_{II}|}{2} \right\}, \left\{ \frac{|\sigma_{II} - \sigma_{III}|}{2} \right\}, \left\{ \frac{|\sigma_I - \sigma_{III}|}{2} \right\}$$

- the second one claims that the yielding occurs when the deformation distorting strain reaches a limit value. The stress limit is:

$$\sigma_{id,VM} = \frac{1}{\sqrt{2}} \sqrt{(\sigma_1^2 - \sigma_2^2)^2 + (\sigma_2^2 - \sigma_3^2)^2 + (\sigma_1^2 - \sigma_3^2)^2}$$

These stresses are the 'ideal' ones, that do not consider the presence of the inclusion: they will be modified by the Eshleby solver.

In the sphere case, the Hertz theory was used, while in the specimen case the stress can be computed easily from the De Saint Venant theory.

4.2.1 Hertzian stress - Spheres

Starting from the geometry of the contact and the load applied, the distribution of the stress under the surface is known. Only seven components of the tensor are different from zero, since the applied load is purely axial. Moreover, being two pairs of stresses equal, only five are significant.

To compute the equivalent stresses, the tensor with seven components was diagonalized in order to get a matrix with only the three principal stresses different from zero.

Load [N]	34400	
Max Hertzian pressure [MPa]	6001	
Contact ellipse semi-axes [mm]	1.934	0.431
Poisson ratio	0.35	
Young modulus [GPa]	210	

Table 4.1: Contact parameters

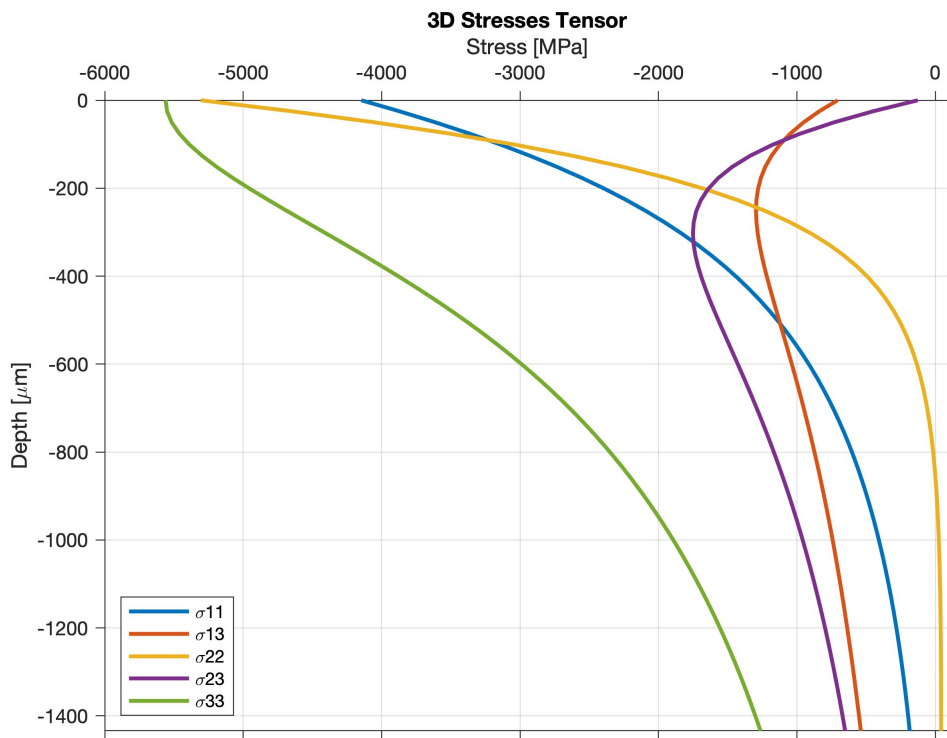


Figure 4.7: Sub-surface stresses, corresponding to 34400 N

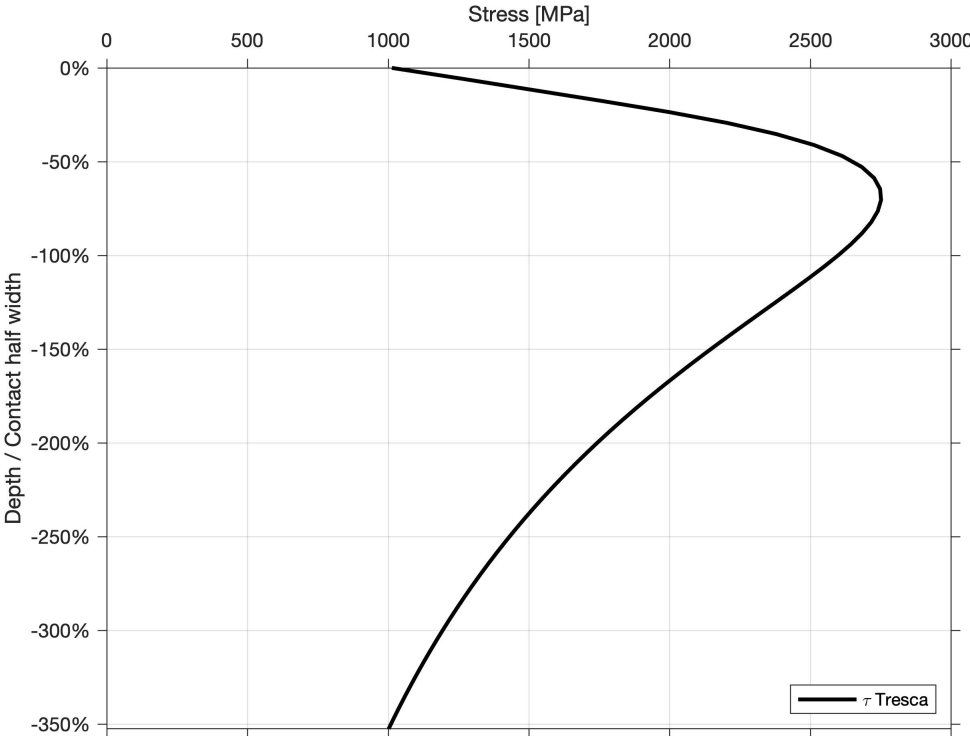


Figure 4.8: Sub-surface Tresca Stress, corresponding to 34400 N

4.2.2 Stress - Specimens

The rotating bending machine applies the force as shown in Fig. 4.9.

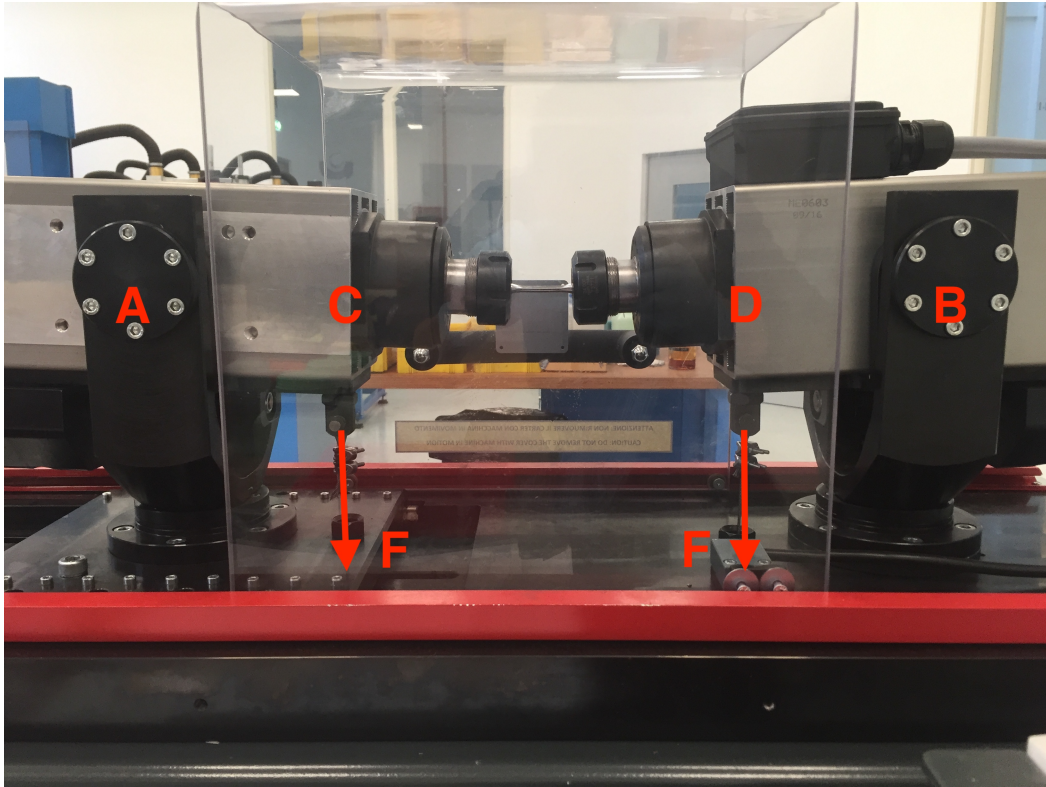


Figure 4.9: Rotating bending machine - Load condition

The applied stress on the specimen can be found starting from the free body diagram (Fig. 4.10):

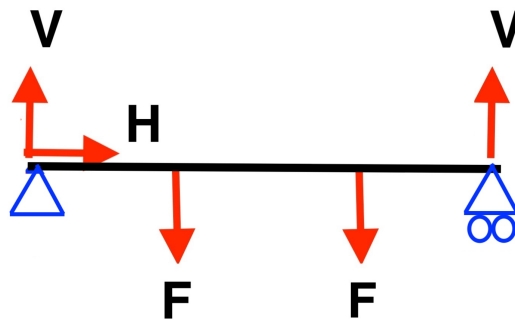
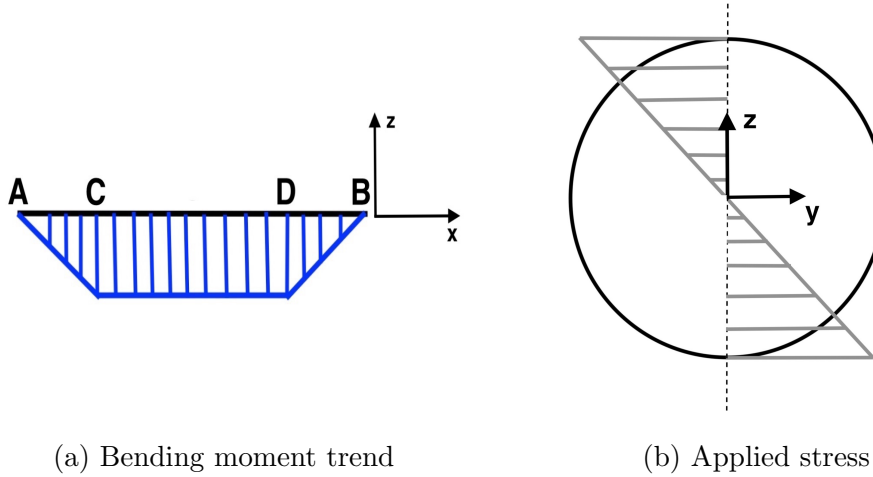


Figure 4.10: Free body diagram

Since the geometries of the machine and of the specimen are known, the bending moment trend and the applied stress are:



(a) Bending moment trend

(b) Applied stress

The load applied from the machine generates a uniform bending moment on the specimen (Fig. 4.11a), for this reason the applied stress from point C to point D changes only because of the variation of the cross section area. In the central part of the specimen the stress is maximum, because the cross section area is minimum (Fig. 4.11b).

At this point, knowing the applied stress at the surface, it was possible to know the stress at each depth changing the y coordinate, and so the 'ideal' stress at the inclusion level.

In the specimen case, there is only one principal stress, so the corresponding Tresca one is:

$$\tau_{max} = \frac{\sigma_{xx}}{2}$$

4.2.3 Stress variation

All the data required from the Eshelby solver was known (inclusion dimension, depth, chemical composition and configuration, stress at the inclusion depth). To have a complete description of how the solver works, please see chapter 5.2.

It is necessary to underline that the third dimension of the inclusion it is not easy to determine, in this study the one along the **z-axis**. Nevertheless, thanks to the experience, it's possible to say that it is similar to one of the two other dimensions. When the inclusion detaches from the surface fracture, it is possible to detect the third dimension and in every case it is similar to the others dimensions. Moreover, since the stress analysis was performed on the **xy plane** the **z** dimension in not affecting the stress field.

The code reads the input stress tensor at the correct depth from an Excel file and, with all the inclusion data, it calculates the 'new' stress tensor and the Tresca and von Mises stresses. Moreover, it plots a 3D graph in which the stress state inside and outside the inclusion. The grid limits were chosen with respect to the perturbation of the stress state due to the inclusion: when the stress outside the inclusion decreases at the matrix-free level the grid is interrupted.

Chapter 5

Model

5.1 Eshelby model

The Eshelby model allows to compute the stress field around an ellipsoidal inclusion. A region (inclusion) in an infinite homogeneous, isotropic and elastic medium (matrix) undergoes a change of shape and size. Under the constraint of the matrix, the inclusion has an arbitrary homogeneous strain. The objective is to evaluate the elastic fields of the inclusion and of the matrix [4].

Eshelby investigated the elastic fields thinking to cut round a generic region and removing it from the matrix. In this way the region can change its shape, since it is unconstrained. Then, applying forces to the region and so restoring it to its original form, put it back in the matrix. The stress is now zero and has a constant value inside the inclusion. The applied surface tractions have become built in as a layer of body force spread over the interface between matrix and inclusion. To complete the solution, this unwanted layer is removed by applying an equal and opposite layer of body force; the additional elastic field thus introduced is found by integration from the expression for the elastic field of a point force [4].

The result that Eshelby found was that if the inclusion is ellipsoidal and the matrix in which it is embedded is subjected to an homogeneous load, the stress within the inclusion is uniform. This means that the elastic stress and strain **don't change** with the position inside the inclusion.

Mura [17] defined an inclusion as a subdomain Ω in a domain D . The eigenstrain $\epsilon_{ij}^*(x)$ is given in Ω and zero in $D - \Omega$. This is the inclusion problem, as the elastic modulus is the same for both subdomain and domain. The displacement u_j , strain ϵ_{ij} , and stress σ_{ij} are expressed by [17]:

$$u_i(\mathbf{x}) = -C_{kjmn} \int_{\Omega} \epsilon^*(\mathbf{x}') G_{ij,k}(\mathbf{x}-\mathbf{x}') d\mathbf{x}' \quad (5.1)$$

$$\epsilon_{ij}(\mathbf{x}) = -\frac{1}{2} \int_{\Omega} C_{klmn} \epsilon_{mn}^*(\mathbf{x}') (G_{ij,k}(\mathbf{x}-\mathbf{x}') + G_{jk,li}(\mathbf{x}-\mathbf{x}')) d\mathbf{x}' \quad (5.2)$$

$$\sigma(\mathbf{x}) = -C_{ijkl} \left(\int_{\Omega} C_{pqmn} * \epsilon_{mn}^*(\mathbf{x}') G_{kp,ql}(\mathbf{x}-\mathbf{x}') d\mathbf{x}' + \epsilon_{kl}^*(\mathbf{x}) \right) \quad (5.3)$$

where:

- C_{ijkl} is the stiffness tensor
- G_{ij} is Green's function
- \mathbf{x} is the position vector
- \mathbf{x}' denotes the position of a point source

Since the strain and stress fields inside the inclusion are uniform:

$$\epsilon_{ij}(\mathbf{x}) = S_{ijkl} \epsilon_{kl}^* \quad \text{for } \mathbf{x} \in \Omega \quad (5.4)$$

with S_{kl} as the Eshelby tensor [17]. This tensor contains several integrals, approximated with tolerance of order 10^{-16} by the MATLAB function **elliptic12** [13], the solutions are quasi-analytical [17].

Regarding the strain field outside the inclusion:

$$\epsilon_{ij}(\mathbf{x}) = S_{ijkl} \epsilon_{kl}^* \quad \text{for } \mathbf{x} \in D - \Omega \quad (5.5)$$

Having this expression of the strain for both inside and outside the inclusion, the stress can be obtained as follows:

$$\sigma_{ij} = C_{ijkl} \epsilon_{kl}(\mathbf{x}) \quad (5.6)$$

5.1.1 Equivalent inclusion method

If the elastic field that has to be evaluated is characterized by different elastic moduli, as the subdomain moduli is different from the one of the matrix, this makes the problem different. In this case the problem is called '*the inhomogeneity problem*', while in the case of the same elastic modulus it is

called '*the inclusion problem*'. The correlation between the two was argued by Eshelby [4]: the stress perturbation due to the presence of an ellipsoidal inhomogeneity of an homogeneous applied stress σ_{ij}^∞ , can be determined by an inclusion problem when the eigenstrain ϵ^* is chosen correctly. This is called the equivalent inclusion method [16].

Mura [17] gives the strain and stress fields as follows:

$$\epsilon_{ij} = \epsilon_{ij}^\infty + S_{ijmn}\epsilon_{mn}^* \quad (5.7)$$

$$\sigma_{ij} = \sigma_{ij}^\infty + C_{ijkl}(S_{klmn}\epsilon_{mn}^* - \epsilon_{mn}^*) \quad \text{for } \mathbf{x} \in \Omega \quad (5.8)$$

$$\epsilon_{ij}(\mathbf{x}) = \epsilon_{ij}^\infty + D_{klmn}(\mathbf{x})\epsilon_{mn}^* \quad (5.9)$$

$$\sigma_{ij}(\mathbf{x}) = \sigma_{ij}^\infty + C_{ijkl}D_{klmn}(\mathbf{x})\epsilon_{mn}^* \quad \text{for } \mathbf{x} \in D - \Omega \quad (5.10)$$

Note that equations (5.7)(5.9) are similar to (5.4)(5.5) respectively, but the equations describing the equivalent inclusion method (5.7)(5.9) have the term ϵ_{ij}^∞ that represent a remote strain induced by the homogeneous stress σ_{ij}^∞ . The same goes for the equations regarding the stress (5.8)(5.10), but here the eigenstrain is *stress-free*, so it has to be subtracted from the total strain when calculating the stress inhomogeneity.

5.2 Numerical solver

In order to evaluate the effects of various types of inclusions and matrices, a 3D numerical MATLAB solver that implement the Eshelby solution was used. In particular, it allowed to determine the stress field around the microinclusion. Healy [3] proposed a MATLAB code that was able to consider the Eshelby solution for an inclusion with semiaxes $a_1 = a_2 \neq a_3$. The one that was used in this work, allows to consider a general ellipsoidal inclusion or inhomogeneity with three different semiaxes, and it is based on the one developed by Meng et al. [16]. The code has been revisited to adapt it to the particular case of inclusions in ball bearings. As explained by Meng et al. [16], the main script, **incl_prob** handles the input data structure, calls the Eshelby solver, **Esh_sol**, and presents the results. The input structure **incl** has attributions:

- E_m Young's modulus of the matrix
- v_m Poisson ratio of the matrix
- E_h Young modulus of the inhomogeneity
- v_h Poisson ratio of the inhomogeneity
- *dim* the ellipsoidal dimensions a_i
- *ang* rotation angles around coordinate axes
- *stressvec* remote stress σ_{ij}^∞
- *eigp* initial eigenstrain ϵ_{ij}^p
- *grid* observation grid(s) where we evaluate the solutions

where the stress and strain tensors are in the form of six-component vectors because of the symmetry. The **Esh_sol** function reads the input data and output arguments, "disp", "stress" and "strain". The routines called by this function in the order of appearance:

Ctensord constructs the stiffness tensors C_{ijkl} and C_{ijkl}^* for given elastic moduli (E_m, v_m) and (E_h, v_h) . From the stress-strain correspondence, (5.6), it's possible to calculate the remote strain ϵ_{ij}^∞ for the remote stress σ_{ij}^∞ . Note that if $C_{ijkl} = C_{ijkl}^*$, $\sigma_{ij}^\infty = 0$ and $\epsilon_{ij}^p \neq 0$, it is the original inclusion problem.

Esh_int constructs the Eshelby tensor S_{ijkl} for a given v_m and ellipsoid dimension a_i . With C_{ijkl}^* , ϵ_{ij}^∞ and S_{ijkl} it's possible to calculate the fictitious

eigenstrain ϵ_{ij}^* .

Esh_D4 constructs the tensor $D_{ijkl}(x)$ for given v_m , a_i and coordinates x_i .

With D_{ijkl} , it's possible to calculate the exterior strain and stress.

Esh_disp constructs the displacements u_i for given v_m , a_i , x_i , and ϵ_{ij}^* .

Esh_D4_disp merges the functionalities of **Esh_D4** and **Esh_disp**.

Since the objective is to find the stress field perturbation, only **Esh_D4** routine is chosen, the displacement given by **Esh_disp** it is not considered at this stage.

Chapter 6

Numerical Simulations

In order to evaluate the functionalities of the code and the different effects of the several parameters, numerical simulations were made. These numerical tests are based on experimental data coming from failures on test rigs, so the results should be truthful respect to the experimental cases. This means that, taking into account a real found microinclusion, the parameters were changed consciously, simulating the different effects on the stress field.

Before starting the parametric analysis, it is necessary to point out that the simulated load on the bearing is static and purely axial, and it's equal to the one applied at the test rigs for experimental tests.

Since the axial load on each ball it is known, as the geometry of the bearing, it is possible to evaluate the normal load (respect to the contact). Thanks to the Hertz theory and the Poisson ratio of the bearing material, the contact pressure can be estimated, as the pressure tensor at each depth (Fig. 6.1). The tensor found at the depth at which the inclusion is present, is the input of the code.

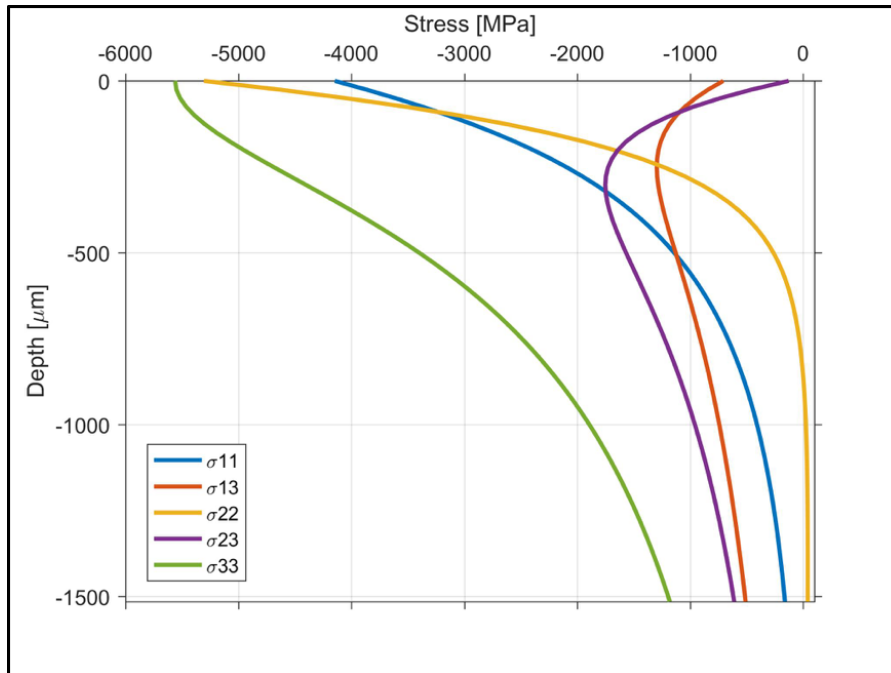


Figure 6.1: Sub-surface stresses, axial load equal to 34400 N

6.1 Dimension

The inclusion size affects the stress field around the inclusion: increasing the inclusion dimension, the area subjected to a stress perturbation increases. On the other hand, the Tresca stress peak value does not change significantly (Table 6.1). These results agree to what Guan et al. [9] and Moghaddam et al. [14] found. Obviously, a larger inclusion can be located at the critical depth with an higher probability respect to a smaller one.

Regarding a ball bearing case, having a larger stressed area, it means that it will be subjected to the load more frequently.

Stress peak increment at NMI boundary		
Size of the semiaxis [μm]		Tresca peak Increment
<i>From</i>	0.5x0.5x0.5	+39%
<i>To</i>	50x50x50	+39%

Table 6.1: Effect of the inclusion dimension

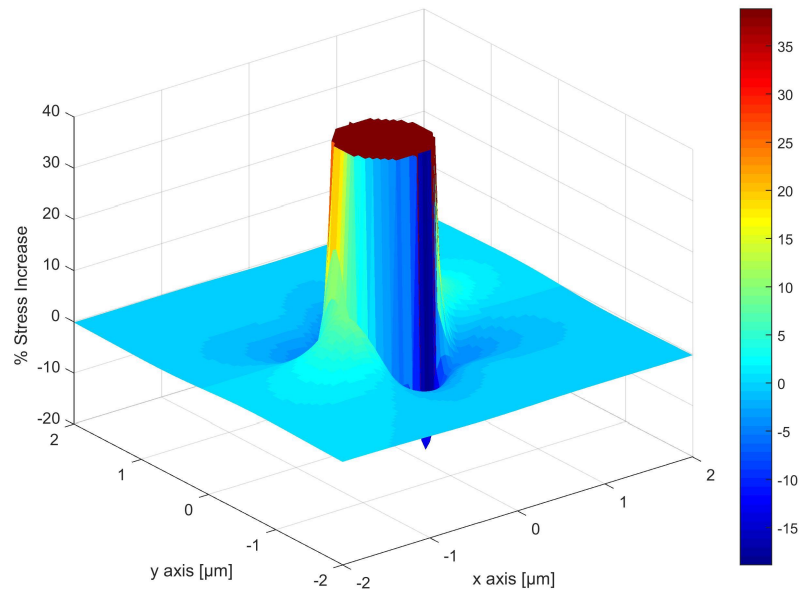


Figure 6.2: Stress perturbation due to a spheroidal inclusion - $0.5 \mu m$ radius

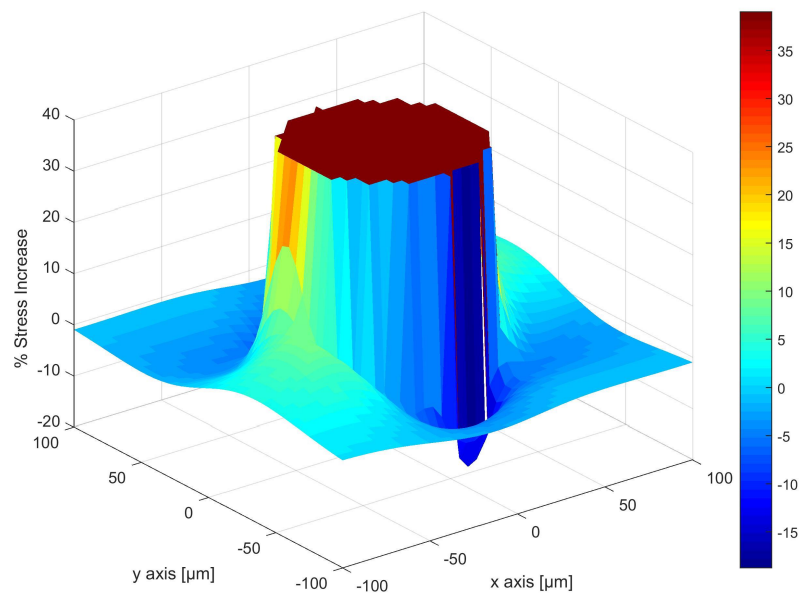


Figure 6.3: Stress perturbation due to a spheroidal inclusion - $50 \mu m$ radius

6.2 Shape

Changing the two semiaxes of the inclusion perpendicular to the force direction, the effect of the shape has been evaluated. The force direction is parallel to the \mathbf{z} -axis, so the two semiaxes are directed as \mathbf{x} and \mathbf{y} . The ratio between the two has been changed until one order of magnitude and the results are showed below (Table 6.2):

Stress peak increment at NMI boundary		
Case number	Shape [y/x]	Tresca peak Increment
1 st	1	+39%
2 nd	2	+42%
3 rd	10	+49%

Table 6.2: Effect of the inclusion shape

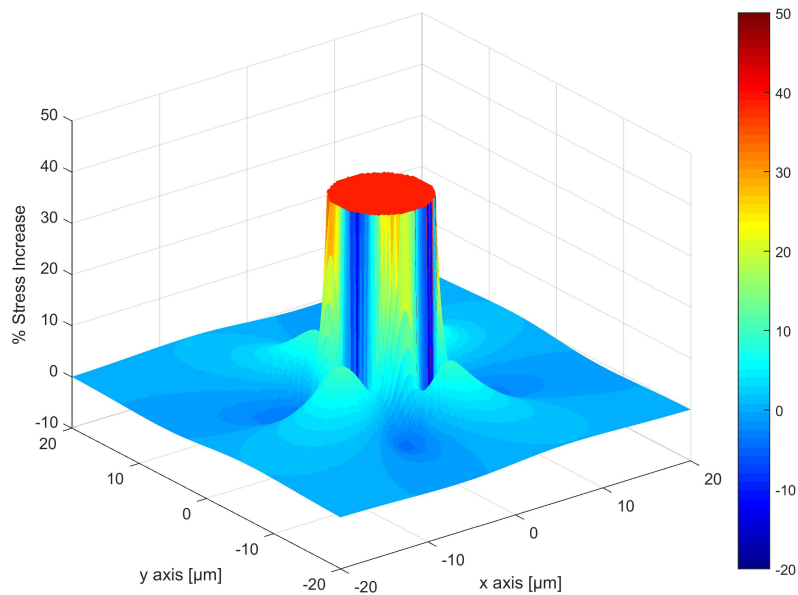


Figure 6.4: Stress perturbation: effect of the shape - 1st Case

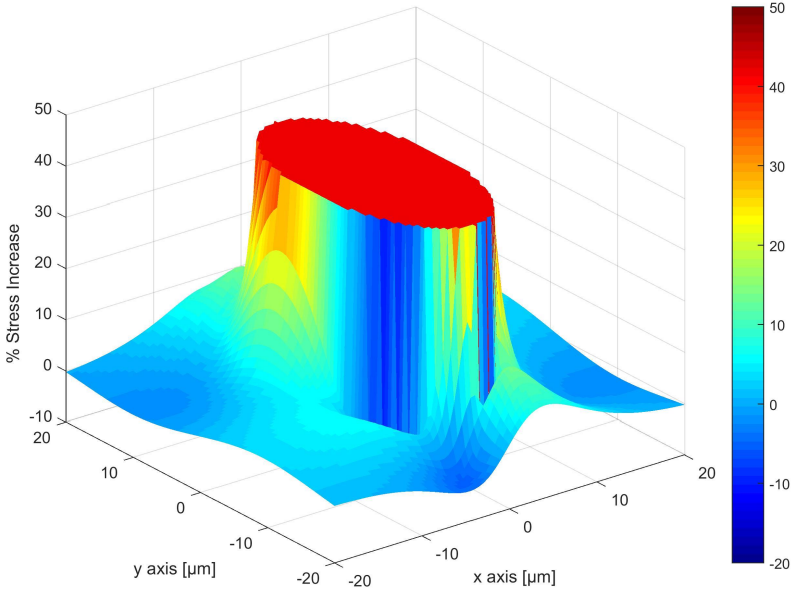


Figure 6.5: Stress perturbation: effect of the shape - 2nd Case

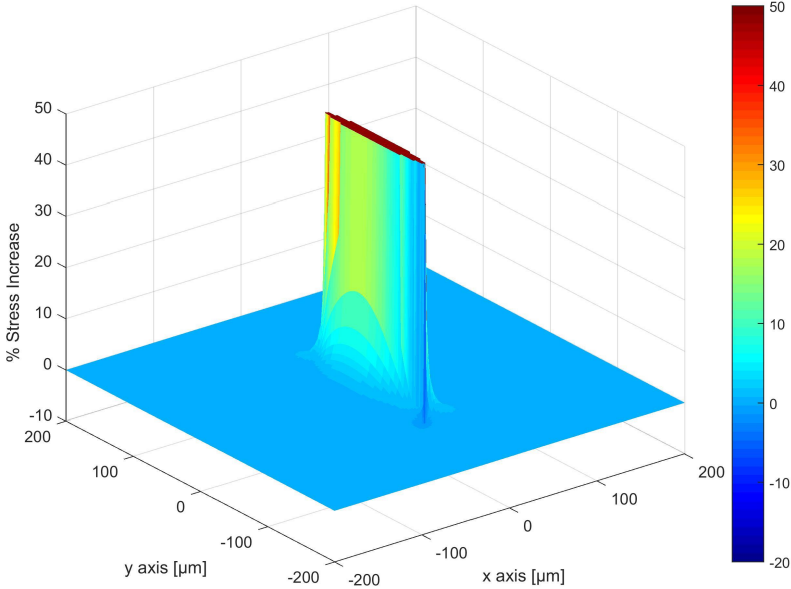


Figure 6.6: Stress perturbation: effect of the shape - 3rd Case

The shape plays an important role on the stress increment at the inclusion boundary, if the semiaxes ratio increases, the stress peak increases in a not negligible way.

6.3 Depth

An important factor for the stress peak at the inclusion boundary is the depth at which the inclusion is located. From the Hertz theory, it is known that the maximum equivalent stress is located at a certain depth below the surface. This depth can be identified, with a good approximation, as:

$$Depth_{\sigma_{eq,max}} = 0.75 \cdot b$$

where b is the contact half width.

The stress increment [%] due to the NMI remains the same independently from the depth as shown in Table 6.3. At the critical depth, the original stress calculated by Hertz is maximum, so the absolute increase is larger, Fig. 6.7.

Stress peak increment at NMI boundary		
Case number	Depth/b	Tresca peak Increment
1 st	35%	+39%
2 nd	71%	+39%
3 rd	175%	+39%

Table 6.3: Effect of the depth

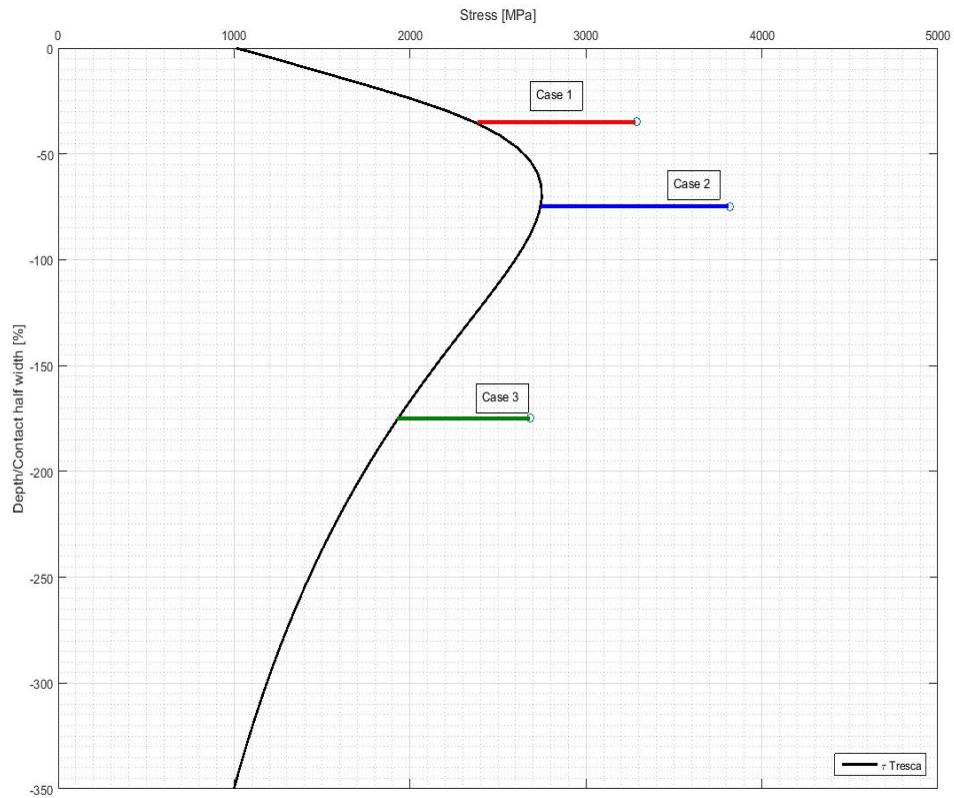


Figure 6.7: Stress perturbation: effect of the depth

6.4 Chemical composition

6.4.1 Inclusion Composition

Most inclusions in bearing steels, are non metallic (**NMI**), and typically they are stiffer than the matrix. In fact, referring to experimental cases, few of the most common ones are Allumina (Al_2O_3), Titanium nitrides (TiN) and Titanium carbides (TiC) and each of them has an elastic modulus that is approximately **1.8 times or higher** than the elastic modulus of the pure steel. Also other types of inclusions can be found in steels, typically they are not detrimental as the ones presented above since they are not as stiff as those.

In the cases presented here, the peak increment remains almost the same (between +36% and +39%), but this effect is due to the very similar Young

modulus. Major changes on the elastic modulus will lead to larger increments, since they are related to the difference between E_m and E_h : if the ΔE increases, the peak increases.

Another parameter is the Poisson ratio (ν_m and ν_h), index of the shrinkage and the expansion of the sample. Similarly to what seen for the Young modulus, if the $\Delta\nu$ increases, also the peak increases.

Stress peak increment at NMI boundary		
Case number	Composition	Tresca peak Increment
1 st	Al_2O_3	+36%
2 nd	TiN	+36%
3 rd	TiC	+39%

Table 6.4: Effect of the composition

6.4.2 Matrix composition

Similarly to the inclusion case, the chemical composition of the matrix influences the stress field since ΔE and $\Delta\nu$ change considering the type of matrix. In this work, the matrix considered was only the 100Cr6, that is largely used for bearing production. Considering other bearing steel alloys, already used or in development, they can lead to negligible variations as the input value for calculations are Poisson ratio and Young's modulus.

6.5 Configuration

Experimental evidence shows that inclusions can appear in pairs, clusters and stringers. In order to be aligned with experimental cases and to the ASTM E45 Standard [5], few cases have been considered for the numerical analysis. The Standard provides a solution for the stringer case, that is considered with a minimum of three particles. In this case, the stringer can be considered as a stand-alone inclusion with an elongated semiaxes that covers the distance from the first to the last inclusion of the stringer.

As suggested by the E45 [5], the particles have to be placed at a certain distance limit from the centerline of the stringer itself, and the distance between

them has to be less than a certain threshold. Considering a stringer as a stand alone inclusion with elongated semiaxis, it is similar to what has been shown in the shape section (Table 6.2).

6.6 Conclusions

As proposed in [9], if the inclusion is far from the surface it will be not the main source of the spalling. According to the present research, in the worst case, the stress increase is approximately **+50%**.

The depth threshold below which the stress remains below the maximum stress calculated by Hertz is approximately **188%** the contact half width, Fig. 6.8. This result is in good agreement with [9, 14].

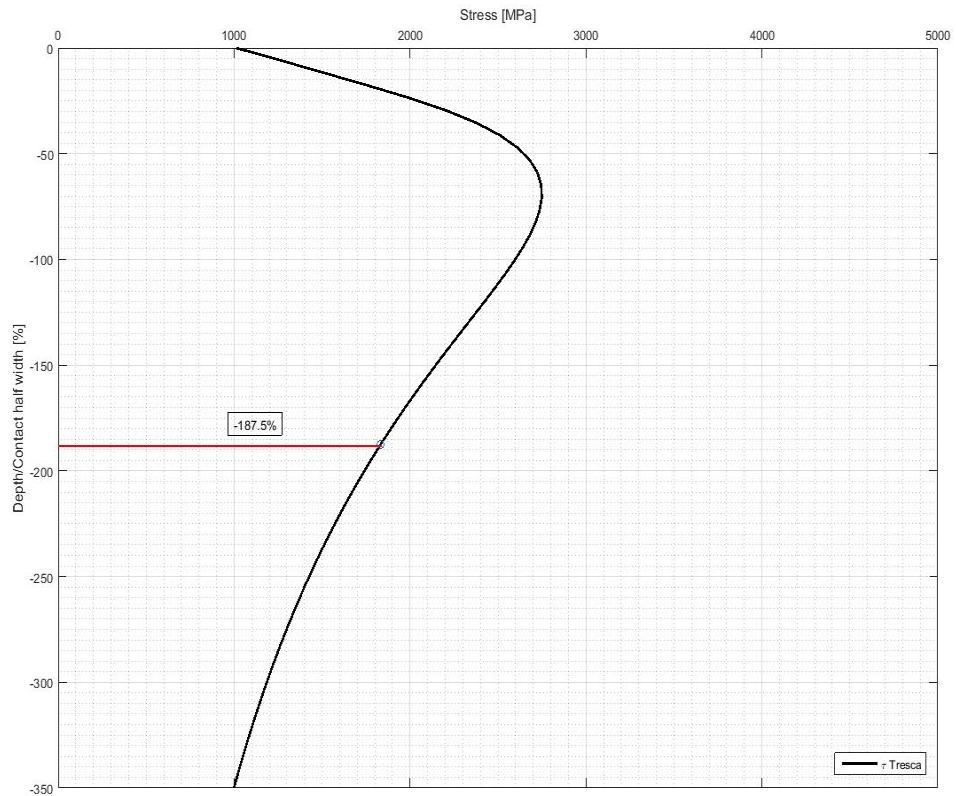


Figure 6.8: Depth threshold

Chapter 7

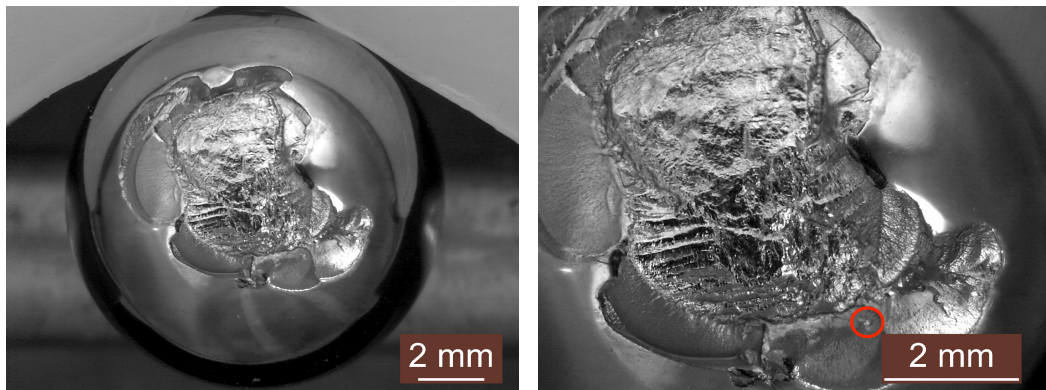
Failures on balls

Seven broken balls coming from test rigs were analyzed. In **five** cases more than one inclusion was present in the fractured area: for this reason the considered one was the one with the major increase of stress, since it was the worse from the fatigue life point of view. Nevertheless, also the other inclusions will be reported in the appendix A. Probably, also in the other **two** cases the balls had few inclusions, but it could happen that they remained under the material that was peeling.

Regarding the chemical composition, if the presence of some elements was negligible (evaluating the spectrum) these elements were neglected when considering the composition. Otherwise, if the presence of some elements was not negligible, a weighted average of them was performed to obtain the Young modulus and the Poisson ratio. It happened that for some inclusions, the dimensions were not clear, as the chemical composition and so the Young and Poisson parameters. Further clarifications are presented in this chapter.

7.1 Case 1

The test $n^{\circ} 1$ presented a failed ball after **11.2 [h]**. In this case, there was more than one inclusions in the fractured area. The one showed below is the most critical under the stress rise point of view. The fracture analyses at the optical microscope it is reported:



(a) 8x magnif.

(b) 16x magnif.

Figure 7.1: Test 1 - 11.2 h - Fracture inspection

The SEM analyses detected the inclusion dimensions and composition:

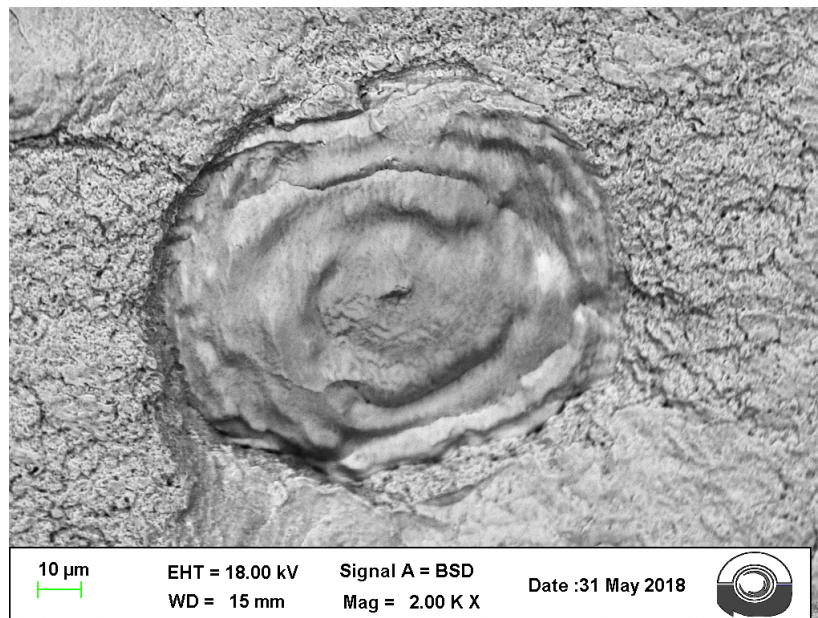


Figure 7.2: Test 1 - 11.2 h - 2000x magnif.

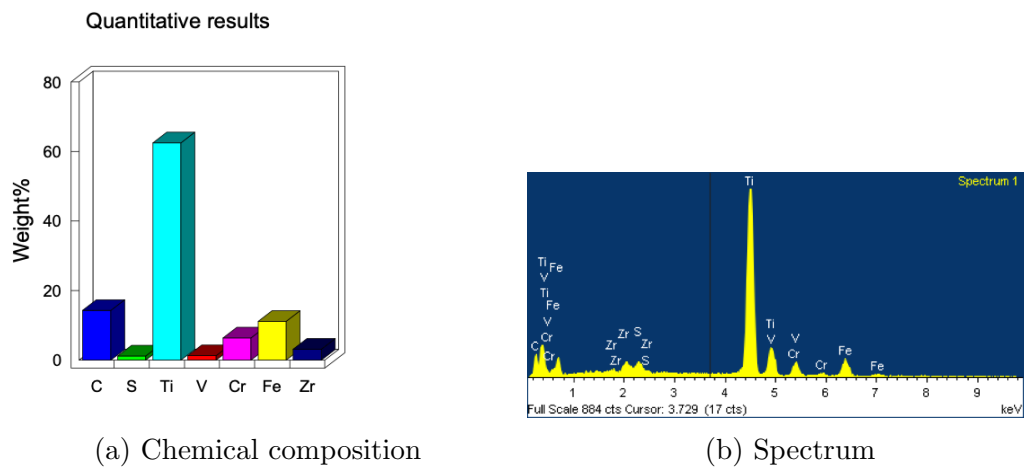


Figure 7.3: Test 1 - 11.2 h - SEM analyses

Since there are few elements in the inclusion slot, it's necessary to specify how the Young modulus is found: in this case the **TiC** composition was chosen, as the other elements (Cr, V, S, Zr) are in relatively small quantities and they have an elastic modulus that is quite small respect to the TiC. In this way, the adopted composition is the most critical one.

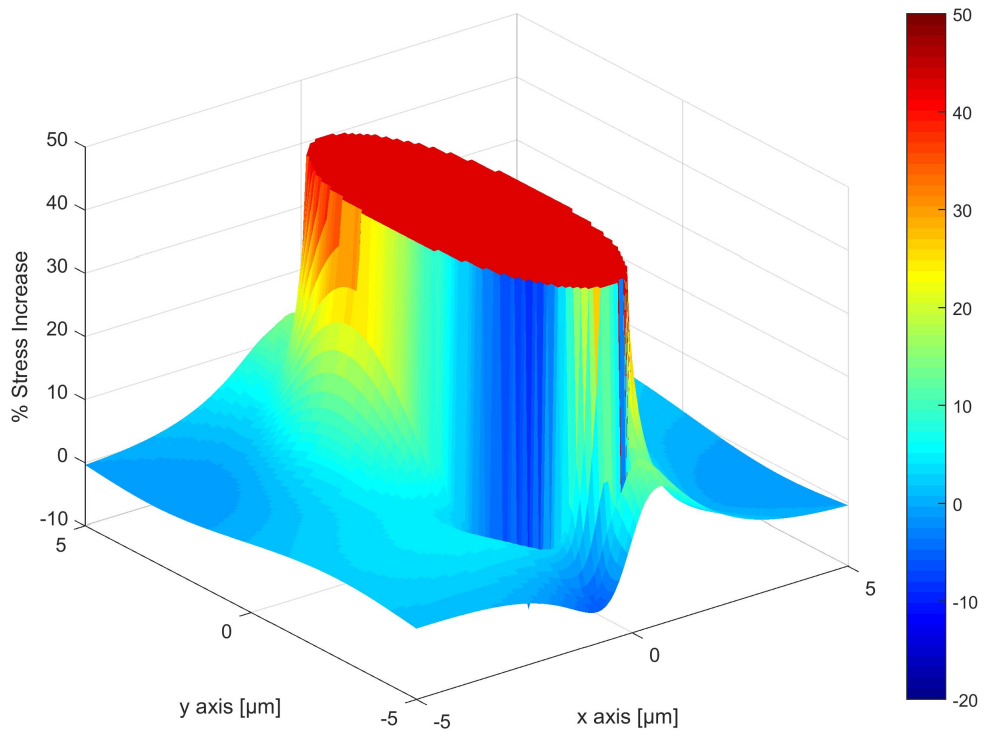


Figure 7.4: Test 1 - 11.2 h - Simulated stress inside and outside the inclusion

	Original	Maximum	Increase [%]
Tresca [MPa]	2319	3650	43
	Matrix	Inclusion	Ratio
Young Modulus [GPa]	210	380	1.81
Poisson Ratio	0.35	0.17	/
	x	y	z
Inclusion dimensions [μm]	1.67	4.34	1.67
Inclusion depth [μm]	-453		
Applied Load [N]	34400		
Cycles to failure [$\cdot 10^6$]	0.46		

Table 7.1: Test 1 - 11.2 h - Results

7.2 Case 2

The test $n^{\circ} 2$ presented a failed ball after **33.9 [h]**. Also in this case, there was more than one inclusion in the fractured area. The one showed below is the one chosen with the same criteria used for Case 1.

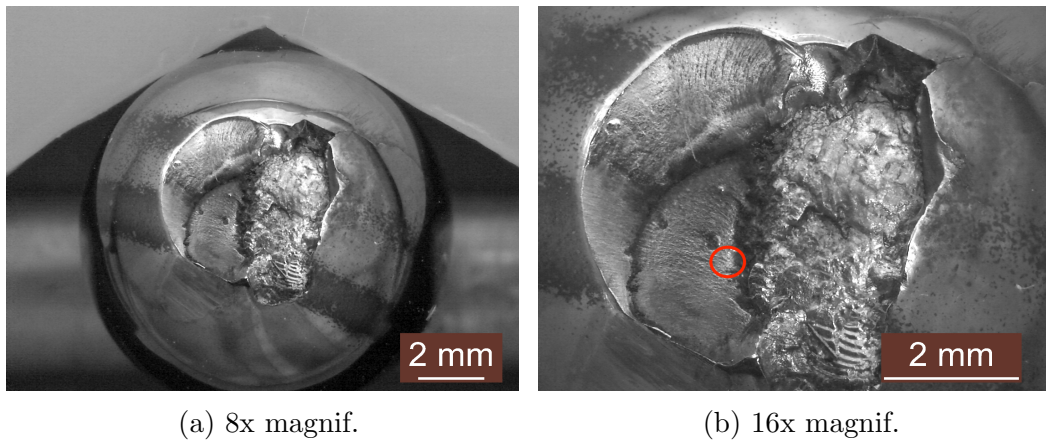


Figure 7.5: Test 2 - 33.9 h - Fracture inspection

The SEM analyses detected the inclusion dimensions and composition:

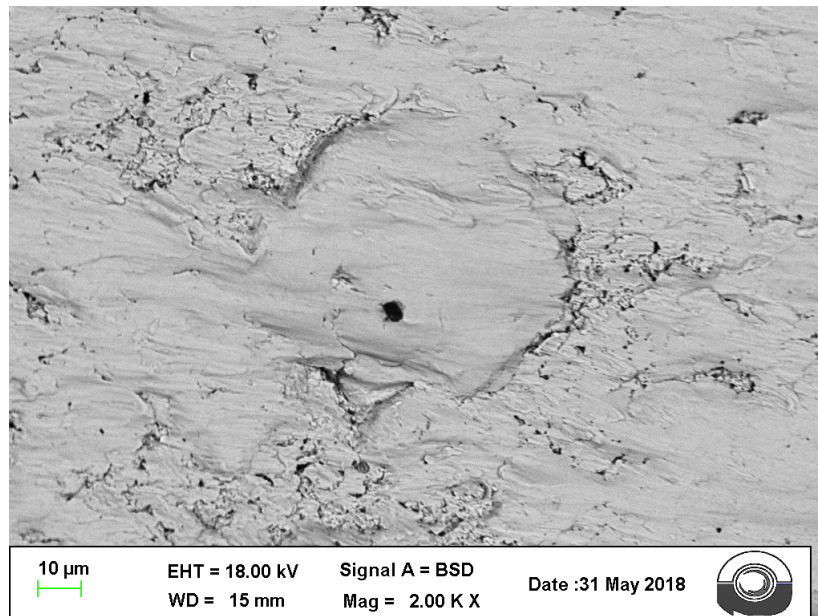


Figure 7.6: Test 2 - 33.9 h - 2000x magnif.

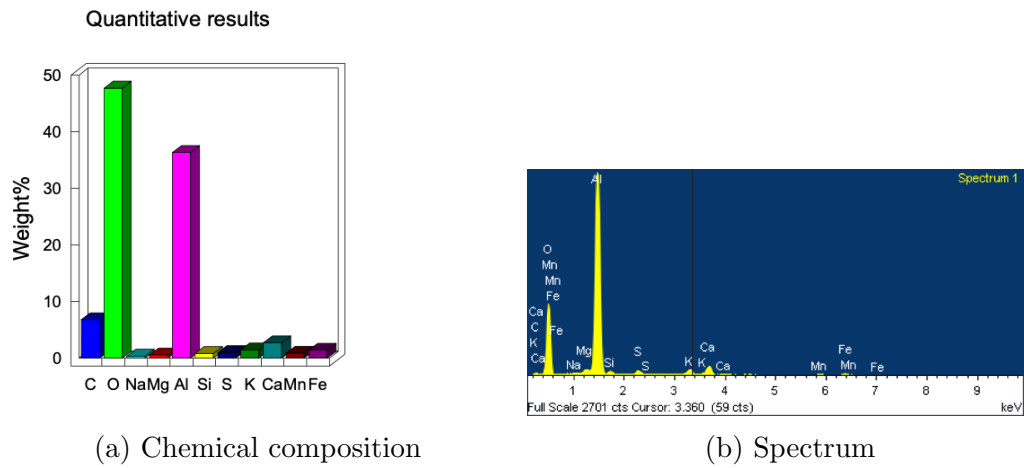


Figure 7.7: Test 2 - 33.9 h - SEM analyses

The inclusion composition is Alumina (Al_2O_3) with a minor presence of other oxides.

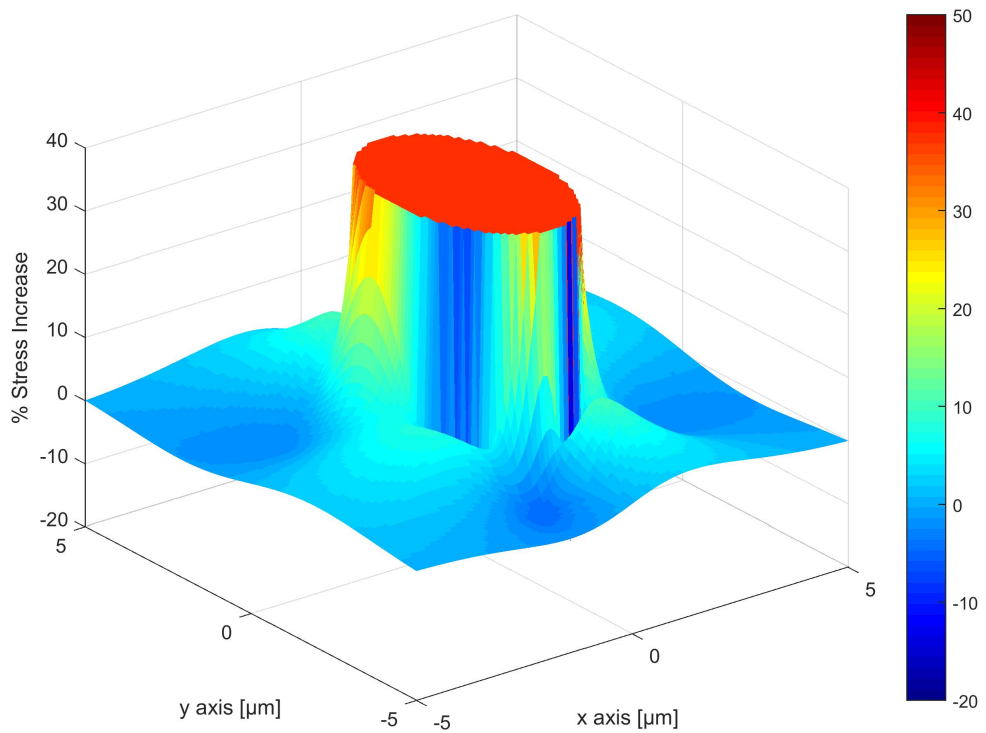


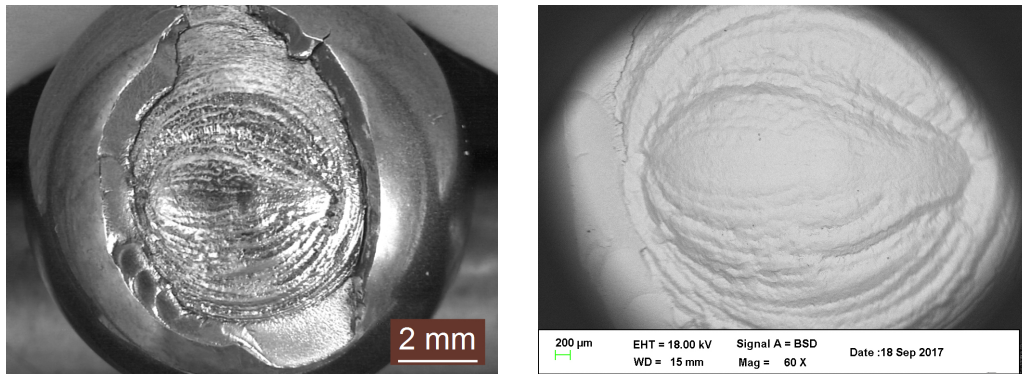
Figure 7.8: Test 2 - 33.9 h - Simulated stress inside and outside the inclusion

	Original	Maximum	Increase [%]
Tresca [MPa]	2319	3189	37
	Matrix	Inclusion	Ratio
Young Modulus [GPa]	210	375	1.79
Poisson Ratio	0.35	0.22	/
	x	y	z
Inclusion dimensions [μm]	1.67	2.67	1.67
Inclusion depth [μm]	-562		
Applied Load [N]	34400		
Cycles to failure [$\cdot 10^6$]	1.40		

Table 7.2: Test 2 - 33.9 h - Results

7.3 Case 3

The test $n^{\circ} 3$ presented a failed ball after **46.9 [h]**. Only one inclusion was found in the spalling area.



(a) 10x magnif.

(b) 60x magnif. - BSD

Figure 7.9: Test 3 - 46.9 h - Fracture inspection

The SEM analyses detected the inclusion dimensions and composition:



(a) 60x magnif. - SE1

(b) 700x magnif

Figure 7.10: Test 3 - 46.9 h - SEM fracture inspection

The inclusion is composed by different parts, as stated previously (chapter 6), it is considered as a stand alone inclusion with elongated semiaxes.

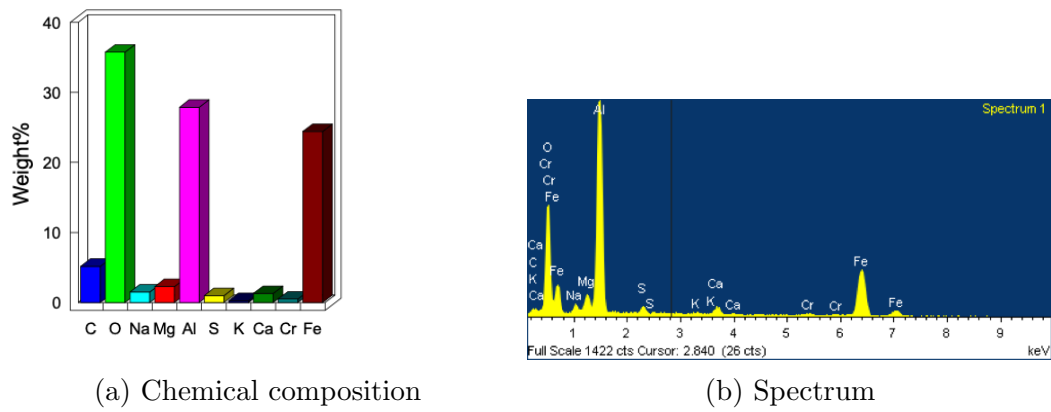


Figure 7.11: Test 3 - 46.9 h - SEM analyses

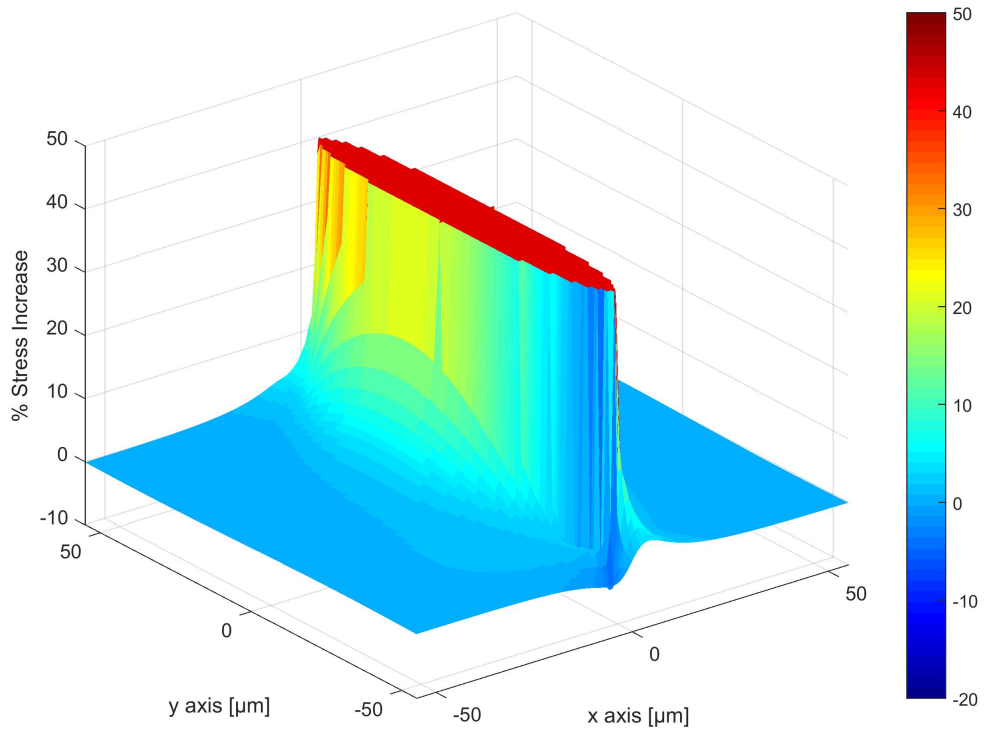


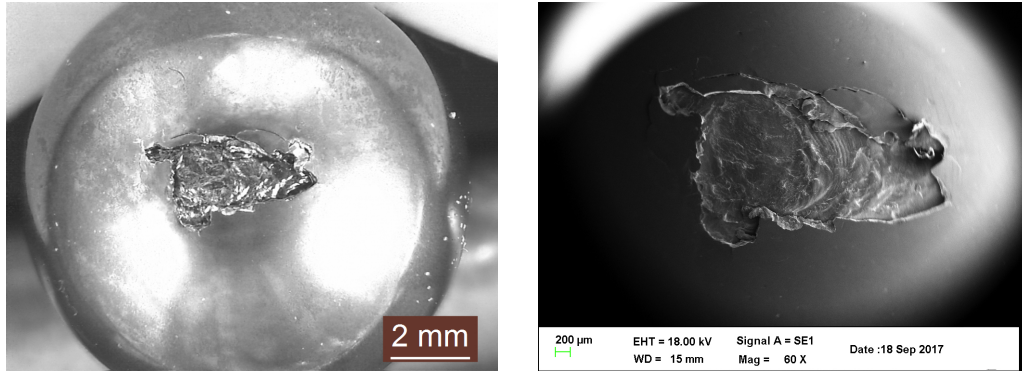
Figure 7.12: Test 3 - 46.9 h - Simulated stress inside and outside the inclusion

	Original	Maximum	Increase [%]
Tresca [MPa]	2210	3146	42
	Matrix	Inclusion	Ratio
Young Modulus [GPa]	210	375	1.79
Poisson Ratio	0.35	0.22	/
	x	y	z
Inclusion dimensions [μm]	7.00	49.00	7.00
Inclusion depth [μm]	-600		
Applied Load [N]	34400		
Cycles to failure [$\cdot 10^6$]	1.94		

Table 7.3: Test 3 - 46.9 h - Results

7.4 Case 4

The test $n^{\circ} 4$ presented a failed ball after **21.0 [h]**. The inclusion was found in the center of the spalling area.

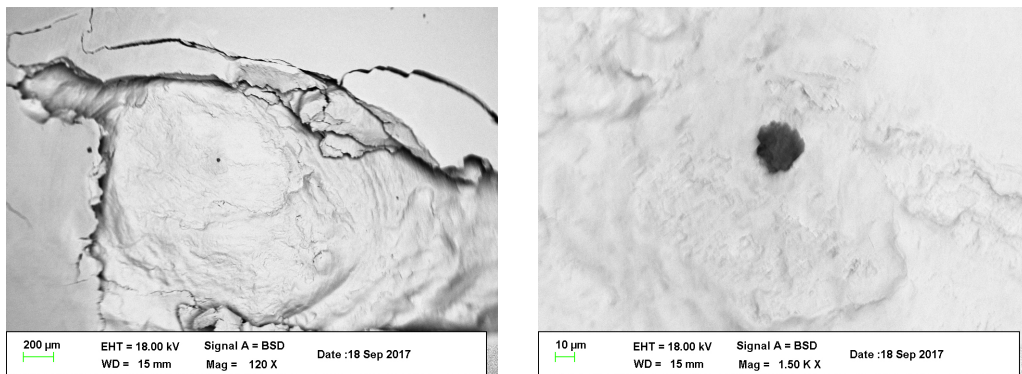


(a) 10x magnif.

(b) 60x magnif. - SE1

Figure 7.13: Test 4 - 21.0 h - Fracture inspection

The SEM analyses detected the inclusion dimensions and composition:



(a) 120x magnif. - BSD

(b) 1500x magnif - BSD

Figure 7.14: Test 4 - 21.0 h - SEM fracture inspection

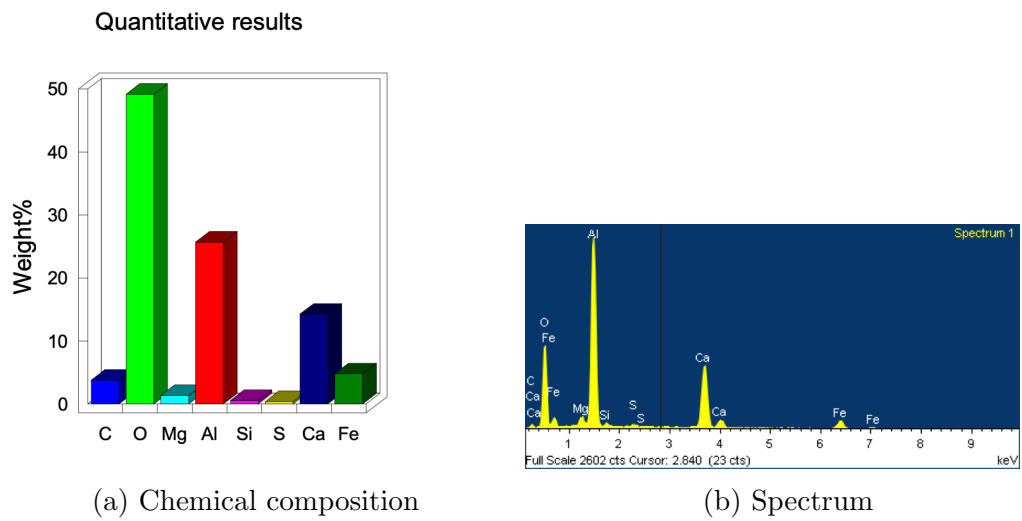


Figure 7.15: Test 4 - 21.0 h - SEM analyses

The inclusion has a circular shape, the three semiaxes are equal in size. The composition is Alumina (Al_2O_3) with a minor presence of Calcium oxides.

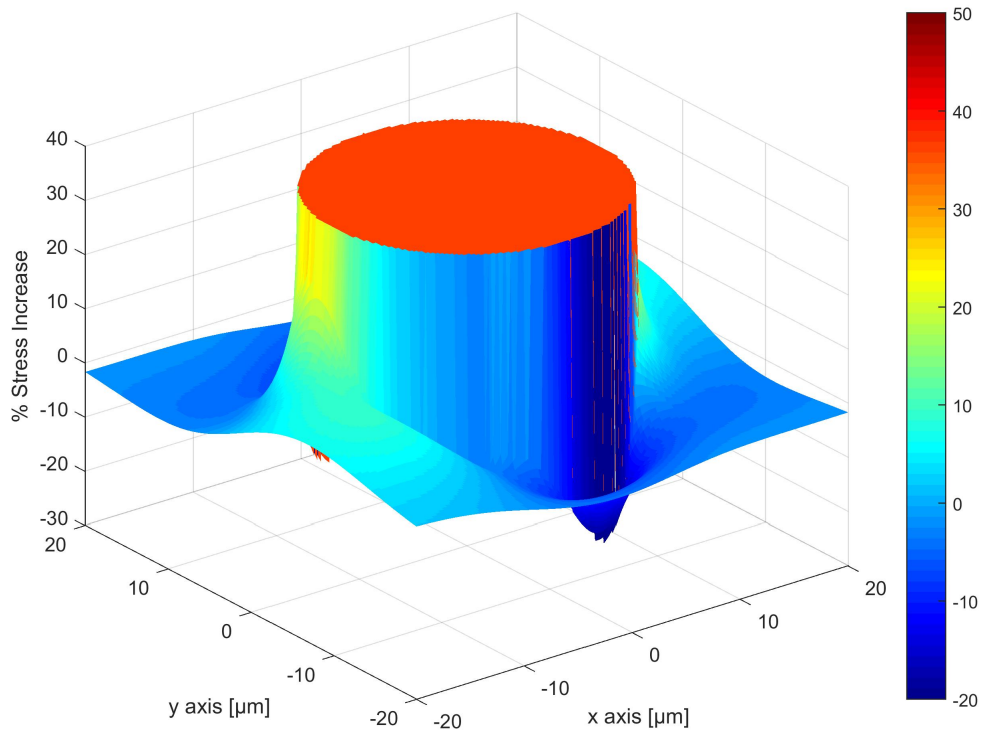


Figure 7.16: Test 4 - 21.0 h - Simulated stress inside and outside the inclusion

	Original	Maximum	Increase [%]
Tresca [MPa]	2748	3743	36
	Matrix	Inclusion	Ratio
Young Modulus [GPa]	210	375	1.79
Poisson Ratio	0.35	0.22	/
	x	y	z
Inclusion dimensions [μm]	12.50	12.50	12.50
Inclusion depth [μm]	-284		
Applied Load [N]	34400		
Cycles to failure [$\cdot 10^6$]	0.87		

Table 7.4: Test 4 - 21.0 h - Results

7.5 Case 5

The test $n^{\circ} 5$ presented a failed ball after **35.0 [h]**. The fractured area presented more than one inclusion, the chosen one was the most detrimental in terms of stress, as Case 1 and Case 2.

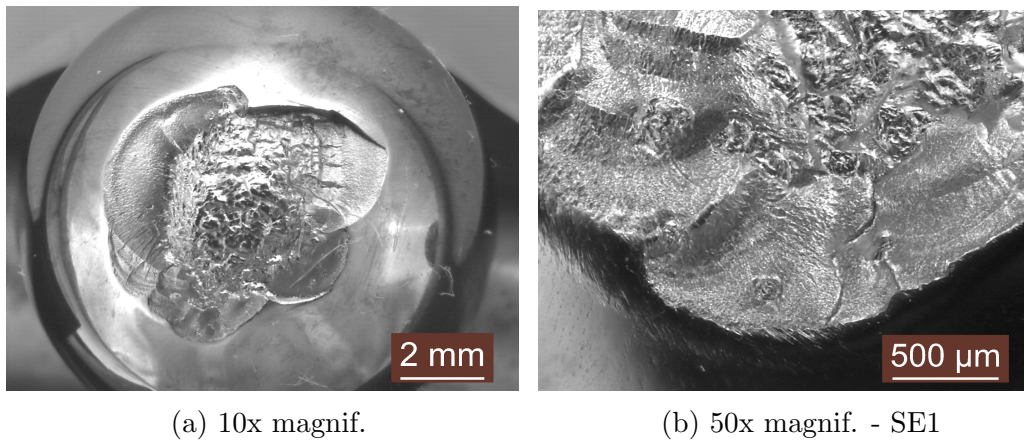


Figure 7.17: Test 5 - 35.0 h - Fracture inspection

The SEM analyses detected the inclusion dimensions and composition:

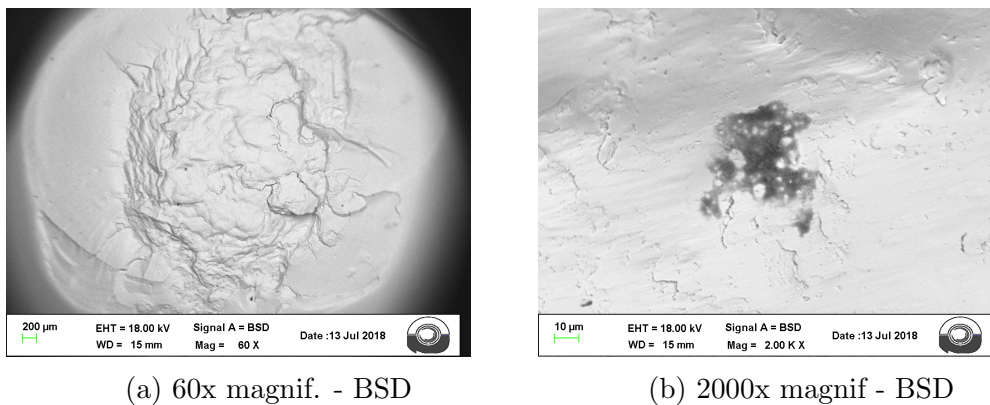


Figure 7.18: Test 5 - 35.0 h - SEM fracture inspection

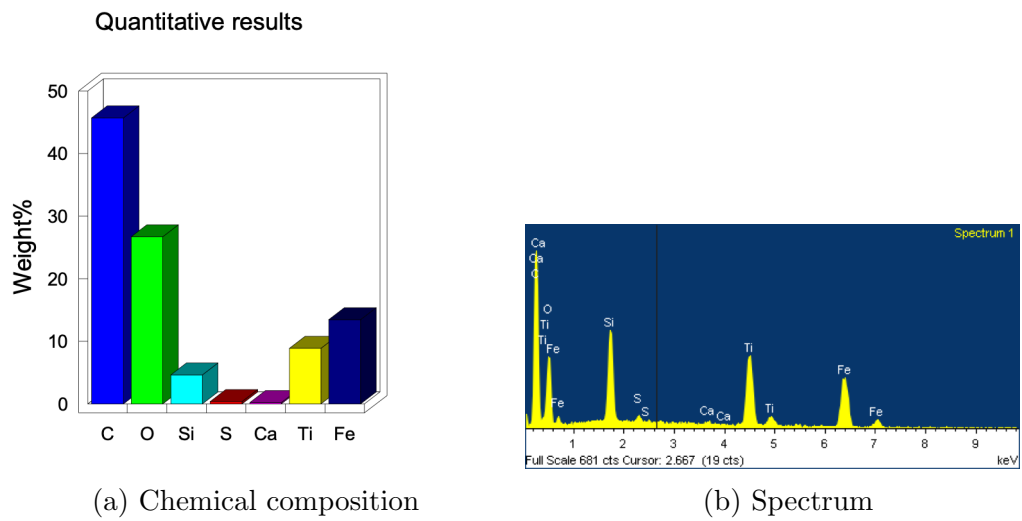


Figure 7.19: Test 5 - 35.0 h - SEM analyses

The inclusion is composed by Titanium carbides (TiC) and Silicon oxides (SiO_2). Since the presence of both is quite important, the Young modulus was computed with a weighted average of the two, looking the Spectrum obtained with the SEM analysis. This led to a stress increase that is reduced to 21%: considering the inclusion as TiC would have been too detrimental.

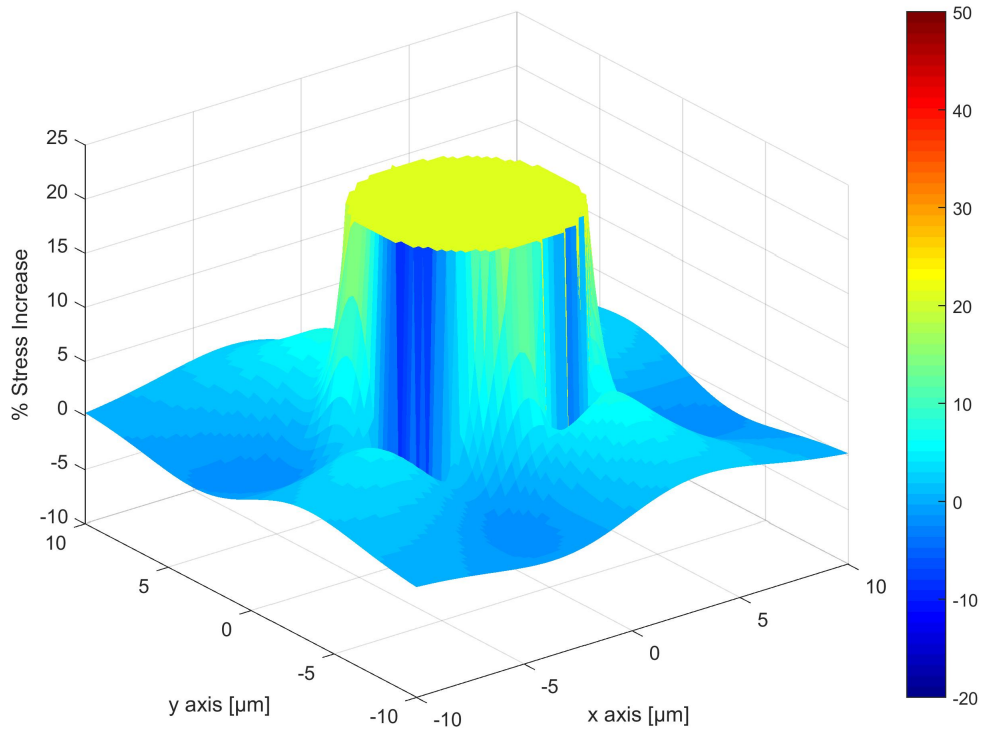


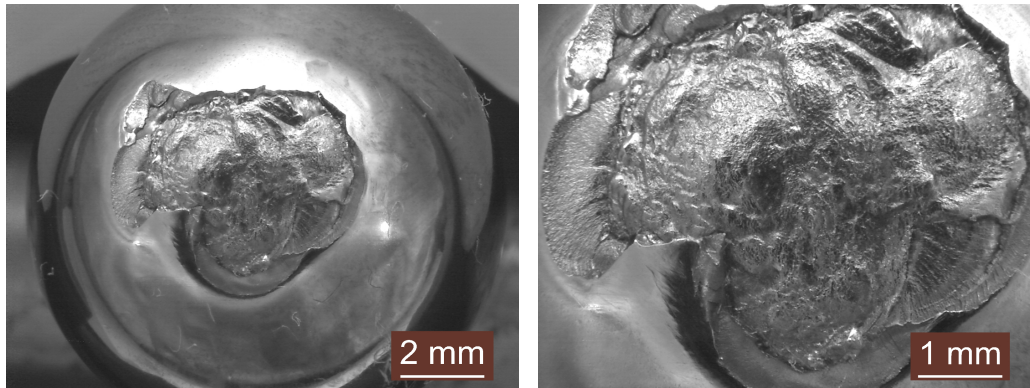
Figure 7.20: Test 5 - 35.0 h - Simulated stress inside and outside the inclusion

	Original	Maximum	Increase [%]
Tresca [MPa]	2609	3168	21
	Matrix	Inclusion	Ratio
Young Modulus [GPa]	210	280	1.33
Poisson Ratio	0.35	0.21	/
	x	y	z
Inclusion dimensions [μm]	4.50	4.50	4.50
Inclusion depth [μm]	-436		
Applied Load [N]	34400		
Cycles to failure [$\cdot 10^6$]	1.45		

Table 7.5: Test 5 - 35.0 h - Results

7.6 Case 6

The test $n^{\circ} 6$ presented a failed ball after **11.2 [h]**. The fractured area presented more than one inclusion.

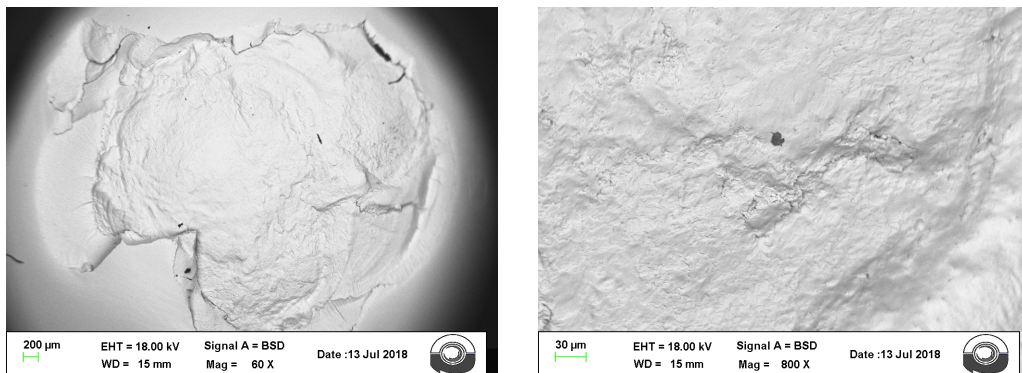


(a) 10x magnif.

(b) 20x magnif.

Figure 7.21: Test 6 - 11.2 h - Fracture inspection

The SEM analyses detected the inclusion dimensions and composition:



(a) 60x magnif. - BSD

(b) 800x magnif - BSD

Figure 7.22: Test 6 - 11.2 h - SEM fracture inspection

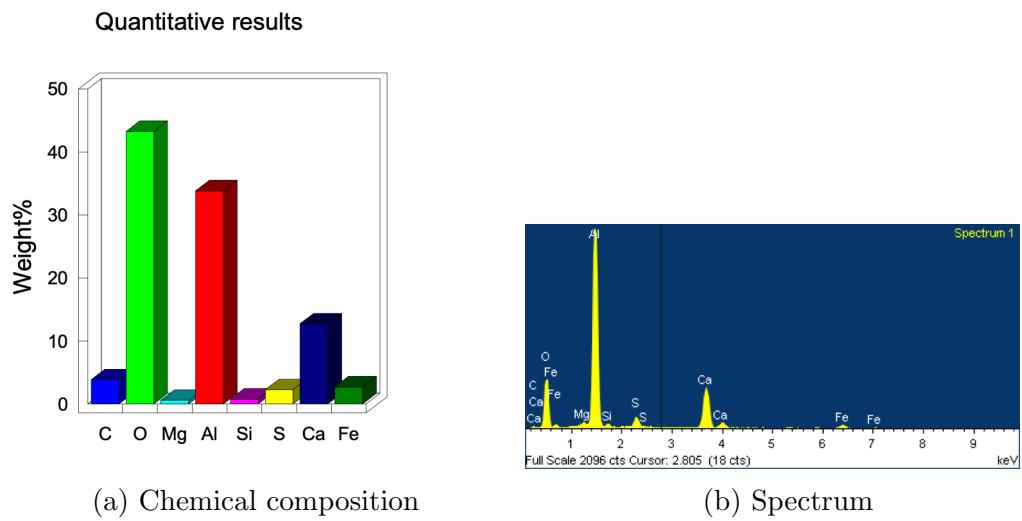


Figure 7.23: Test 6 - 11.2 h - SEM analyses

The inclusion composition is Allumina (Al_2O_3) with a minor presence of Calcium oxides.

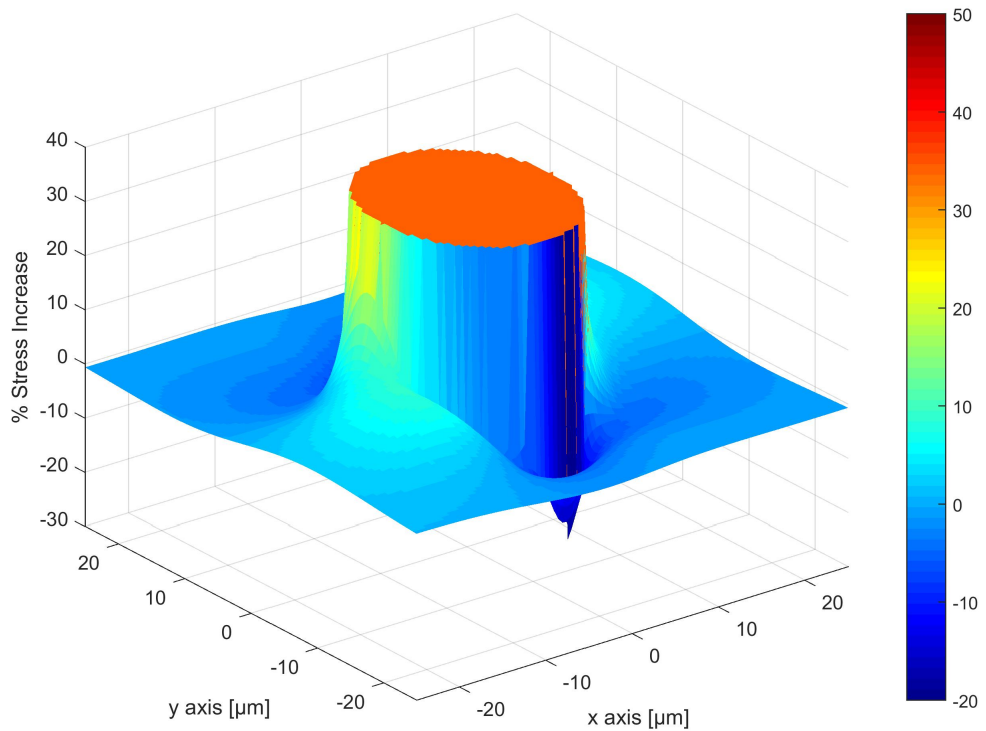


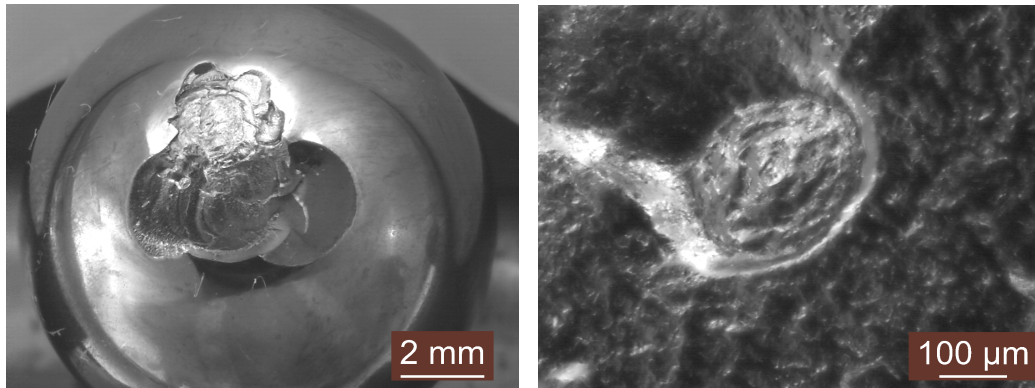
Figure 7.24: Test 6 - 11.2 h - Simulated stress inside and outside the inclusion

	Original	Maximum	Increase [%]
Tresca [MPa]	2759	3706	34
	Matrix	Inclusion	Ratio
Young Modulus [GPa]	210	375	1.79
Poisson Ratio	0.35	0.22	/
	x	y	z
Inclusion dimensions [μm]	12.34	10.00	10.00
Inclusion depth [μm]	-326		
Applied Load [N]	34400		
Cycles to failure [$\cdot 10^6$]	0.46		

Table 7.6: Test 6 - 11.2 h - Results

7.7 Case 7

The test $n^{\circ} 7$ presented a failed ball after **90.7 [h]**:

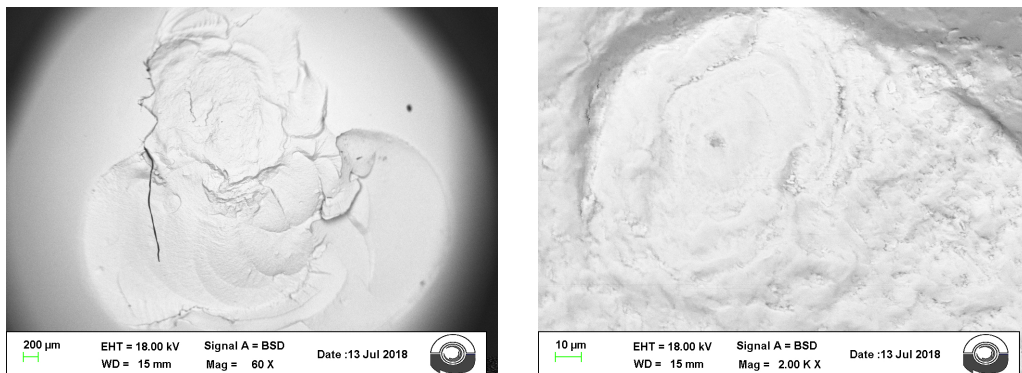


(a) 10x magnif.

(b) 160x magnif.

Figure 7.25: Test 7 - 90.7 h - Fracture inspection

The SEM analyses detected the inclusion dimensions and composition:



(a) 60x magnif. - BSD

(b) 2000x magnif - BSD

Figure 7.26: Test 7 - 90.7 h - SEM fracture inspection

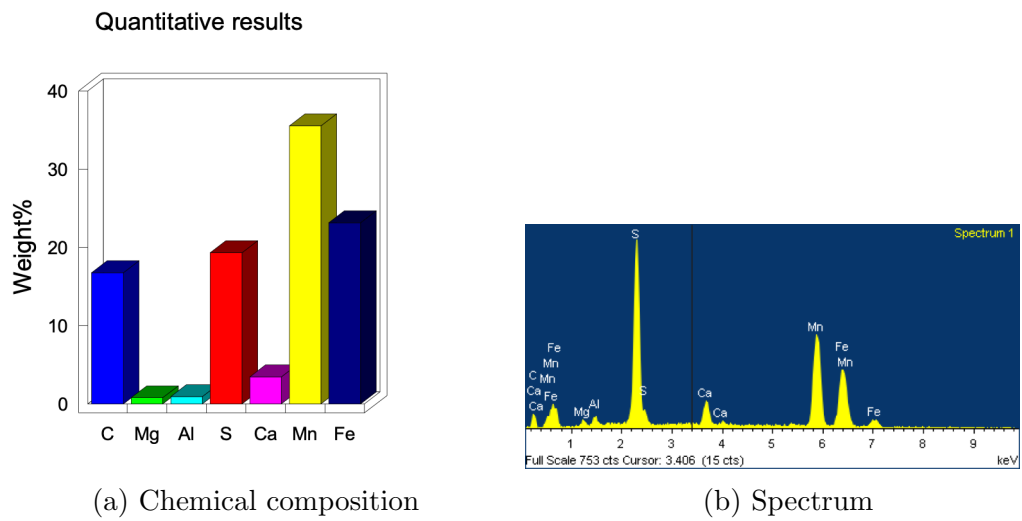


Figure 7.27: Test 7 - 90.7 h - SEM analyses

In the inclusion area were found S, Mn and Calcium. In this case it's tricky to find the correct Young Modulus since the composition it's not so clear. Nevertheless, this type of inclusion was not so critical (as Al_2O_3 or carbides and nitrides), in fact the test lasted way more than the others.

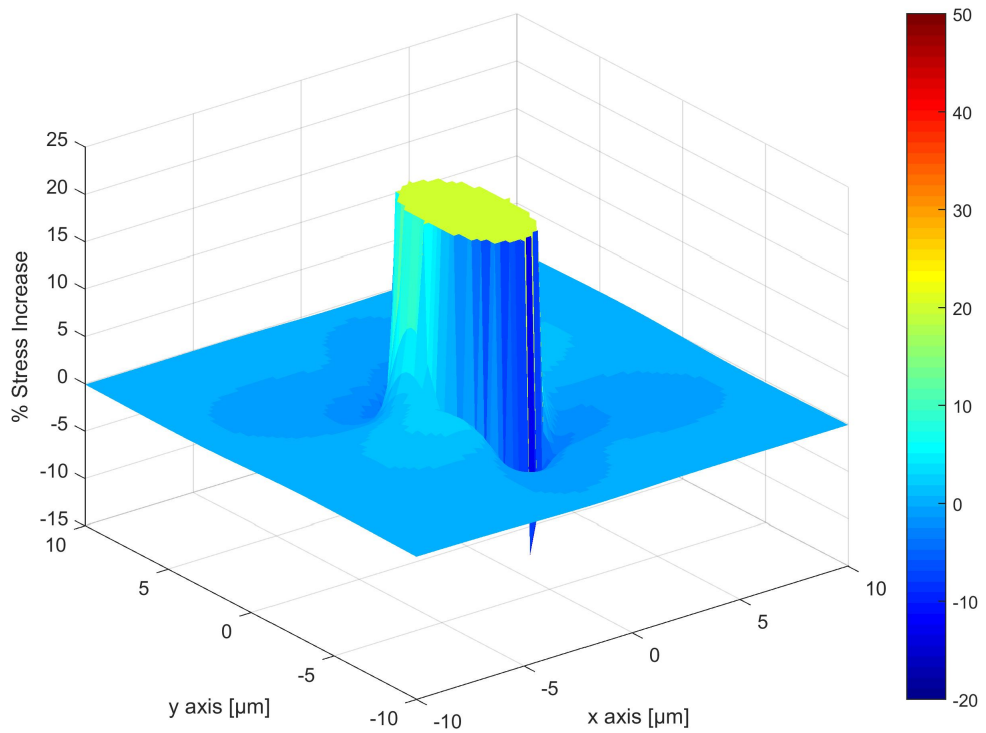


Figure 7.28: Test 7 - 90.7 h - Simulated stress inside and outside the inclusion

	Original	Maximum	Increase [%]
Tresca [MPa]	2636	3173	20
	Matrix	Inclusion	Ratio
Young Modulus [GPa]	210	289	1.38
Poisson Ratio	0.35	0.21	/
	x	y	z
Inclusion dimensions [μm]	3.50	2.00	2.00
Inclusion depth [μm]	-450		
Applied Load [N]	34400		
Cycles to failure [$\cdot 10^6$]	3.75		

Table 7.7: Test 7 - 90.7 h - Results

Chapter 8

Failures on specimens

Also for the specimens, **seven** cases were analyzed. The inclusion from which the fracture started, was composed by Al_2O_3 plus others oxides in **five** of the cases. Only in one specimen no *Aluminum* was found. The remaining specimen had an inclusion but probably it broke off when the rupture happened, so it was not possible to identify the inclusion composition.

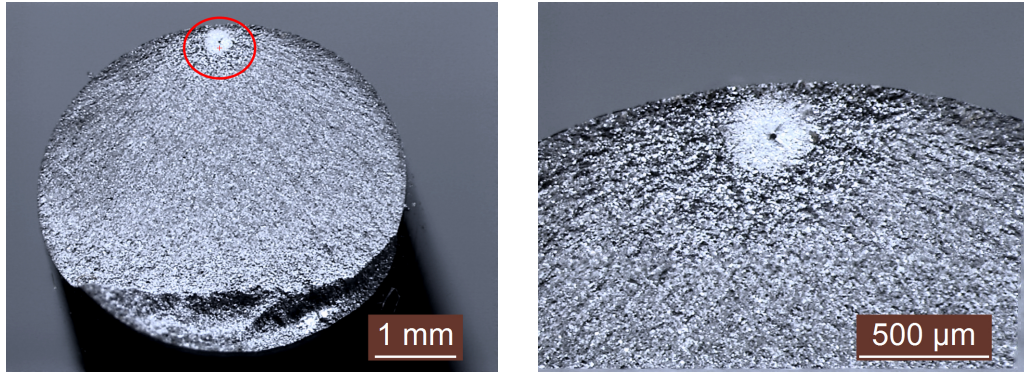
It has to be noticed that when Al_2O_3 was present, the Young modulus and the Poisson ratio were the ones of the Al_2O_3 itself, since they are the most critical in this case and it's very difficult to determine the factors taking into account every element.

The inclusions were all similar also in terms of dimensions and depth, and basically they can be approximated as circular.

Differently from the ball case, no more than one inclusion was present in the fractured area.

8.1 Case 1

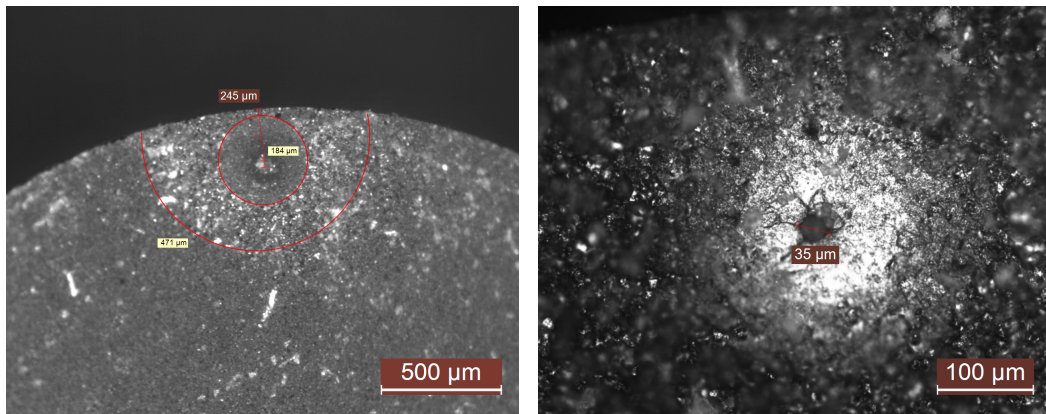
The specimen $n^{\circ} 1$ failed after $2.80 \cdot 10^6$ cycles:



(a) 20x magnif.

(b) 63x magnif.

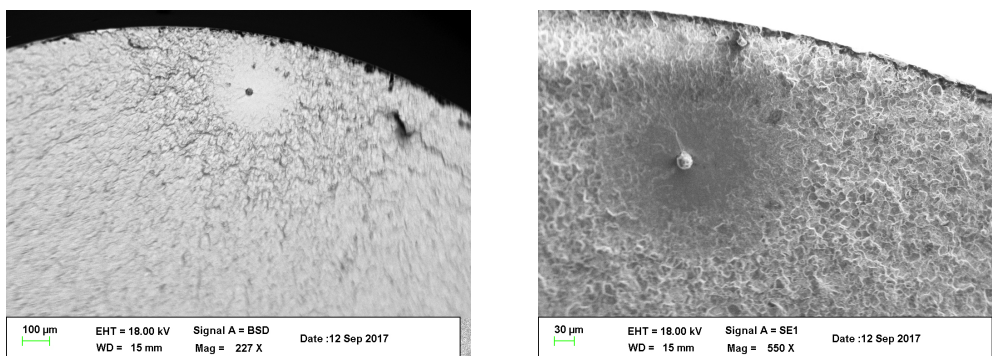
Figure 8.1: Specimen 1 - Fracture inspection



(a) Specimen 1 - 50x magnif.

(b) Specimen 1 - 200x magnif.

Figure 8.2: Specimen 1 - Inclusion dimensions



(a) Specimen 1 - 227x magnif.

(b) Specimen 1 - 550x magnif.

Figure 8.3: Specimen 1 - SEM fracture inspection

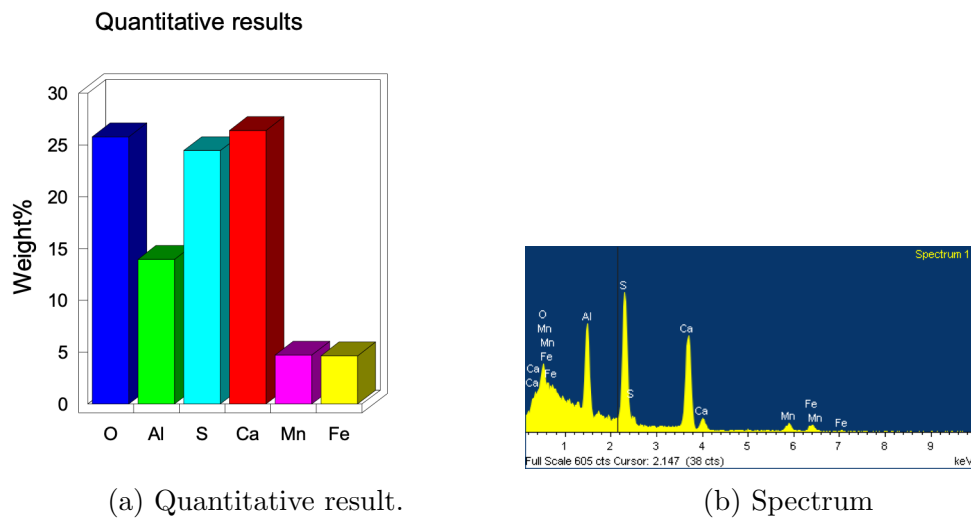


Figure 8.4: Specimen 1 - $2.8 \cdot 10^6$ cycles - SEM Analyses

The inclusion composition was not only Al_2O_3 , also Ca and S were present, inducing the possibility to have also these types of oxides. As explained before, it's difficult to find the elastic modulus of such a mixed inclusion, so the most critical one (Al_2O_3) was chosen.

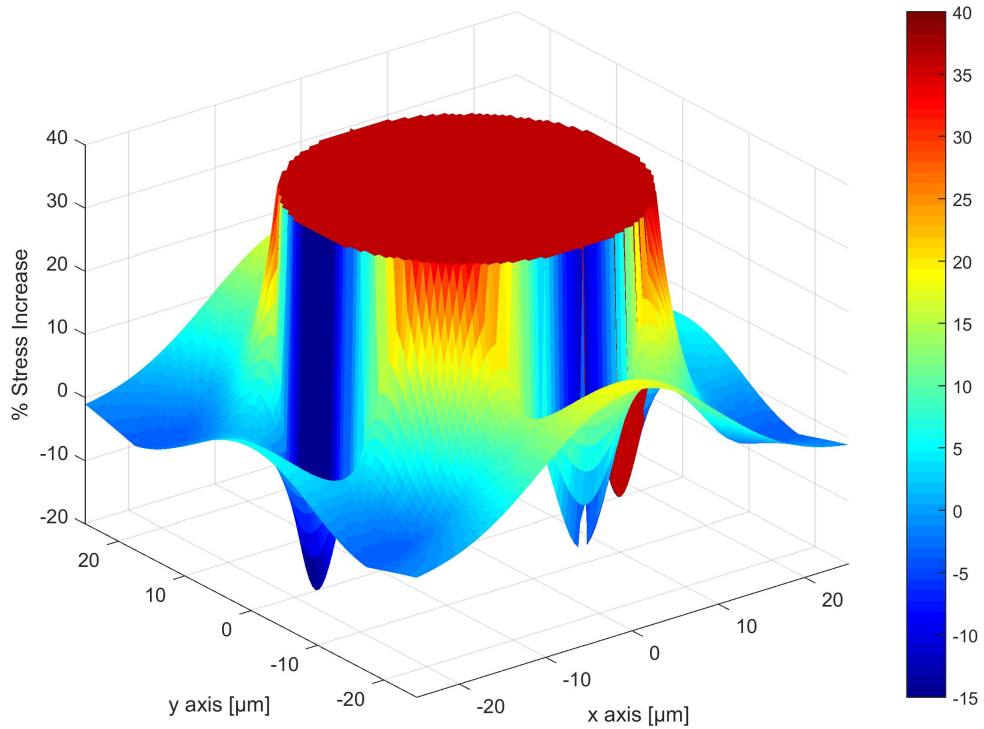


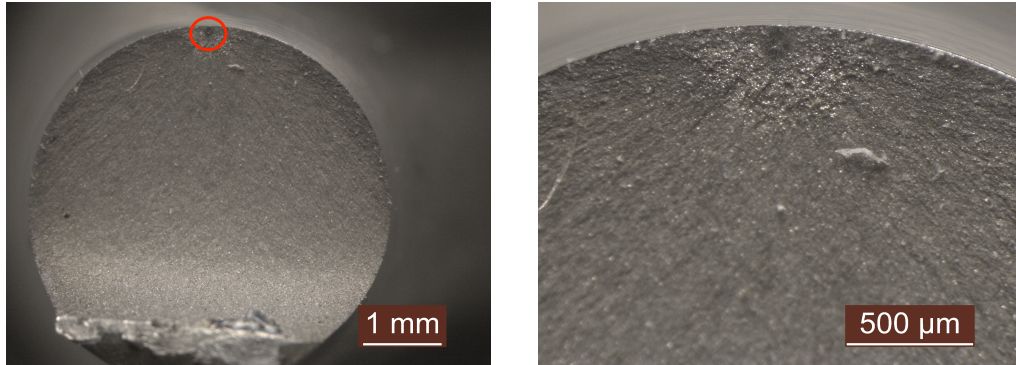
Figure 8.5: Specimen 1 - $2.80 \cdot 10^6$ cycles - Simulated stress inside and outside the inclusion

	Original	Maximum	Increase [%]
Tresca stress [MPa]	501	683	36
Original stress [MPa]	1125		
Stress at the depth [MPa]	1003	1366	36
	Matrix	Inclusion	Ratio
Young Modulus [GPa]	210	375	1.79
Poisson Ratio	0.35	0.22	/
	x	y	z
Inclusion dimensions [μm]	17.5	17.5	17.5
Inclusion depth [μm]	-245		
Cycles to failure [$\cdot 10^6$]	2.8		

Table 8.1: Specimen 1 - $2.80 \cdot 10^6$ cycles - Results

8.2 Case 2

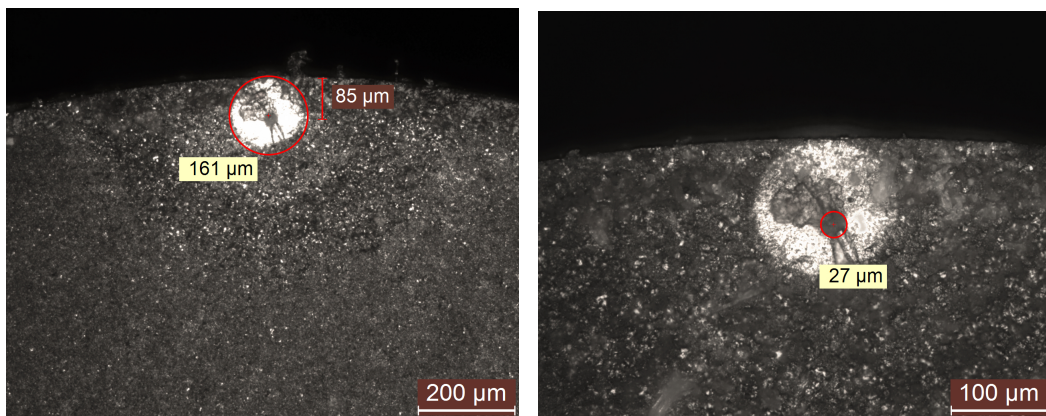
The specimen $n^{\circ} 2$ failed after $1.36 \cdot 10^6$ cycles:



(a) 20x magnif.

(b) 63x magnif.

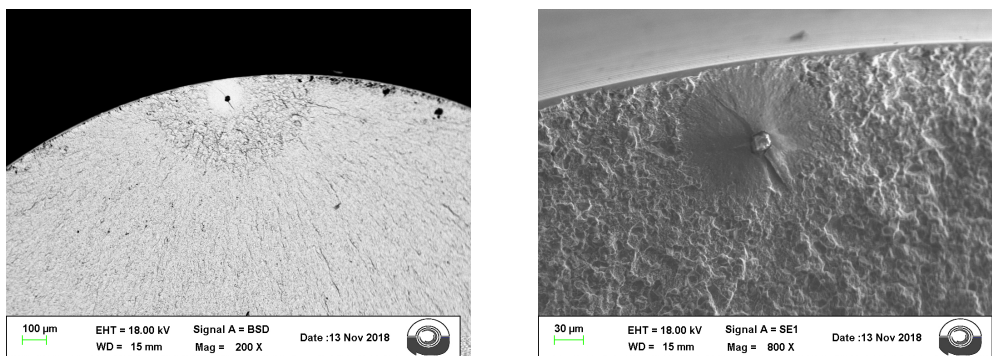
Figure 8.6: Specimen 2 - Fracture inspection



(a) Specimen 2 - 100x magnif.

(b) Specimen 2 - 200x magnif.

Figure 8.7: Specimen 2 - Inclusion dimensions



(a) Specimen 2 - 200x magnif.

(b) Specimen 2 - 800x magnif.

Figure 8.8: Specimen 2 - SEM fracture inspection

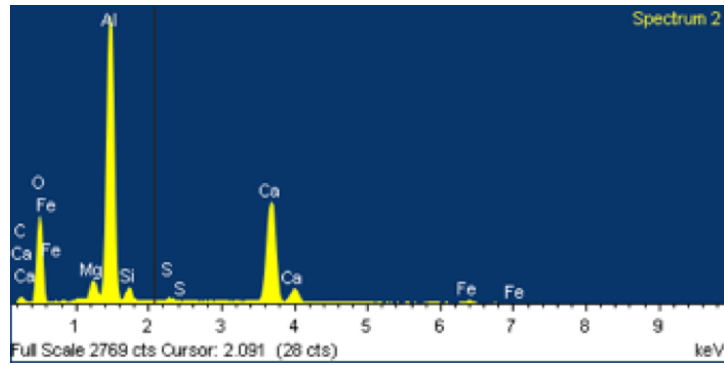


Figure 8.9: Specimen 2 - Spectrum

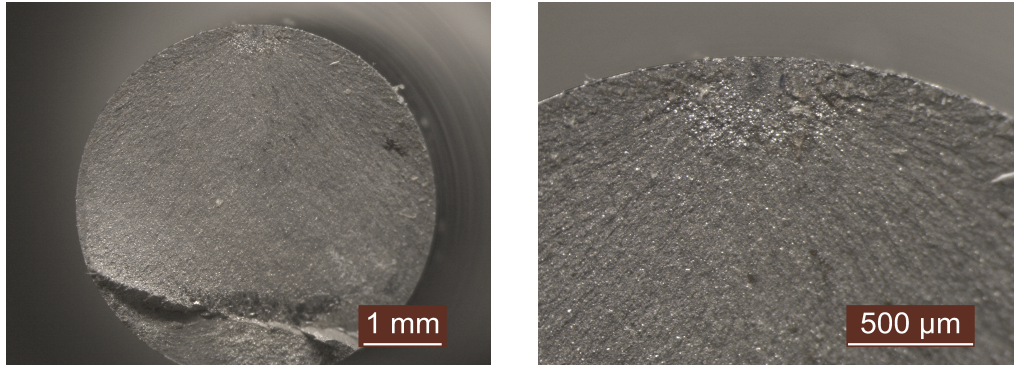
In this case the inclusion was a typical Al_2O_3 with circular shape.

	Original	Maximum	Increase [%]
Tresca stress [MPa]	577	787	36
Original stress [MPa]	1200		
Stress at the depth [MPa]	1155	1573	36
	Matrix	Inclusion	Ratio
Young Modulus [GPa]	210	375	1.79
Poisson Ratio	0.35	0.22	/
	x	y	z
Inclusion dimensions [μm]	13.5	13.5	13.5
Inclusion depth [μm]	-85		
Cycles to failure [$\cdot 10^6$]	1.36		

Table 8.2: Specimen 2 - $1.36 \cdot 10^6$ cycles - Results

8.3 Case 3

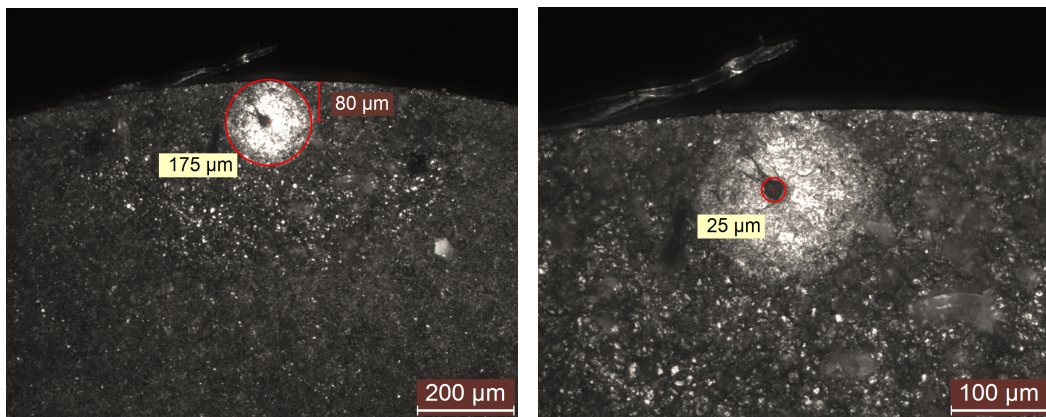
The specimen $n^{\circ} 3$ failed after $2.74 \cdot 10^6$ cycles:



(a) 20x magnif.

(b) 63x magnif.

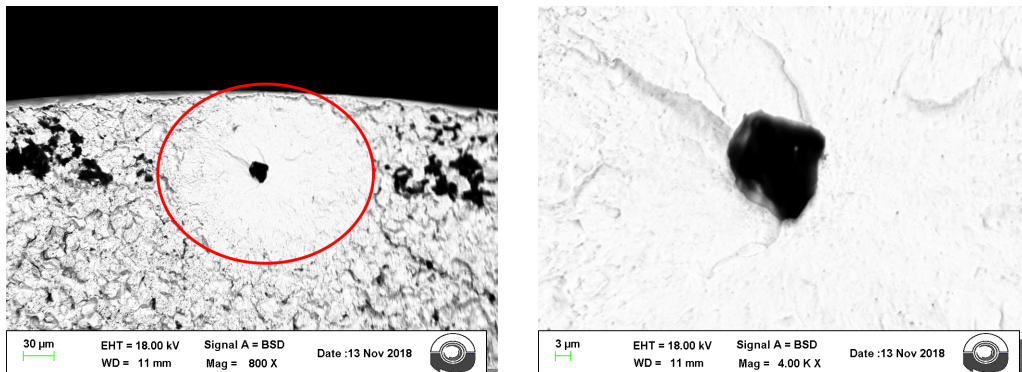
Figure 8.10: Specimen 3 - Fracture inspection



(a) Specimen 3 - 100x magnif.

(b) Specimen 3 - 200x magnif.

Figure 8.11: Specimen 3 - Inclusion dimensions



(a) Specimen 3 - 800x magnif. - BSD

(b) Specimen 3 - 4000x magnif.

Figure 8.12: Specimen 3 - SEM fracture inspection

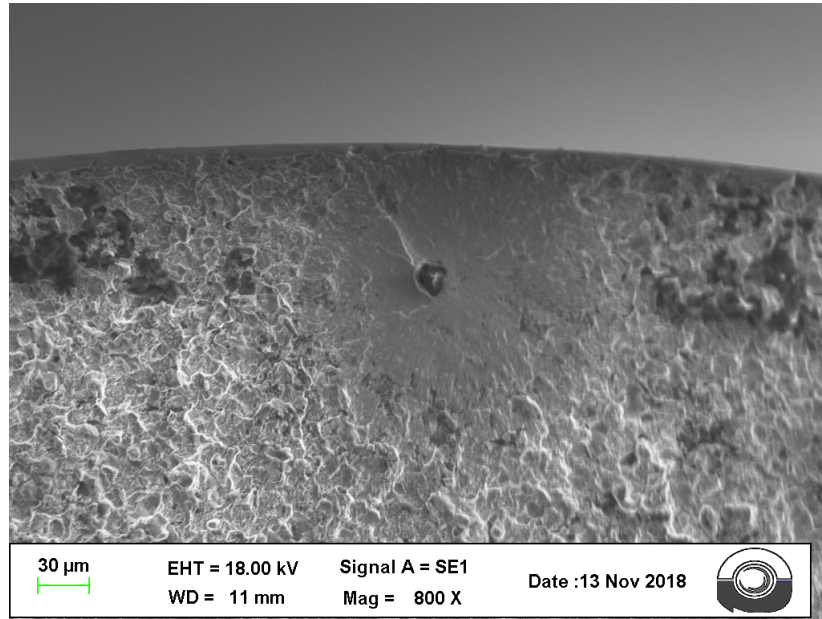


Figure 8.13: Specimen 3 - 800x magnif. - SE1

As the Fig. 8.12, 8.13 represent, the inclusion was not present in the inspected area. This can happen when the inclusion detaches from the surrounding material during the rupture of the specimen. No TiC or TiN inclusions (that are more critical than Al_2O_3) were found in all the tested specimens, so Al_2O_3 was assumed.

	Original	Maximum	Increase [%]
Tresca stress [MPa]	555	756	36
Original stress [MPa]	1200		
Stress at the depth [MPa]	1109	1511	36
	Matrix	Inclusion	Ratio
Young Modulus [GPa]	210	375	1.79
Poisson Ratio	0.35	0.22	/
	x	y	z
Inclusion dimensions [μm]	12.5	12.5	12.5
Inclusion depth [μm]	-80		
Cycles to failure [$\cdot 10^6$]	2.74		

Table 8.3: Specimen 3 - $1.36 \cdot 10^6$ cycles - Results

8.4 Case 4

The specimen $n^{\circ} 4$ failed after $4.83 \cdot 10^6$ cycles:

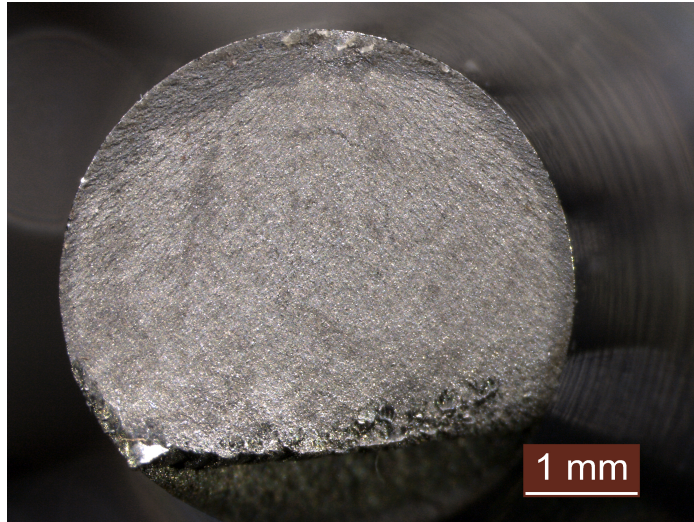
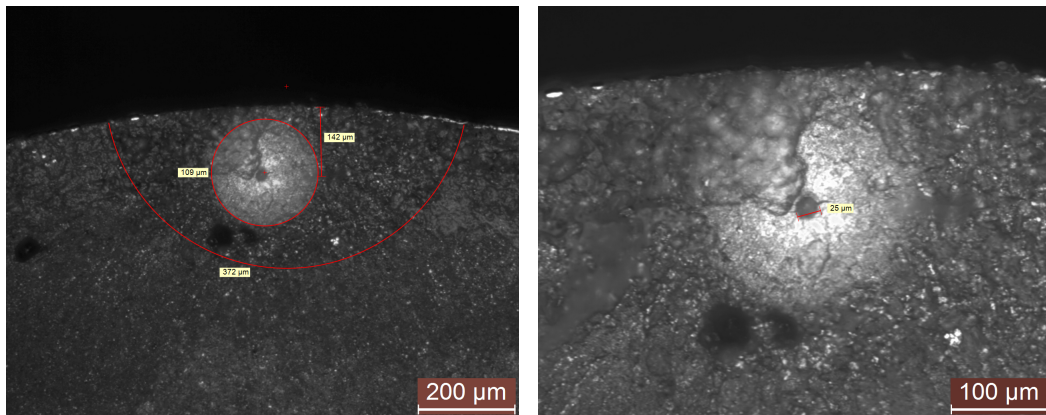


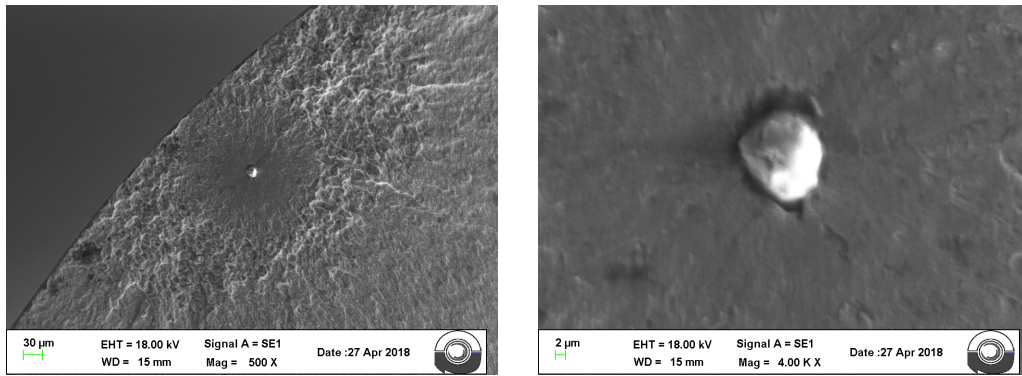
Figure 8.14: Specimen 4 - 20x magnif.



(a) Specimen 4 - 100x magnif.

(b) Specimen 4 - 200x magnif.

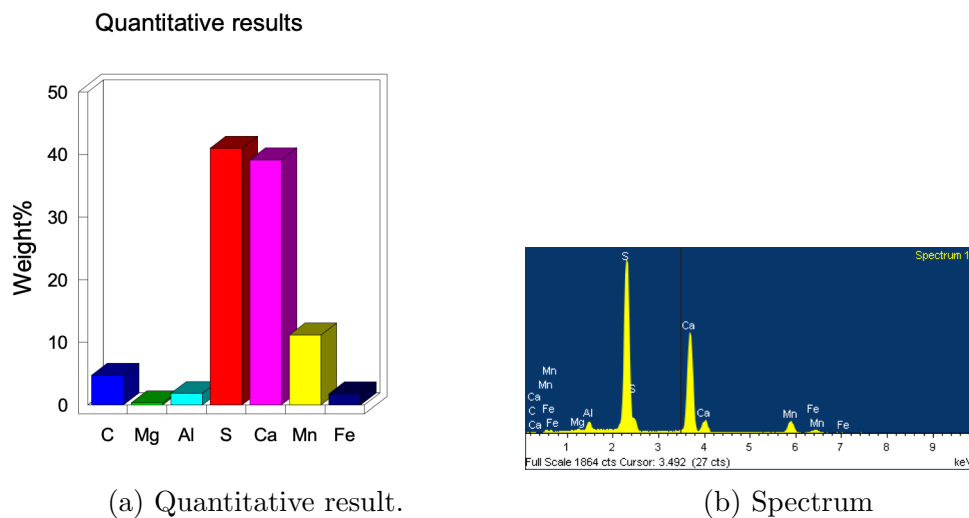
Figure 8.15: Specimen 4 - Inclusion dimensions



(a) Specimen 4 - 500x magnif.

(b) Specimen 4 - 4000x magnif.

Figure 8.16: Specimen 4 - SEM fracture inspection



(a) Quantitative result.

(b) Spectrum

Figure 8.17: Specimen 4 - $4.83 \cdot 10^6$ cycles - SEM Analyses

In this case the presence of *Aluminum* was quite low, while S, Ca and Mn were present in a relevant quantity. These types of element are not stiff as the oxides, in fact the stress increase was lower respect to the Al_2O_3 case (+21% vs +36%).

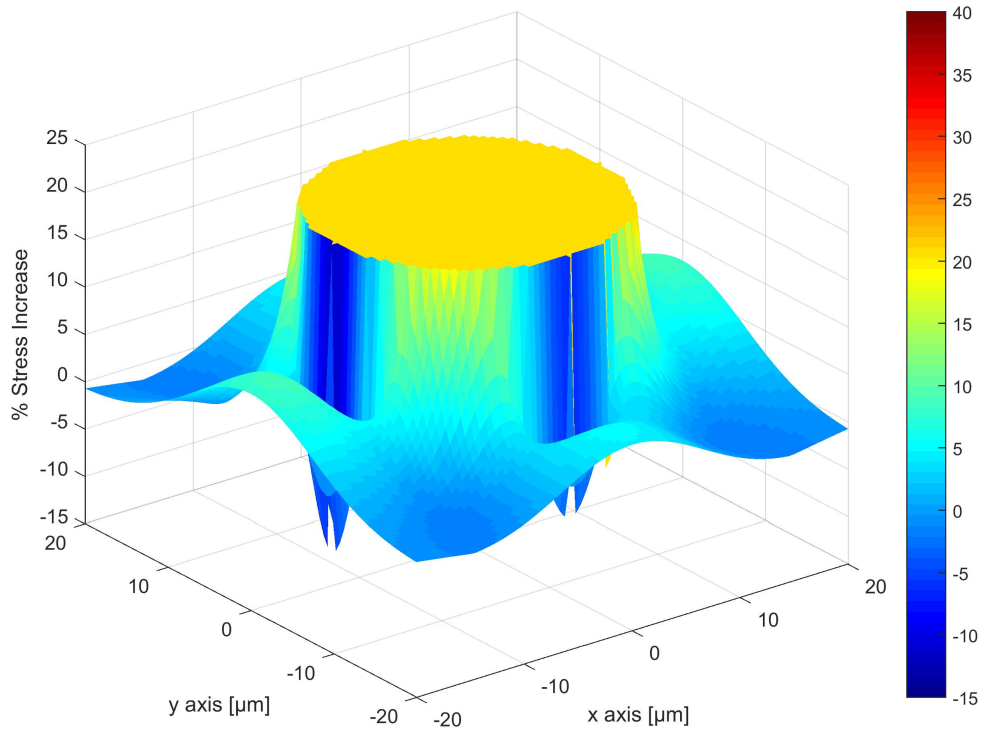


Figure 8.18: Specimen 4 - $4.83 \cdot 10^6$ cycles - Simulated stress inside and outside the inclusion

	Original	Maximum	Increase [%]
Tresca stress [MPa]	539	652	21
Original stress [MPa]	1150		
Stress at the depth [MPa]	1077	1304	21
	Matrix	Inclusion	Ratio
Young Modulus [GPa]	210	280	1.33
Poisson Ratio	0.35	0.22	/
	x	y	z
Inclusion dimensions [μm]	12.5	12.5	12.5
Inclusion depth [μm]	-142		
Cycles to failure [$\cdot 10^6$]	10.1		

Table 8.4: Specimen 4 - $4.83 \cdot 10^6$ cycles - Results

8.5 Case 5

The specimen $n^{\circ} 5$ failed after $1.60 \cdot 10^6$ cycles:

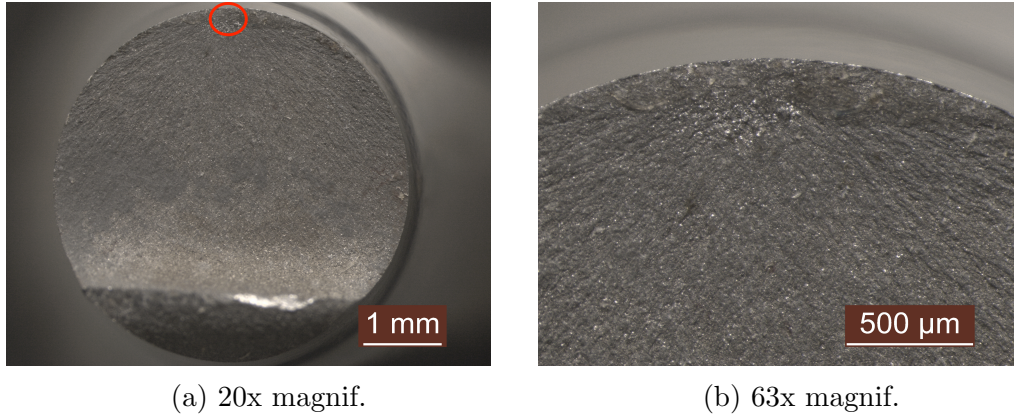


Figure 8.19: Specimen 5 - Fracture inspection

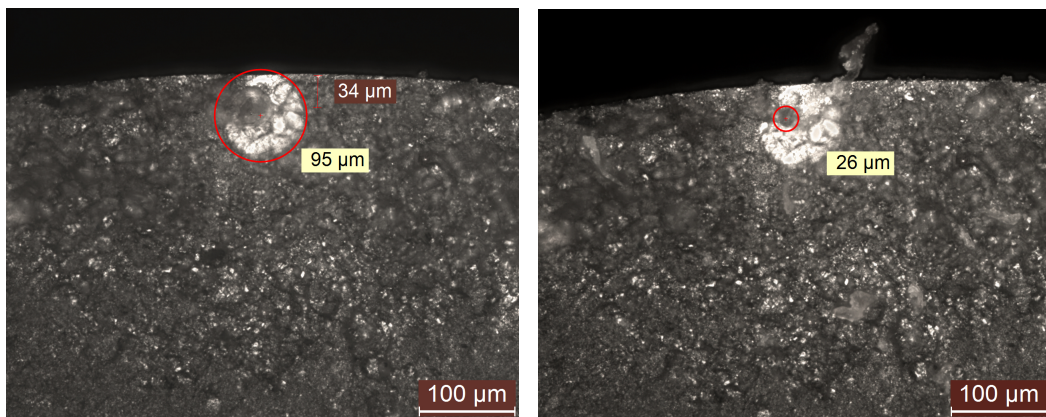


Figure 8.20: Specimen 5 - Inclusion dimensions - 200x magnif.

The SEM analyses detected the inclusion dimensions and composition:

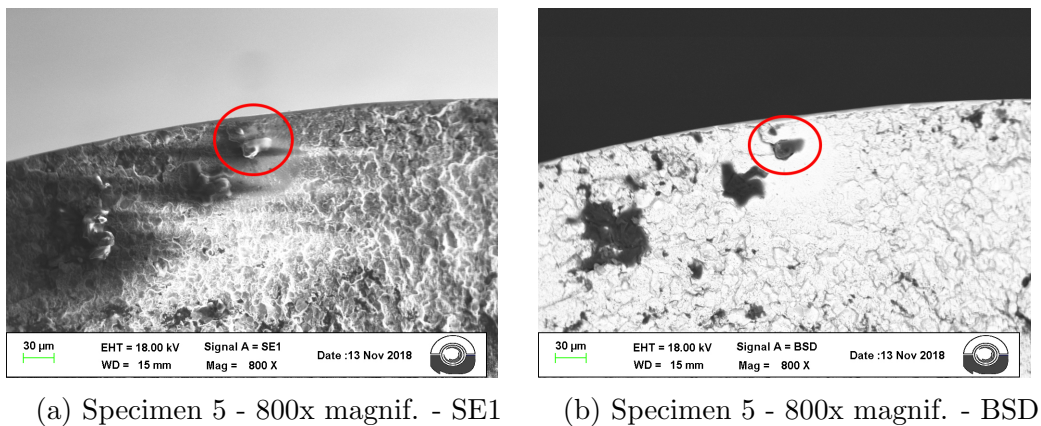


Figure 8.21: Specimen 5 - SEM fracture inspection

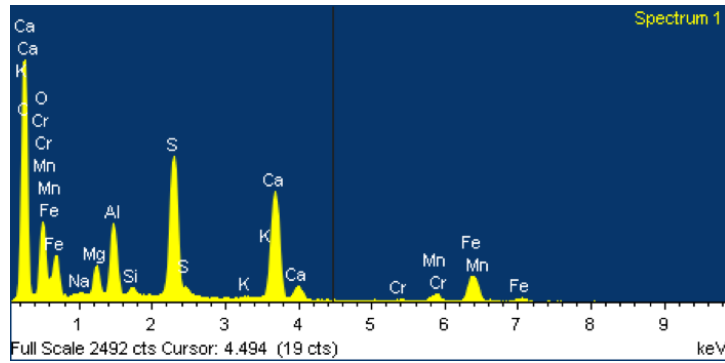


Figure 8.22: Specimen 5 - Spectrum

It happens sometimes that the first peak on the spectrum of a SEM analysis collects a great quantity of elements all together. A part from this peak (that was not considered), the composition it's similar to a typical Al_2O_3 type.

	Original	Maximum	Increase [%]
Tresca stress [MPa]	591	805	36
Original stress [MPa]	1200		
Stress at the depth [MPa]	1182	1610	36
	Matrix	Inclusion	Ratio
Young Modulus [GPa]	210	375	1.79
Poisson Ratio	0.35	0.22	/
	x	y	z
Inclusion dimensions [μm]	13.0	13.0	13.0
Inclusion depth [μm]	-34		
Cycles to failure [$\cdot 10^6$]	0.77		

Table 8.5: Specimen 5 - $0.77 \cdot 10^6$ cycles - Results

8.6 Case 6

The specimen $n^{\circ} 6$ failed after $0.62 \cdot 10^6$ cycles:

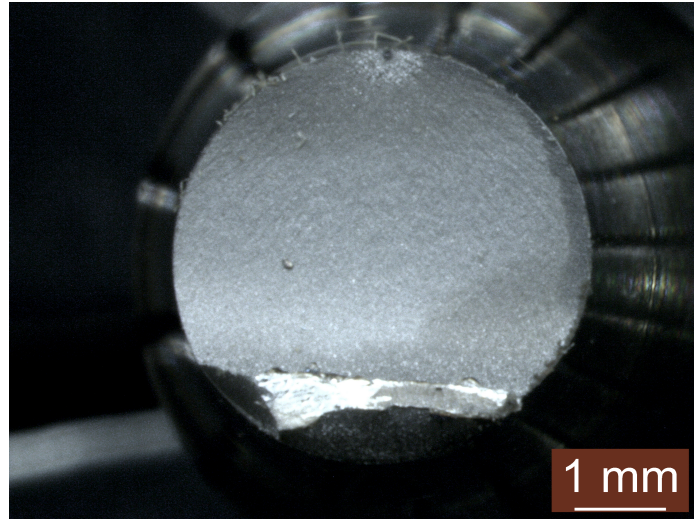
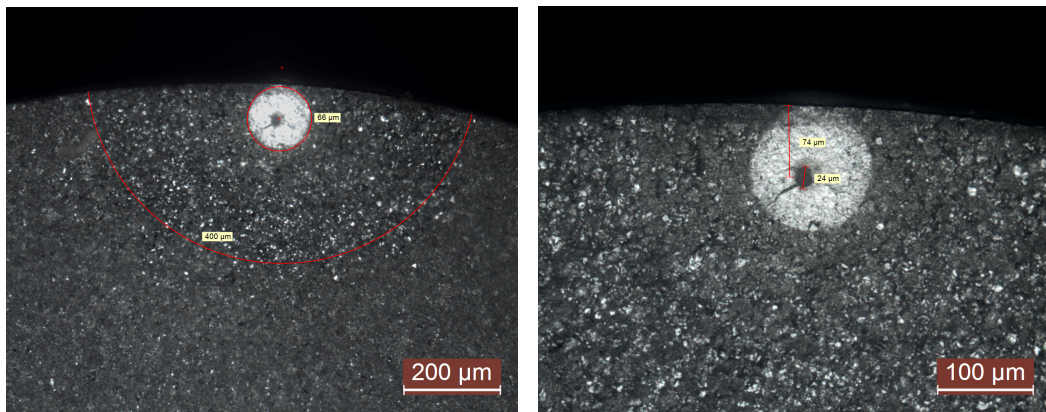


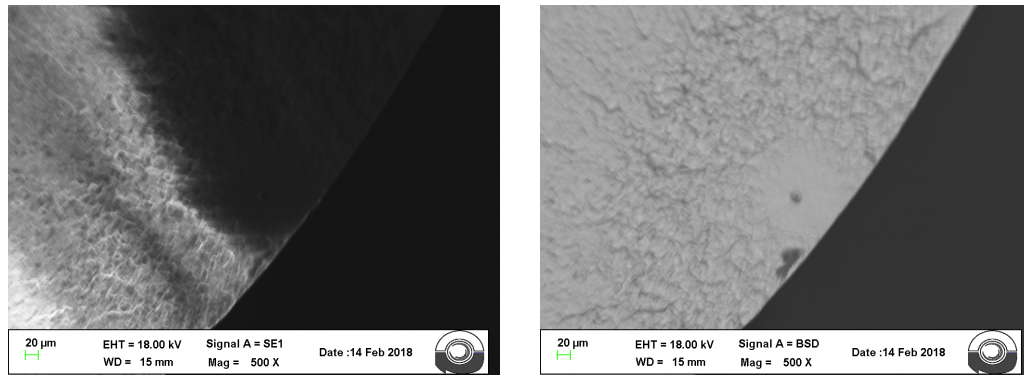
Figure 8.23: Specimen 6 - 16x magnif.



(a) Specimen 6 - 100x magnif.

(b) Specimen 6 - 200x magnif.

Figure 8.24: Specimen 6 - Inclusion dimensions



(a) Specimen 6 - 500x magnif.

(b) Specimen 6 - 4000x magnif.

Figure 8.25: Specimen 6 - SEM fracture inspection

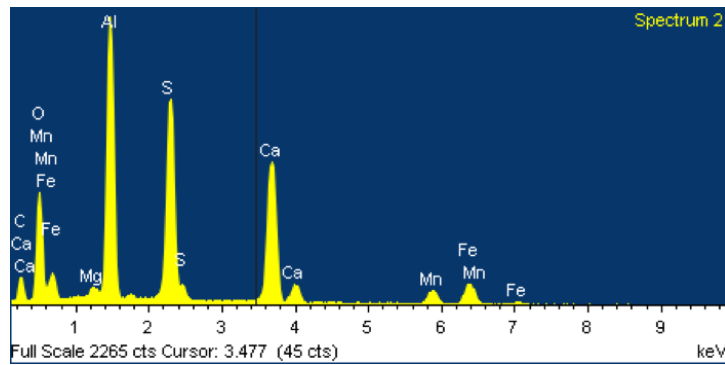


Figure 8.26: Specimen 6 - Spectrum

	Original	Maximum	Increase [%]
Tresca stress [MPa]	580	791	36
Original stress [MPa]	1200		
Stress at the depth [MPa]	1161	1581	36
	Matrix	Inclusion	Ratio
Young Modulus [GPa]	210	375	1.79
Poisson Ratio	0.35	0.22	/
	x	y	z
Inclusion dimensions [μm]	12.0	12.0	12.0
Inclusion depth [μm]	-74		
Cycles to failure [$\cdot 10^6$]	0.62		

Table 8.6: Specimen 6 - $0.62 \cdot 10^6$ cycles - Results

8.7 Case 7

The specimen $n^{\circ} 7$ failed after $0.06 \cdot 10^6$ cycles:

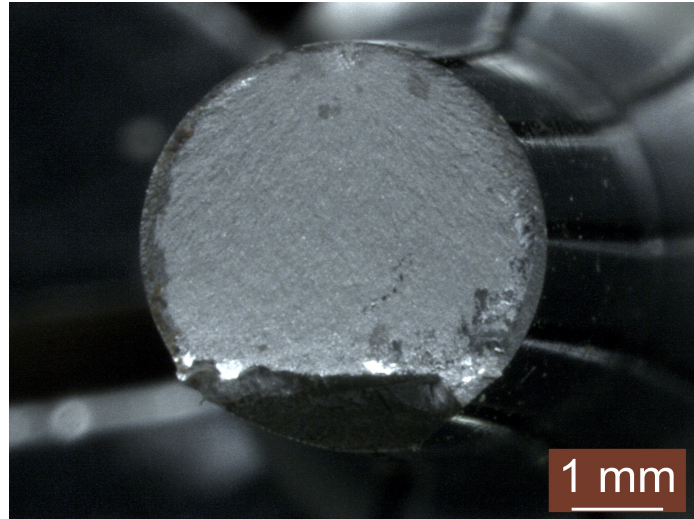
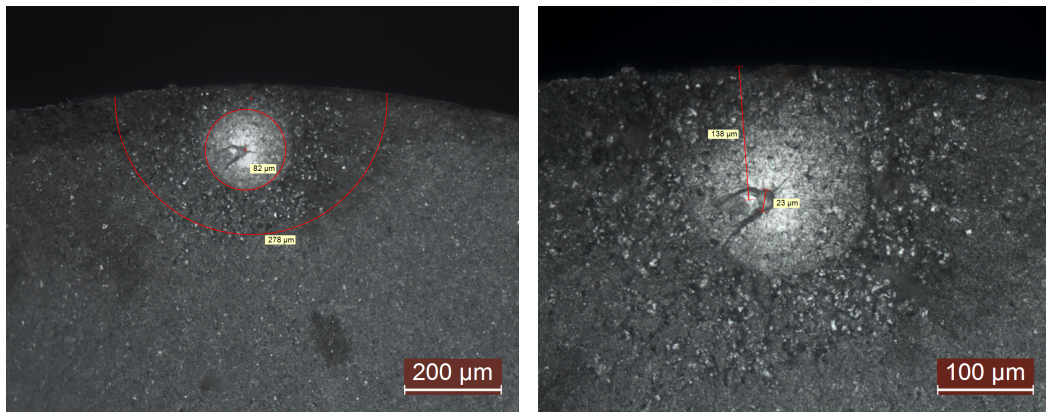


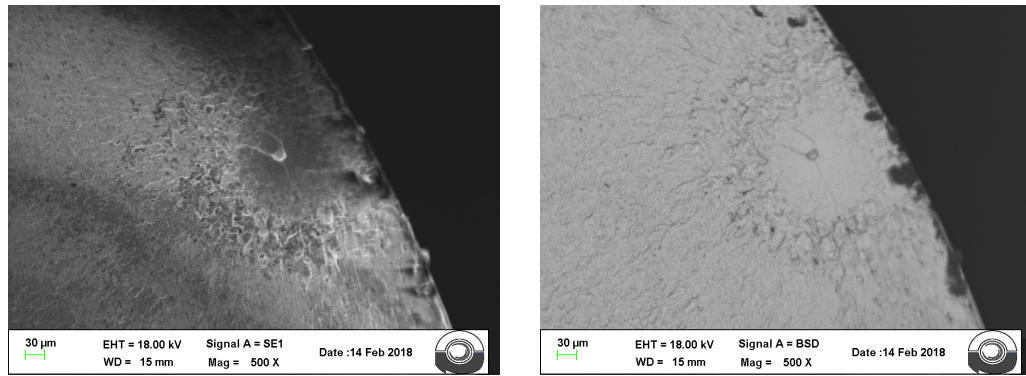
Figure 8.27: Specimen 7 - 16x magnif.



(a) Specimen 7 - 100x magnif.

(b) Specimen 7 - 200x magnif.

Figure 8.28: Specimen 7 - Inclusion dimensions



(a) Specimen 7 - 500x magnif.

(b) Specimen 7 - 500x magnif. - BSD

Figure 8.29: Specimen 7 - SEM fracture inspection

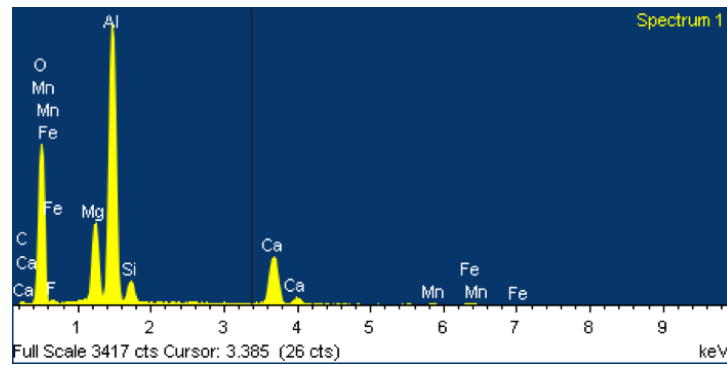


Figure 8.30: Specimen 7 - Spectrum

	Original	Maximum	Increase [%]
Tresca stress [MPa]	563	767	36
Original stress [MPa]	1200		
Stress at the depth [MPa]	1126	1531	36
	Matrix	Inclusion	Ratio
Young Modulus [GPa]	210	375	1.79
Poisson Ratio	0.35	0.22	/
	x	y	z
Inclusion dimensions [μm]	11.5	11.5	11.5
Inclusion depth [μm]	-138		
Cycles to failure [$\cdot 10^6$]	0.06		

Table 8.7: Specimen 7 - $0.06 \cdot 10^6$ cycles - Results

Chapter 9

Life - Stress Relation

Considering the Tresca stress value (modified by the inclusion presence), of the **seven** balls and **seven** specimens, two respective diagrams were made (Fig. 9.1, 9.2).

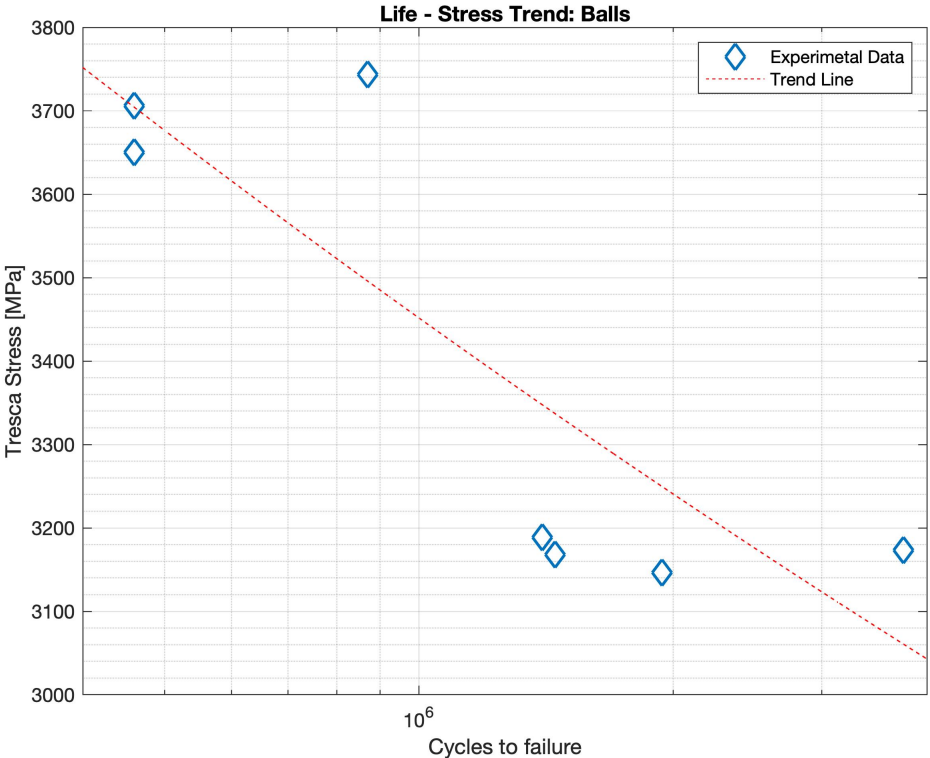


Figure 9.1: Life - Stress trend for balls



Figure 9.2: Life - Stress trend for specimens

In both cases it is possible to note that when the stress increases, the cycles to failure decreases.

The trend line for the ball cases resulted as:

$$\tau_{tresca} = 12135 \cdot N^{-0.091} \tag{9.1}$$

with $R^2 = 0.7095$.

The trend line for the specimens:

$$\tau_{tresca} = 1022 \cdot N^{-0.023} \tag{9.2}$$

with $R^2 = 0.1693$.

The low value of R^2 for the specimen cases is probably due to the severe nature of tension-compression at which the specimens are subjected. Another important factor is the probability to have, in some cases, surface defects that can reduce the fatigue life.

9.1 Stress threshold

9.1.1 Spheres

The maximum stress increase found in the experimental cases was **+43%** (case **1**). As already stated in chapter 6, it is reasonable to consider **+50%** as a limit value:

$$\tau_{threshold} = \frac{\tau_{TrescaMax}}{1.5}$$

In order to have a 'real Tresca' that overcomes the 'maximum ideal Tresca', the inclusion should not be located at a distance from the surface that is more than **188%** the contact half width (chapter 6). The graph below (9.3) shows the proof that the critical inclusions found on failed balls are not shallower than this value.

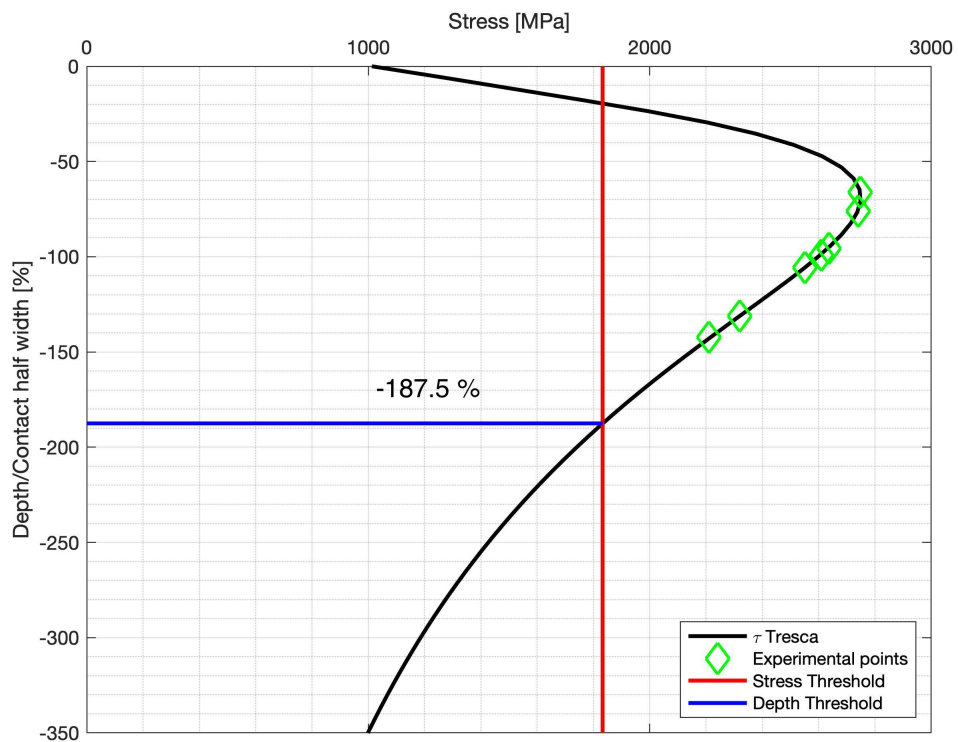


Figure 9.3: Stress Threshold - Experimental Cases

Chapter 10

Conclusions

The main target of the thesis was to evaluate the influence of microinclusions on the fatigue life of rolling bodies. For this reason, the effect on the stress field of balls and specimens made of 100Cr6 was studied.

The spheres were tested thanks to Test Rigs, while a Rotating bending fatigue machine was used for specimens. The fracture analyses were assessed thanks to a gaugemeter, an optical microscope and a Scanning Electron Microscope. A numerical solver that implements the Eshelby solution for the inclusion problem was developed to analyze the cases above. Some simulations were made to understand the functionalities of the code and the effect of the different parameters: dimension, shape, depth, chemical composition and configuration were evaluated. Moreover, the code was useful to simulate the stress state of the experimental cases.

Seven specimens and seven balls were considered, for each case all the inclusion properties were found and the stress state mesh was evaluated.

The survey pointed out that inclusions that are shallower than a certain value are not critical for failures. The difference between the Young modulus of the inclusion and the one of the matrix, as the Poisson ratio, is very important for the distribution of stress variation. If the difference is notable, the stress peak will be prominent. Another key factor is the shape, if the inclusion can be approximated as an elongated ellipse, the stress peak increment is greater. There was a wide range of inclusion types found in balls, with also different shapes and dimensions, while in specimens they had similar properties.

Chapter 11

Future works

Nowadays, the steel balls for bearing applications are more and more able to perform at a very high level from the fatigue life point of view. One of the most critical parameters that affect the performances is the inclusion presence. For this reason it's necessary to extend the present study with a life model that is able to predict the fatigue life of the rolling element considering the inclusion presence.

From the stress computation point of view, a better characterization of the inclusions Young modulus and Poisson ratio is mandatory. Also the effect of residual stresses should be analyzed in depth. When the stress evaluation will be complete, the life model should take into account the spinning of the ball inside the bearing, so how many actual stress cycles the inclusion suffers.

Ringraziamenti

Innanzitutto vorrei ringraziare la Prof. Raffaella Sesana per aver creduto in me, rendendo possibile lo svolgimento di questi tesi e per il costante supporto lungo tutta la durata del periodo di tirocinio e tesi che ho intrapreso in azienda. Vorrei anche esprimere la mia gratitudine a Sebastiano Rizzo, che mi ha accolto nel Laboratorio Centrale di Tsubaki - Nakashima, dandomi l'opportunità di vivere una soddisfacente esperienza aziendale per otto mesi. Aggiungo anche il Product Development team per il supporto garantitomi ogni giorno: Andrea Uva, Stefano Pagliassotto, Cosimo Sammarco, Alberto Carano e tutti i membri del reparto Qualità di Pinerolo.

Un ringraziamento speciale va ai miei genitori, Mariangela e Raffaele, a cui sono profondamente legato ed eternamente grato per tutto quello che hanno fatto e continuano a fare per me. Tengo anche a ringraziare mio zio e i miei nonni per avermi sempre ascoltato e sostenuto durante tutto il percorso didattico. Infine, vorrei ringraziare Giulia, che ormai da molti anni condivide con me tutti i momenti positivi e negativi, senza mai farmi mancare il suo affetto ed il suo sostegno.

List of Figures

2.1	Interference fringes of two transparent bodies in contact, loaded	17
2.2	Subsurface stresses: sphere-sphere contact	19
2.3	Subsurface stresses: cylinder-cylinder contact	19
4.1	Raw steel coil cut and final specimen	24
4.2	Specimen geometry	25
4.3	Rotating bending machine	26
4.4	Test rigs for balls bearing tests	28
4.5	Gauge meter	31
4.6	Scanning Electron Microscope	32
4.7	Sub-surface stresses, corresponding to 34400 N	34
4.8	Sub-surface Tresca Stress, corresponding to 34400 N	35
4.9	Rotating bending machine - Load condition	36
4.10	Free body diagram	36
6.1	Sub-surface stresses, axial load equal to 34400 N	45
6.2	Stress perturbation due to a spheroidal inclusion - 0.5 μm radius	46
6.3	Stress perturbation due to a spheroidal inclusion - 50 μm radius	46
6.4	Stress perturbation: effect of the shape - 1st Case	47
6.5	Stress perturbation: effect of the shape - 2nd Case	48
6.6	Stress perturbation: effect of the shape - 3rd Case	48
6.7	Stress perturbation: effect of the depth	50
6.8	Depth threshold	52
7.1	Test 1 - 11.2 h - Fracture inspection	54
7.2	Test 1 - 11.2 h - 2000x magnif.	54
7.3	Test 1 - 11.2 h - SEM analyses	55
7.4	Test 1 - 11.2 h - Simulated stress inside and outside the inclusion	55
7.5	Test 2 - 33.9 h - Fracture inspection	57
7.6	Test 2 - 33.9 h - 2000x magnif.	57

7.7	Test 2 - 33.9 h - SEM analyses	58
7.8	Test 2 - 33.9 h - Simulated stress inside and outside the inclusion	58
7.9	Test 3 - 46.9 h - Fracture inspection	60
7.10	Test 3 - 46.9 h - SEM fracture inspection	60
7.11	Test 3 - 46.9 h - SEM analyses	61
7.12	Test 3 - 46.9 h - Simulated stress inside and outside the inclusion	61
7.13	Test 4 - 21.0 h - Fracture inspection	63
7.14	Test 4 - 21.0 h - SEM fracture inspection	63
7.15	Test 4 - 21.0 h - SEM analyses	64
7.16	Test 4 - 21.0 h - Simulated stress inside and outside the inclusion	64
7.17	Test 5 - 35.0 h - Fracture inspection	66
7.18	Test 5 - 35.0 h - SEM fracture inspection	66
7.19	Test 5 - 35.0 h - SEM analyses	67
7.20	Test 5 - 35.0 h - Simulated stress inside and outside the inclusion	68
7.21	Test 6 - 11.2 h - Fracture inspection	69
7.22	Test 6 - 11.2 h - SEM fracture inspection	69
7.23	Test 6 - 11.2 h - SEM analyses	70
7.24	Test 6 - 11.2 h - Simulated stress inside and outside the inclusion	70
7.25	Test 7 - 90.7 h - Fracture inspection	72
7.26	Test 7 - 90.7 h - SEM fracture inspection	72
7.27	Test 7 - 90.7 h - SEM analyses	73
7.28	Test 7 - 90.7 h - Simulated stress inside and outside the inclusion	73
8.1	Specimen 1 - Fracture inspection	76
8.2	Specimen 1 - Inclusion dimensions	76
8.3	Specimen 1 - SEM fracture inspection	76
8.4	Specimen 1 - $2.8 \cdot 10^6$ cycles - SEM Analyses	77
8.5	Specimen 1 - $2.80 \cdot 10^6$ cycles - Simulated stress inside and outside the inclusion	78
8.6	Specimen 2 - Fracture inspection	79
8.7	Specimen 2 - Inclusion dimensions	79
8.8	Specimen 2 - SEM fracture inspection	79
8.9	Specimen 2 - Spectrum	80
8.10	Specimen 3 - Fracture inspection	81
8.11	Specimen 3 - Inclusion dimensions	81
8.12	Specimen 3 - SEM fracture inspection	81
8.13	Specimen 3 - 800x magnif. - SE1	82
8.14	Specimen 4 - 20x magnif.	83

8.15 Specimen 4 - Inclusion dimensions	83
8.16 Specimen 4 - SEM fracture inspection	84
8.17 Specimen 4 - $4.83 \cdot 10^6$ cycles - SEM Analyses	84
8.18 Specimen 4 - $4.83 \cdot 10^6$ cycles - Simulated stress inside and outside the inclusion	85
8.19 Specimen 5 - Fracture inspection	86
8.20 Specimen 5 - Inclusion dimensions - 200x magnif.	86
8.21 Specimen 5 - SEM fracture inspection	86
8.22 Specimen 5 - Spectrum	87
8.23 Specimen 6 - 16x magnif.	88
8.24 Specimen 6 - Inclusion dimensions	88
8.25 Specimen 6 - SEM fracture inspection	89
8.26 Specimen 6 - Spectrum	89
8.27 Specimen 7 - 16x magnif.	90
8.28 Specimen 7 - Inclusion dimensions	90
8.29 Specimen 7 - SEM fracture inspection	91
8.30 Specimen 7 - Spectrum	91
9.1 Life - Stress trend for balls	92
9.2 Life - Stress trend for specimens	93
9.3 Stress Threshold - Experimental Cases	94
A.1 Test 1 - $2^{nd}incl.$ - 2000x magnif. and stress	103
A.2 Test 1 - $2^{nd}incl.$ - SEM analyses	104
A.3 Test 1 - $3^{rd}incl.$ - 2000x magnif. and stress	104
A.4 Test 1 - $3^{rd}incl.$ - SEM analyses	104
A.5 Test 2 - $2^{nd}incl.$ - 2000x magnif. and stress	105
A.6 Test 2 - $2^{nd}incl.$ - SEM analyses	105
A.7 Test 2 - $3^{rd}incl.$ - 2000x magnif. and stress	106
A.8 Test 2 - $3^{rd}incl.$ - SEM analyses	106
A.9 Test 5 - $2^{nd}incl.$ - 2000x magnif.	107
A.10 Test 5 - $2^{nd}incl.$ - SEM analyses	107
A.11 Test 6 - $2^{nd}incl.$ - 2000x magnif. and stress	108
A.12 Test 6 - $2^{nd}incl.$ - SEM analyses	108
A.13 Test 6 - $2^{nd}incl.$ - 2000x magnif.	109
A.14 Test 6 - $3^{rd}incl.$ - SEM analyses	109
A.15 Test 7 - $2^{nd}incl.$ - 2000x magnif.	109
A.16 Test 7 - $2^{nd}incl.$ - SEM analyses	110

A.17 Test 7 - 3ndincl. - 2000x magnif. and stress 110
A.18 Test 7 - 3ndincl. - SEM analyses 110

List of Tables

4.1	Contact parameters	34
6.1	Effect of the inclusion dimension	45
6.2	Effect of the inclusion shape	47
6.3	Effect of the depth	49
6.4	Effect of the composition	51
7.1	Test 1 - 11.2 h - Results	56
7.2	Test 2 - 33.9 h - Results	59
7.3	Test 3 - 46.9 h - Results	62
7.4	Test 4 - 21.0 h - Results	65
7.5	Test 5 - 35.0 h - Results	68
7.6	Test 6 - 11.2 h - Results	71
7.7	Test 7 - 90.7 h - Results	74
8.1	Specimen 1 - $2.80 \cdot 10^6$ cycles - Results	78
8.2	Specimen 2 - $1.36 \cdot 10^6$ cycles - Results	80
8.3	Specimen 3 - $1.36 \cdot 10^6$ cycles - Results	82
8.4	Specimen 4 - $4.83 \cdot 10^6$ cycles - Results	85
8.5	Specimen 5 - $0.77 \cdot 10^6$ cycles - Results	87
8.6	Specimen 6 - $0.62 \cdot 10^6$ cycles - Results	89
8.7	Specimen 7 - $0.06 \cdot 10^6$ cycles - Results	91

Appendix A

Balls - others inclusions

A.1 Case 1

A.1.1 Second inclusion

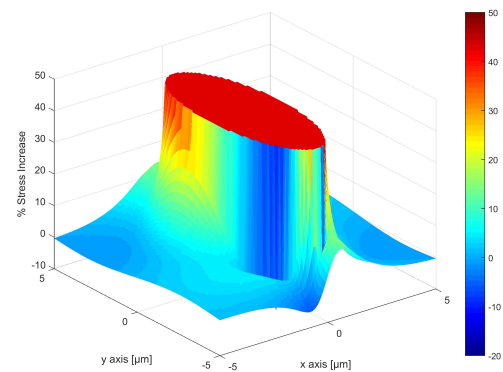
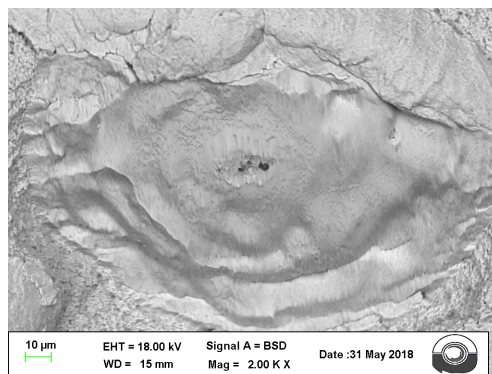


Figure A.1: Test 1 - 2ndincl. - 2000x magnif. and stress

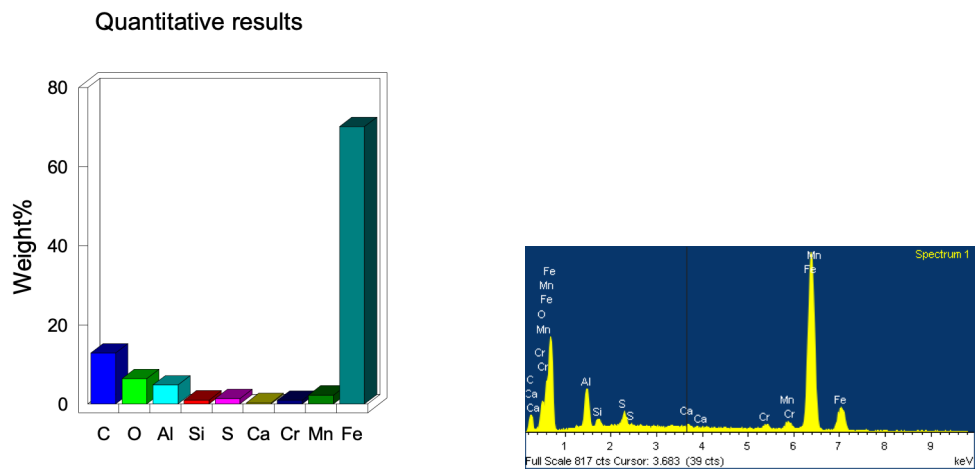


Figure A.2: Test 1 - 2ndincl. - SEM analyses

A.1.2 Third inclusion

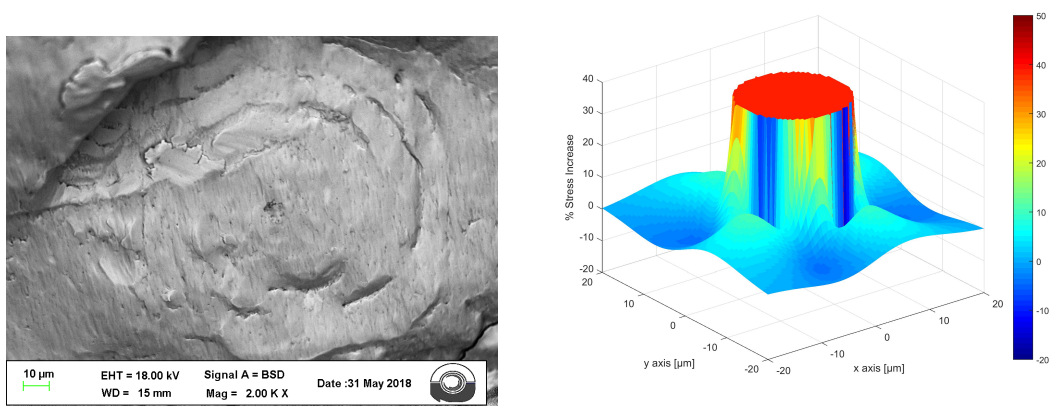


Figure A.3: Test 1 - 3rdincl. - 2000x magnif. and stress

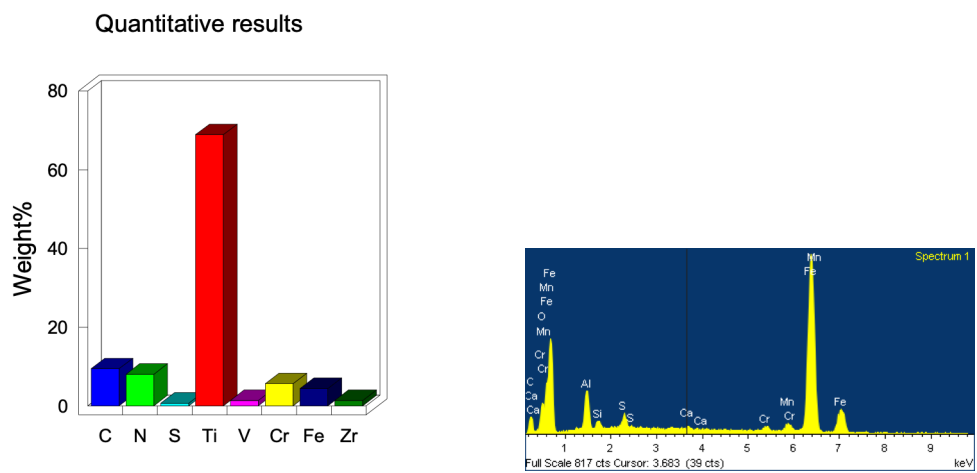


Figure A.4: Test 1 - 3rdincl. - SEM analyses

A.2.2 Third inclusion

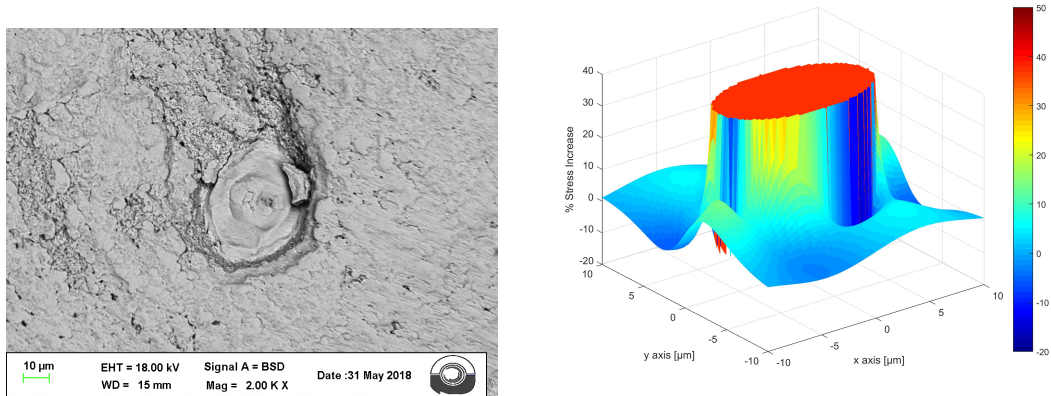


Figure A.7: Test 2 - 3rdincl. - 2000x magnif. and stress

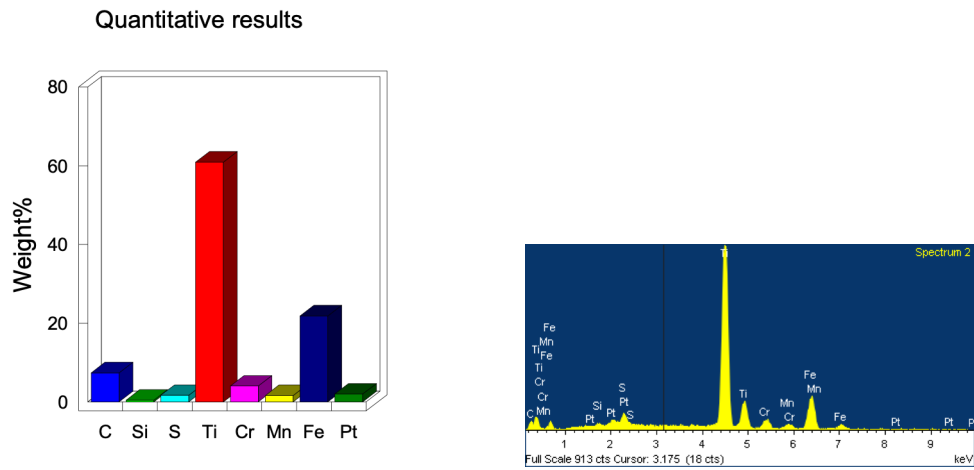


Figure A.8: Test 2 - 3rdincl. - SEM analyses

A.3 Case 5

A.3.1 Second inclusion

Not possible to estimate correctly the Young Modulus.

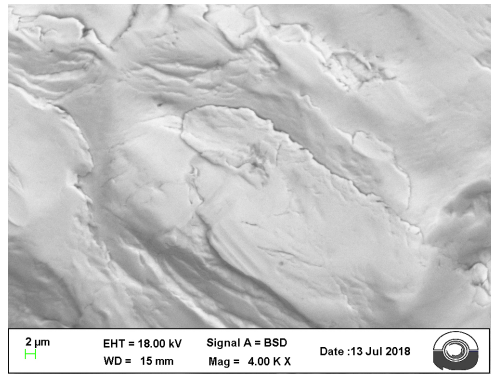


Figure A.9: Test 5 - 2ndincl. - 2000x magnif.

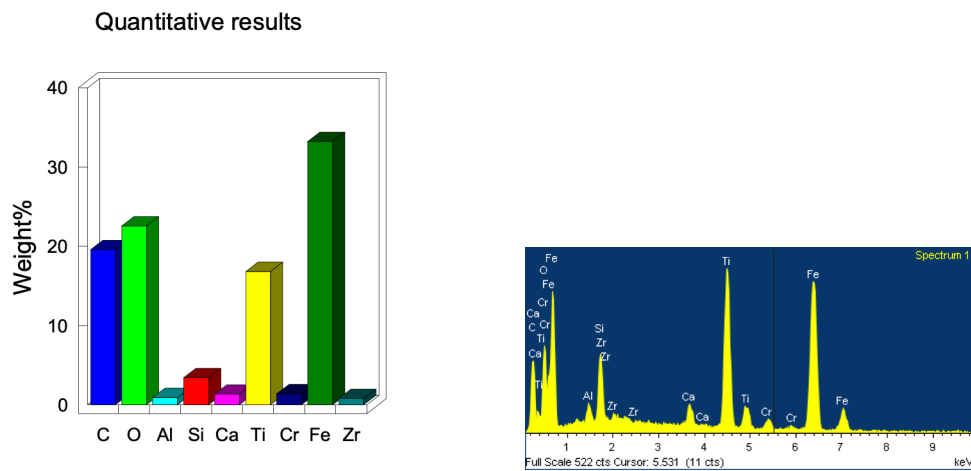


Figure A.10: Test 5 - 2ndincl. - SEM analyses

A.4 Case 6

A.4.1 Second inclusion

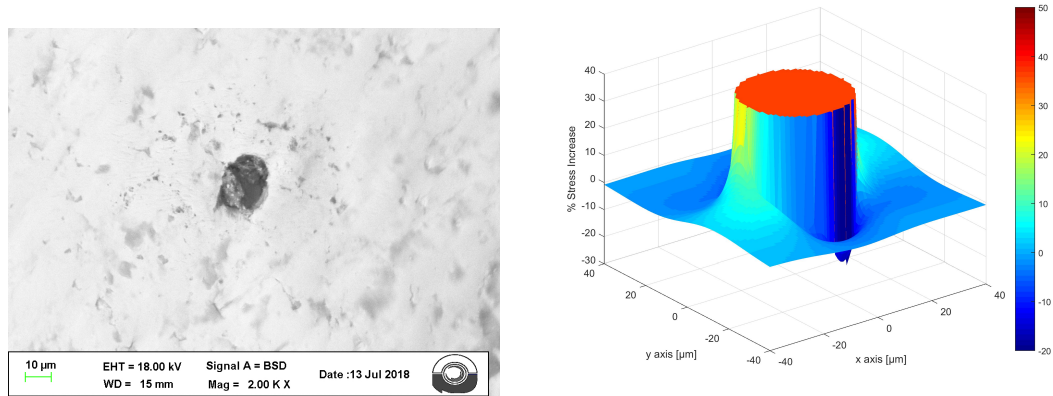


Figure A.11: Test 6 - 2ndincl. - 2000x magnif. and stress

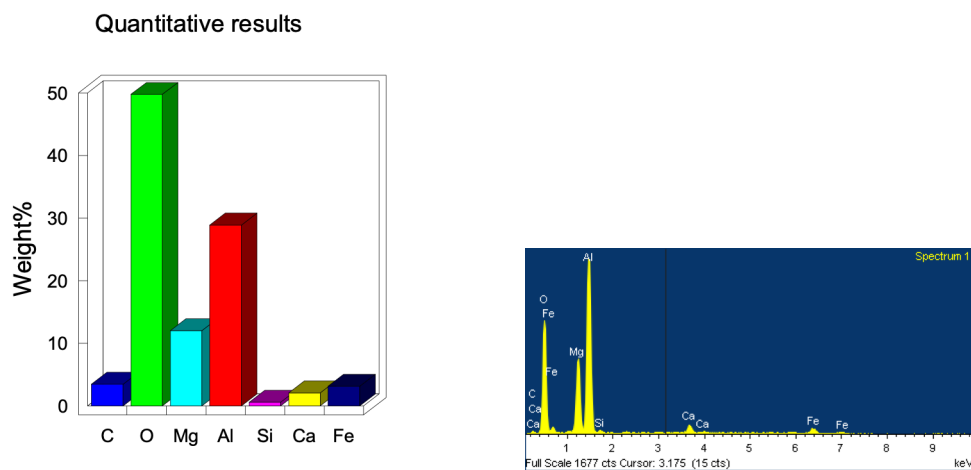


Figure A.12: Test 6 - 2ndincl. - SEM analyses

A.4.2 Third inclusion

Not possible to estimate the Young Modulus and the inclusion dimension.

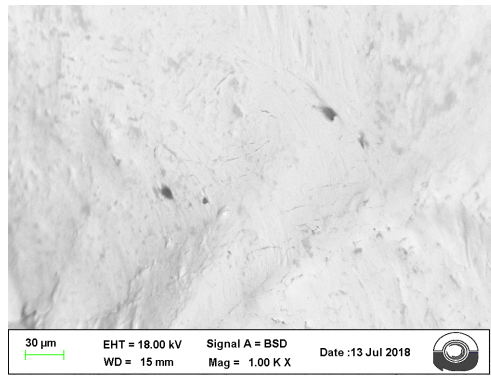


Figure A.13: Test 6 - 2ndincl. - 2000x magnif.

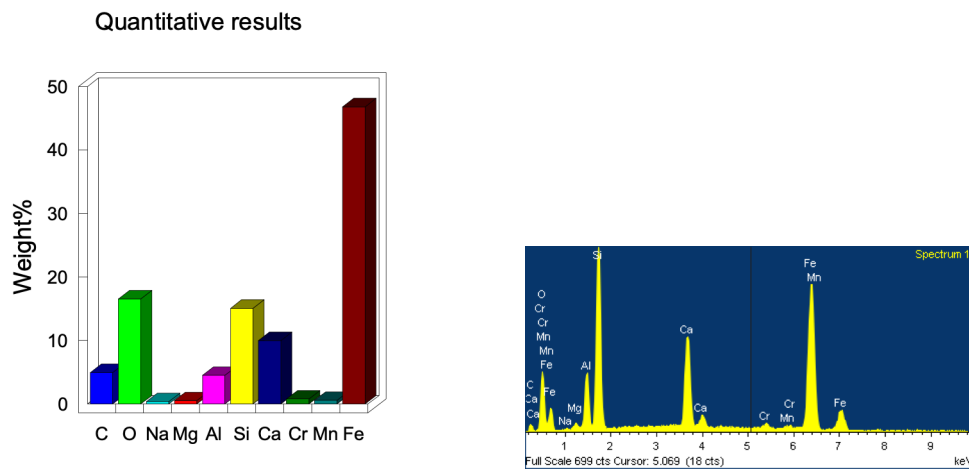


Figure A.14: Test 6 - 3rdincl. - SEM analyses

A.5 Case 7

A.5.1 Second inclusion

Not possible to detect the inclusion dimensions.

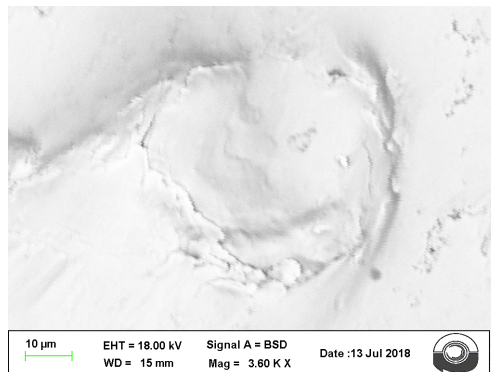


Figure A.15: Test 7 - 2ndincl. - 2000x magnif.

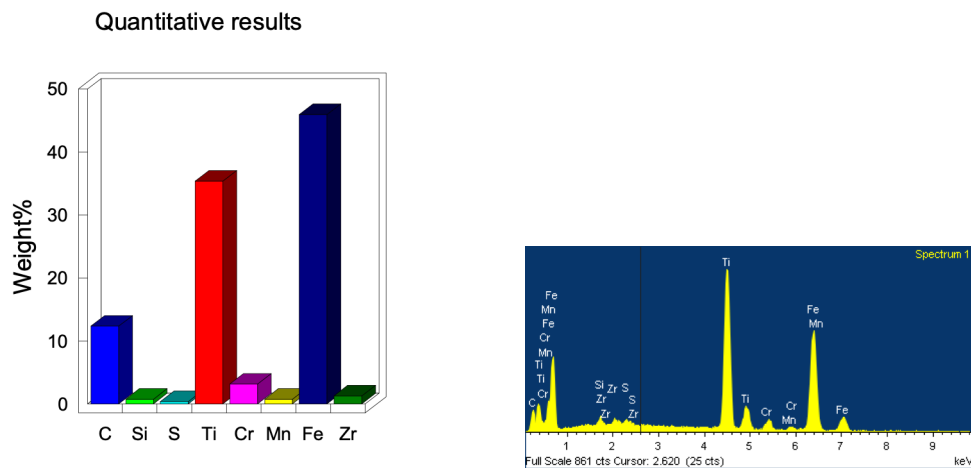


Figure A.16: Test 7 - 2ndincl. - SEM analyses

A.5.2 Third inclusion

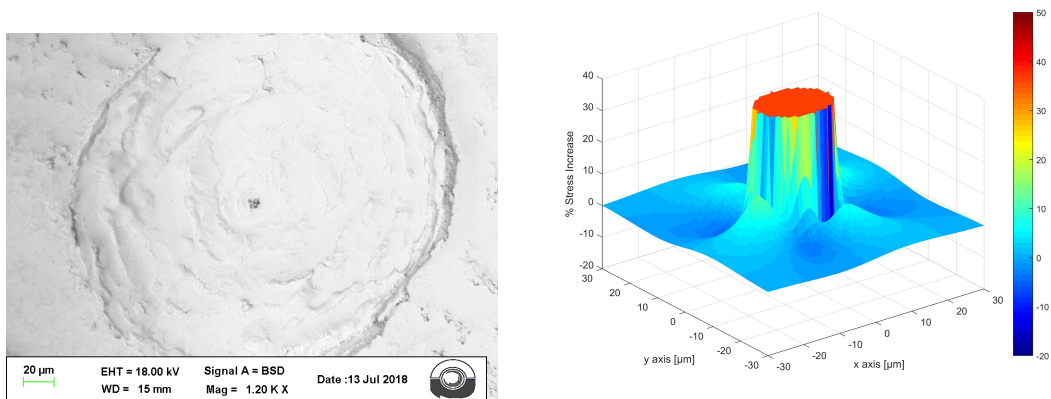


Figure A.17: Test 7 - 3rdincl. - 2000x magnif. and stress

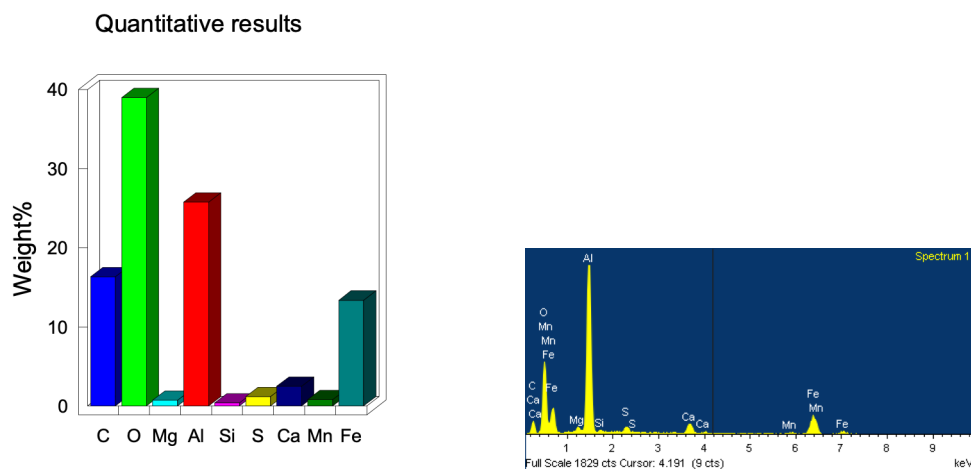


Figure A.18: Test 7 - 3rdincl. - SEM analyses

Bibliography

- [1] Stienon A. et al. “A new methodology based on X-ray micro-tomography to estimate stress concentrations around inclusions in high strength steels”. In: *Mater Sci Eng A* (2009).
- [2] H.K.D.H. Bhadeshia. *Steels for bearings*. SKF University Technology Centre for Steels, University of Cambridge, and UK, 2012.
- [3] Healy D. “Elastic field in 3D due to a spheroidal inclusion - MATLAB code for Eshelby’s solution”. In: *Computers and Geosciences* (2008).
- [4] J.D. Eshelby. *The determination of the elastic field of an ellipsoidal inclusion, and related problems*. Department of physical metalurgy, University of Birmingham, 1957.
- [5] ASTM Int. *Standard Methods for Determining the Inclusion Content of Steel, E45*.
- [6] E. Ioannides and T.A. Harris. “A Physically based model for endurance limit of bearing steels”. In: *Journal of Tribology* (1985).
- [7] T.A. Ioannides E. Harris and M. Ragen. “Endurance of aircraft gas turbine mainshaft ball bearings - Analysis using improved fatigue life theory: Part I”. In: *Journal of Tribology* (1990).
- [8] Courbon J. et al. “Influence of inclusion pairs, clusters and stringers on the lower bound of the endurance limit of bearing steels”. In: *Tribology International* (2003).
- [9] Guan J. et al. “Effects of non-metallic inclusions on the crack propagation in bearing steel”. In: *Tribology International* (2016).
- [10] P.K. Pearson J.F. Braza and C.J. Hannigan. “The performance of 52100, M-50 and M-50 NiL steels in radial bearings”. In: *International Off-Highway and Powerplant Congress SAE Technical Paper Series* (1993), pp. 1–13.

-
- [11] Hashimoto K. et al. “Study of rolling contact fatigue of bearing steels in relation to various oxide inclusions”. In: *Materials and Design* (2010).
- [12] P. Lamagnere et al. “A Physically based model for endurance limit of bearing steels”. In: *Journal of Tribology* (1998).
- [13] Igor M. “Elliptic integrals and functions”. In: *Mathworks* (2005).
- [14] Moghaddam S. M. et al. “Effect of non-metallic inclusions on butterfly wing initiation, crack formation, and spall geometry in bearing steels”. In: *International Journal of fatigue* (2015).
- [15] Nagao M., Hiraoka K., and Unigame Y. “Influence of non metallic inclusion size on rolling contact fatigue life in bearing steel”. In: *Sanyo Tech. Rep.* (2005).
- [16] Pollard D. D. Meng C. Heltsley W. “Evaluation of the Eshelby solution for the ellipsoidal inclusion and heterogeneity”. In: *Computers and Geosciences* (2011).
- [17] Mura T. *Micromechanics of defects in solis*. Dordrecht, 1987.
- [18] Seki T. “Evaluation procedures of nonmetallic inclusions size by statistics and extreme value and prediction of fatigue life in bearing steels”. In: *Aichi Tech. rep.* (1995).
- [19] M.A. Raegan T.A. Harris and R.F. Spitzer. “The effect of hoop and material residual stresses on the fatigue life of high speed, rolling bearings”. In: *Tribology Transactions* 35 (1992), pp. 194–198.
- [20] W. Weibull. *A statistical theory of the strenght of Materials*. Royal Swedish Institute for Engineering Research, 1939.
- [21] Moschovidis ZA. “Two ellipsoidal inhomogeneities and related problems treated by the equivalent inclusion method”. In: *Ph.D. Thesis, Northwestern University, Evanston* (1975).